Silicon Field-Effect Sensors for Biomolecular Assays

by

Emily Barbara Cooper

S.B. Electrical Engineering, Massachusetts Institute of Technology (2000)
M.Eng. Electrical Engineering, Massachusetts Institute of Technology (2000)

Submitted to the Department of Electrical Engineering and Computer Science
in partial fulfillment of the requirements for the degree of

Doctor of Philosophy

at the

MASSACHUSETTS INSTITUTE OF TECHNOLOGY

September 2003

Author ....
Department of Electrical Engineering and Computer Science
August 22, 2003

Certified by... .....
Scott R. Manalis
Associate Professor of Media Arts and Sciences, and Biological Engineering
Thesis Supervisor

Accepted by ....
Arthur C. Smith
Chairman, Department Committee on Graduate Students

Silicon Field-Effect Sensors for Biomolecular Assays

by

Emily Barbara Cooper

Submitted to the Department of Electrical Engineering and Computer Science
on August 22, 2003, in partial fulfillment of the
requirements for the degree of
Doctor of Philosophy

Abstract

System-level understanding of biological processes requires the development of novel biosensors capable of quantitative, real-time readout of molecular interactions. Label-free detection methods can minimize costs in time and resources by obviating preparatory steps necessary with label-based methods. They may further be valuable for monitoring biomolecular systems which are difficult or impossible to tag, or for which reporter molecules interfere with biological function. Field-effect sensing is a method of directly sensing intrinsic electrical charge associated with biomolecules without the need for reporter molecules. Microfabrication of field-effect biosensors enables their integration in compact microanalytical systems, as well as the potential to be scaled down in size and up in number.

Applying field-effect sensing to the detection and real-time monitoring of specific molecular interactions has long been of interest for protein and nucleic acids analysis. However, these applications are inhibited by serious practical limitations imposed by charge screening in solution. The development of effective measurement techniques requires inquiry into aspects of device engineering, surface chemistry, and buffer conditions.

This thesis describes a body of experimental work that investigates the feasibility of label-free analysis of biomolecular interactions by field-effect. This work begins with the microfabrication of field-effect sensors with extremely thin gate oxide, which enables improved surface potential resolution over previously reported sensors. The performance of these sensors has been characterized in terms of drift, noise, and leakage. To better understand the applicability of these sensors, we have characterized the sensors' response to pH, adsorption of polyelectrolyte multilayers, and high-affinity molecular recognition over a range of buffer conditions. Direct, label-free detection of DNA hybridization was accomplished by combining the high-resolution sensors, with enabling surface chemistry, and a differential readout technique.

Finally, we explore the lateral scaling limits of potentiometry by applying a novel nanolithographic technique to the fabrication of a single electron transistor that demonstrates Coulomb oscillations at room temperature.

Thesis Supervisor: Scott R. Manalis
Title: Associate Professor of Media Arts and Sciences, and Biological Engineering

Contents

List of Figures

Chapter 1

Introduction

1.1 Label Free Detection

This thesis investigates the applicability of microfabricated field-effect sensors to the detection and measurement of specific molecular interactions. This work is situated at the confluence of current biosensing needs and rapidly developing fabrication capabilities. The extraordinary scaling of integrated circuits achieved in recent decades has inspired the application of microfabrication techniques in a variety of fields, among them, bioanalytical systems. Microfabricated biosensor research aims to enable greater assay efficiency, compact analytical systems for diagnostics, and novel detection capabilities inaccessible with current technologies.

Specific molecular detection is enabled by recognition events between molecules that have specific affinities, examples of which are antigen-antibody binding, nucleic acid hybridization, and receptor-ligand binding. In a typical assay, a probe molecule, which has specific affinity to the target molecule of interest is immobilized on a surface. The test analyte is washed over the surface and if the target is present, it will bind specifically to the probe. These binding events are most routinely transduced by reporter molecules such as fluorescent, chemiluminescent, redox, or radioactive labels. The high concentration sensitivity achievable by label-dependent methods, as well as their applicability to a wide range of molecules have ensured their widespread use. However, there are a number of detection scenarios in which label-independent methods offer advantages.

Label-free detection methods can minimize costs in time and resources by obviating preparatory steps necessary with label-based methods. Labeling yield can be difficult to control, introducing variability among measurements. Label-free methods eliminate the time constraints of fluorescence-based assays, which are susceptible to bleaching or quenching. They may further be valuable for

monitoring biomolecular systems which are difficult or impossible to tag, or for which reporter molecules interfere with biological function. Label-based technologies are end-point detection systems, meaning that one measurement is made at a fixed time point. This can be contrasted to direct, continuous, real-time measurements to which label-free methods are well suited.

Currently, a few label-free detection systems are commercially available. Most notable among these are Quartz Crystal Microbalance(QCM) systems and Surface Plasmon Resonance (SPR) systems.[1,2] Each of these methods can be funcitonalized with probe molecules to enable specific molecular detection. QCM is a mass-sensitive technique, where the resonant frequency of the quartz crystal shifts when molecules bind to the surface. SPR measures change in refractive index of a surface as molecules bind. The mass resolution of these techniques is about one nanogram per square centimeter. These are generalizable to many assay systems, and offer real-time, label-free detection. However, they have not yet been integrated into micro-analytical system.

Microfabrication enables integration with microfluidics handling systems and readout electronics. The development of compact, integrated systems especially targets decentralized point-of-care diagnostics and environmental sensing, where label-dependent systems would be too cumbersome for routine use. The integration of analytic systems minimizes analyte loss through handling. The sensors developed in the bulk of the work presented here have been developed using established, high-yield processes, which enable the parallel production of hundreds of sensors per silicon wafer. Appropriate materials have been employed at appropriate length scales to anticipate integrability. Sensors can be implemented in multiplex arrays, scaled down in size, and scaled up in areal density.

In addition to making current assays more accessible to a broader range of applications, the sensing method described in this thesis looks toward the future of biosensing. The understanding of biology at a systems level requires quantitative, dynamic measurement of biological processes, beyond the capability of current technologies. Label-free systems in particular have the potential to address systems which are difficult to label, or for which labeling interferes with normal biological function. We anticipate that development of label-independent methods will enable assays which are currently infeasible.

This thesis is concerned specifically with the development of field-effect sensing, a method of directly measuring intrinsic electrical charge associated with biomolecules, without the need

[1]C.K. O'Sullivan and G.G. Guilbault. "Commercial quartz crystal microbalances — theory and applications." *Biosensors and Bioelectronics* **14** 663 (1999).

[2]C. Kößlinger, E. Uttenthaler, S. Drost, F. Aberl, H. Wolf, G. Brink, A. Stanglmaier, and E. Sackmann. "Comparison of the QCM and the SPR method for surface studies and immunological applications." *Sensors and Acutators B* **24-25** 107 (1995).

for intermediary reporter molecules. This first chapter will describe the sensing technique and its development over the past thirty years. While commercially available technologies have been developed from this concept, charge screening in solution has limited the development of field-effect systems for detecting molecular binding. Consideration of this limitation will introduce the approach taken by this work, addressing sensor resolution and assay conditions.

1.2 Field-Effect Sensor Concept: The Electrolyte-Insulator-Semiconductor System

Field-effect sensing offers a method of directly measuring intrinsic electrical charge associated with biomolecules without the need for intermediary reporter molecules. Field-effect sensors are based on the electrolyte-insulator-semiconductor (EIS)[3] structure (analogous to a metal-oxide-semiconductor, MOS, structure) and act as potentiometers, measuring the surface potential at an insulator-electrolyte interface. Just as voltage applied at the metal gate modulates the charge distribution in the silicon portion of an MOS structure, the surface potential at the electrolyte-insulator interface of an EIS structure modulates the charge distribution in the silicon region below (shown schematically in 1-1). Since many biomolecules possess significant net charge, molecular recognition events at the sensor surface can be read as shifts in surface potential. Such sensors promise the ability for quantitative, real-time, concentration-sensitive detection. A standard counter-electrode in the electrolyte solution allows the EIS structure to be biased in a sensitive regime of operation.

1.3 Historical Development of Field-Effect Biosensors

EIS sensors were pioneered by Bergveld, who developed the ion-sensitive field-effect transistor (ISFET).[4,5] In this structure, the modulation of the silicon depletion region is measured by the lateral conductance of the silicon below the gate region. In Bergveld's initial work, ISFETs were operated without a counter electrode in solution. Despite the subsequent confusion[6] over the operating principle of a device whose electrolyte is not apparently referenced to the silicon, Bergveld was able to

[3]In an unfortunate name-space collision, this acronym is also used to refer to Electrical Impendance Spectroscopy, a technique that measures impedance of molecular layers on an electrode in solution.

[4]P. Bergveld. "Development of an Ion-Sensitive Solid-State Device for Neurophysiological Measurements." *IEEE Transactions on Biomedical Engineering* **19** 70 (1970).

[5]P. Bergveld. "Development, Operation, and Application of the Ion-Sensitive Field-Effect Transistor as a Tool for Electrophysiology." *IEEE Transactions on Biomedical Engineering* **19** 342 (1972).

[6]J. N. Zemel. "Ion-sensitive Field Effect Transistors and Related Devices." *Analytical Chemistry* **47** 255A (1975).

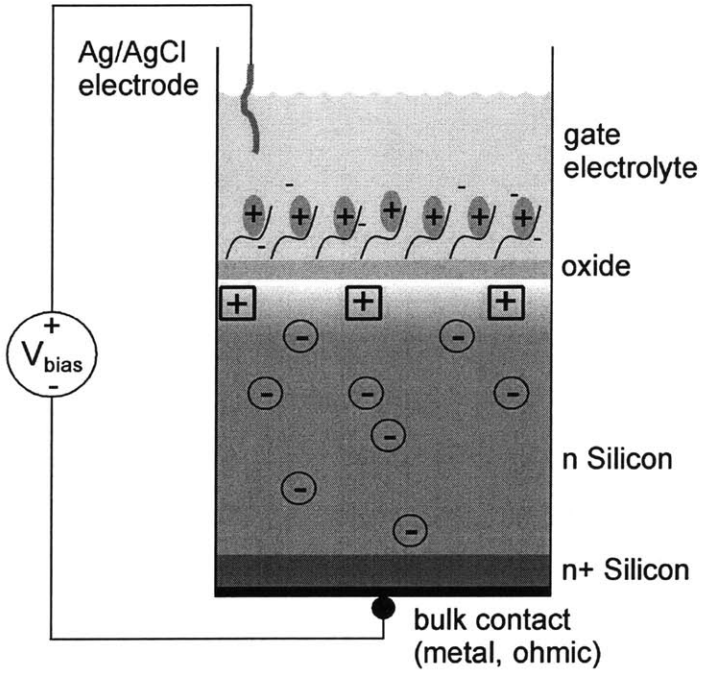

Figure 1-1: Schematic representation of n-type Electrolyte-Insulator-Semiconductor structure

Charged molecules modulate the depletion region charge by field effect since no direct current can flow across the oxide.

use early ISFETs to measure electrical activity in muscle fibers. Moss and coworkers[7] established the importance of the counter-electrode for establishing a bias potential, which was critical for developing an understanding of the ISFET operating principle. Since then, ISFETs have been typically operated in constant-current mode in which a feedback circuit is used to maintain a constant drain current by adjusting the bias potential at the counter electrode in solution. Surface potential changes at the electrolyte-insulator interface are measured by monitoring the compensating gate voltage that must be supplied at the counter electrode.

Alternately, the electrolyte-insulator surface potential can be measured with an EIS capacitor (EISCAP) structure analogous to an MOS capacitor (MOSCAP), as demonstrated by Siu and Cobbold.[8] The EISCAP structure has fewer electrical contacts than the ISFET, which alleviates some of the encapsulation difficulties of ISFET structures where electrical shorting of the electrolyte solution at the source and drain contacts must be prevented. The electrolyte-insulator surface potential can be determined by measuring the capacitance of the silicon space-charge region under the gate. Capacitance versus voltage (CV) characteristics can be measured for EISCAPs by methods[9] analogous to CV characterization techniques for MOS structures.[10]

The development of the Light-Addressable Potentiometric Sensor (LAPS) demonstrated an alternative method for measuring the silicon depletion capacitance.[11] An intensity-modulated light source produces an alternating current response of photogenerated carriers drifting in the high electric field in the space-charge region. The current is highest when there is a large space-charge region in the silicon, i.e. in the inversion regime, and lowest when the space-charge region is smallest, i.e. in accumulation. Since a light source can be directed to a localized region of the sensor, spatially localized measurements of surface potential can be made. Hafeman and coworkers demonstrated the multiplexed readout of nine distinct locations with a single silicon contact[11] This method scales well for multiplexing with a small number of fabricated electrical contacts per sensor region. Spatial resolution is limited by minority carrier diffusion length within the substrate.[12],[13] which is most

[7]S. D. Moss, J. Janata, and C. C. Johnson. "Potassium Ion-Sensitive Field Effect Transistor." *Analytical Chemistry* **47** 2238 (1975).

[8]W. M. Siu and R. S. C. Cobbold. "Basic Properties of the Electrolyte-SiO2-Si System: Physical and Theoretical Aspects." *IEEE Transactions on Electron Devices* **ED-26** 1805 (1979).

[9]B. Prasad and R. Lal. "A capacitive immunosensor measurement system with a lock-in amplifier and potentiostatic control by software." *Measurement Science and Technology* **10** 1097 (1999).

[10]M. Kuhn. "A quasi-static technique for MOS C-V and surface state measurements." *Solid-State Electronics* **13** 873 (1970).

[11]D.G. Hafeman, J.W. Parce, and H.M. McConnell. "Light-Addressable Potentiometric Sensor for Biochemical Systems." *Science* **240** 1182 (1988).

[12]L. Bousse, H. Mostarshed, D. Hafeman, M. Sartore, M. Adami, and C. Nicolini. "Investigation of carrier transport through silicon wafers by photocurrent measurements." *Journal of Applied Physics* **75** 4000 (1994).

[13]W.J. Parak, U.G. Hofmann, H.E. Gaub, and J.C. Owicki. "Lateral resolution of light-addressable potentiometric

effectively controlled by limiting the thickness and feature sizes of the silicon substrate[13,14] By using a 0.5 micron polysilicon substrate, local pH can be measured with sub-micron resolution[14].

1.4 Applications: pH sensing, Local Metabolism, Neurobiology

Typical EIS insulators such as oxides and nitrides exhibit pH sensitivity without further surface preparation because they possess readily ionizable surface groups, whose charge state varies with pH. Silicon nitride, oxynitride, and aluminum oxide are particularly useful as gate insulators for pH-sensing EIS structures since they exhibit nearly linear response over a broad range of pH values.[15]

The pH sensitivity of EIS sensors enables their application to monitoring the metabolism of groups of cells. The LAPS was employed primarily for this purpose monitoring the rate at which a collection of $\sim 10^5$ cells acidify their buffer environment.[16,17] This work was extended by the Wolf group who monitored the metabolism of small numbers of cells adherent on ISFETs.[18] Using a differential setup, the metabolism of 5-10 adherent tumor cells was measured. This measurement was enabled by the proximity of adherent cells to one sensor of the differential pair, such that a localized gradient of metabolic products could be measured between the differential pair.

1.5 Challenges: Specific Molecular Detection

Given the success of pH sensing, and the ability of field-effect sensor to measure ionic charge density at the insulator-electrolyte interface, a logical next step was to turn to the detection of charged biomolecules. At least as early as 1975, the idea of functionalizing EIS sensor surfaces with molecules that could act as specific biorecognition elements was circulating in the research community[7]. Over the next 20 years, many attempts were made by the growing ISFET research community to measure antigen-antibody binding, extremely selective molecular recognition mechanisms relevant to immune response. After a series of unsuccessful experiments that were primarily reported in a

sensors: an experimental and theoretical investigation." *Sensors and Actuators A* **63** 47 (1997).

[14]Y. Ito. "High-spatial resolution LAPS." *Sensors and Actuators B* **52** 107 (1998).

[15]D.L. Harame, L.J. Bousse, J.D. Shott, and J.D. Meindl. "Ion-Sensing Devices with Silicon Nitride and Borosilicate Glass Insulators." *IEEE Transactions on Electron Devcies* **ED-34** 1700 (1987).

[16]H.M. McConnell, J.C. Owicki, J.W. Parce, D. L. Miller, G.T. Baxter, H.G. Wada, and S. Pitchford. "The Cytosensor Microphysiometer: Biological Application of Silioen Technology" *Science* **257** 1906 (1992).

[17]J. C. Owicki, and J. W. Parce. "Biosensors based on the energy metabolism of living cells The physical chemistry and cell biology of extracellular acidification." *Biosensors and Bioelectronics* **7** 225 (1992).

[18]M. Lehmann, W. Baumann, M. Brischwein, R. Ehret, M. Kraus, A. Schwinde, M Bitzenhofer, I. Freund, and B. Wolf. "Non-invasive measurement of cell membrane associated proton gradients by ion-sensitive field-effect transistor arrays for microphysiological and bioelectronical applications." *Biosensors and Bioelectronics* **15** 117 (2000).

handful of negative-result doctoral theses (see references in Koch et al.[19]), Bergveld dismissed field-effect sensing of specific molecular interactions in an article entitled "The Future of Biosensors"[20]:

> This imaginary device was called an ImmunoFET (IMFET), but its operation has never been proven to exist. The reason is of course that no net charge is available, because the surface charges of protein molecules are neutralized by ever-present counter ions. The resulting double layer, with a thickness of the Debye length, is of the order of 1 nm thick in moderate electrolyte concentrations. Beyond this distance, no external electric field exists. Hence the idea that a layer of charged molecules at the surface of an ISFET modulates the electric field in the gate oxide *should definitely be forgotten* [emphasis added].

Understanding this argument requires consideration of the phenomenon of charge screening in electrolyte solutions. Charged surfaces, whether macromolecules or planar substrates like an EIS gate dielectric, will establish an electrical double layer in an electrolyte solution. The surface charge must be balanced by equal and opposite charge, which is supplied by ions in solution. Ions of opposite charge are attracted, and ions of like charge are repelled. This tendency for electric drift is balanced by diffusion. In the absence of other applied forces, any atom or molecule, charged or not, will diffuse from regions of higher concentration higher concentration to regions of lower concentration. It is easy to see that the tendencies for drift and diffusion oppose each other in this system. The details of charge and potential distribution within this electrical double layer will be described in more detail in Chapter 2.

A simple approximation of the length-scale over which this charge screening takes place can be derived from the Poisson-Boltzmann equation applied to the electrolyte system:

$$\tanh\frac{zq\Psi(x)}{4kT} = \tanh\frac{zq\Psi_(o)}{4kT}e^{\left(-x\sqrt{\frac{2z^2a^2C_o}{\epsilon_w kT}}\right)} \tag{1.1}$$

where $\Psi(x)$ is potential, and $\Psi_(o)$ is defined to be the potential at the electrolyte-insulator interface; k is Boltzmann's constant; T is temperature; q is the elementary charge; ϵ_w is the permittivity of the electrolyte, taken to be the permittivity of water; $C(0)$ is ionic concentration in units $\#/\text{cm}^3$; and z is valence. Here, we will assume a symmetric, monovalant electrolyte such that z = 1;

The characteristic length of the space charge region, the Debye length, is given by

$$L_D = \sqrt{\frac{kT\epsilon_w}{2q^2C_o}} \tag{1.2}$$

[19]S. Koch, P. Woias, L.K. Meixner, S. Drost, and H. Wolf. "Protein detection with a novel ISFET-based zeta potential analyzer." *Biosensors and Bioelectronics* **14** 417 (1999).

[20]P. Bergveld. "The future of biosensors." *Sensors and Actuators A* **56** 65 (1996).

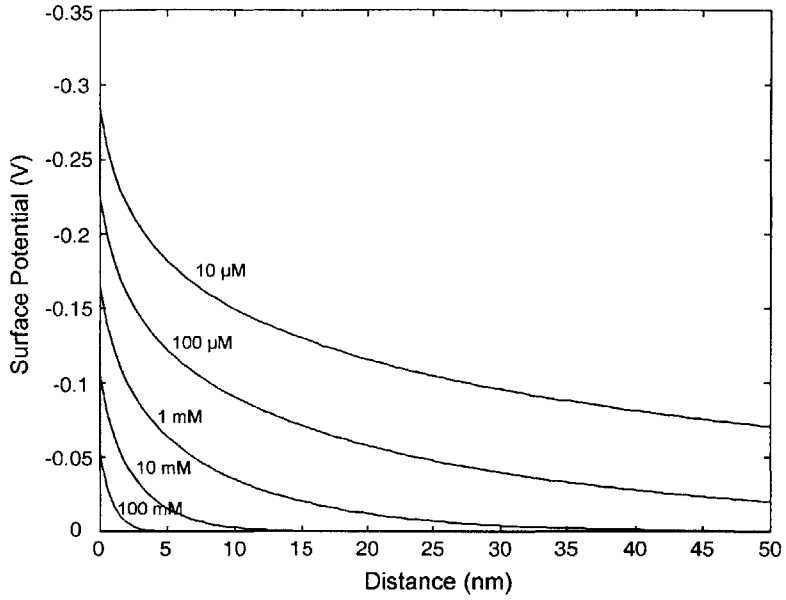

Figure 1-2: Potential decay near a charged surface in an electrolyte
Potential is plotted over a range of concentrations for a symmetric, monovalent electrolyte. A fixed surface charge density of .045 C/cm^2 is assumed.

which describes the exponential term in the above transcendental equation.

Using the above relationships, we can plot the potential near the charged surface in order to get a sense of the relevant length scale. This is shown in Figure 1-2 for a surface with a fixed charge density (0.045 C/cm^2), and various concentrations of symmetric, monovalent electrolytes. High ionic concentrations allow surface charge to be readily screened, within a few nanometers of the surface. This is the length scale to which Bergveld refers in his above statement. In terms of sensing, charge that is more than a few nanometers aways from the surface will be balanced by counter ions in solution, rather than by charge carriers in the silicon. Bergveld's argument is simple: although biomolecules typically possess some characteristic electrical charge, many are larger than the screening length in solution, so molecular recognition events occur too far from the sensor surface to exert significant field on the silicon sensing element.

The measurement limitations imposed by charge screening in solution indicate three areas for improvement of field-effect sensing capabilities. The first explores the limits of the surface potential resolution of the EIS sensor. Increasing the surface potential resolution of sensors would enable easier detection of partially screened charge associated with target molecules. The second is the buffer conditions of an assay. From the sensor perspective, working at low buffer concentration

would be beneficial for imaging charge at the electrolyte-insulator interface. However, many assays of interest require near-biological conditions, with buffer concentrations in the 50-500 mM range. At lower ionics strengths, reaction rates typically decrease, and non-specific interactions increase. Finally, the functionalization chemistry can be optimized in order to locally control the charge micro-environment at the sensor surface. This has the potential to alleviate constraints on buffer conditions required for a particular recognition system.

Meixner and Koch report a theoretical investigation into the local surface potential and charge distribution at the insulator electrolyte interface expected for protein interaction.[21] They conclude that protein interactions may cause signals in the range of 1-10 mV for various buffer conditions. Their conclusion was that because 10 mV is the typical detection limit for field-effect sensors, it is unlikely that potentiometric measurement of protein interactions could be measured by field effect. Although the LAPS demonstrated a noise floor of $\sim$30 μV RMS, there are few demonstrations of specific molecular detection with field-effect devices.

1.6 Scope and Outline of Thesis

In light of the limitations on field-effect sensing imposed by ionic screening, work toward detection of specific molecular binding faces great challenges. The main goal of this thesis has been to investigate scaling limits of device parameters to improve sensor resolution. By using an extrememly thin gate dielectric, the sensors employed in this work have demonstrated a higher surface potential resolution that has been previously demonstrated with EIS sensors. This has enabled fresh investigation into the state-of-the-art of field-effect sensing, exploring types of assays to which this measurement technique is suited, and identifying some bounds on the limitations which remain. In recent years, advancements in areas of surface chemistry, MEMS fabrication, and integration have enabled the development of more compact sensors with a greater repertoire of available surface functionalization techniques. Coupling these techniques with high-resolution sensors, we attempt to develop intuition about interaction of molecular systems with field-effect sensors by developing prototype assays.

A thorough understanding of the charge and potential distribution within the EIS cell is necessary to appreciate both the limitations and the possibilities within this area of research. A detailed analysis of all of the factors affecting the electrochemical micro-environment at the sensor surface would incorporate parameterization of size and areal density of target molecules, probe and target

[21] L.K. Meixner and S. Koch. "Simulation of ISFET operation based on the site binding model." *Sensors and Actuators B* **6** 315 (1992).

concentrations, and buffer concentration. Each of these aspects will be reported and discussed to provide context and understanding of the assays attempted in this work, but a complete numerical analysis of such factors is beyond the scope of this thesis.

The work presented here enables a reassessment of the state of biomolecular detection. While this work does not resolutely conclude the contentious topic of direct potentiometric detection of biomolecules, compelling evidence is presented for continued development of field-effect biosensor systems and assays.

In Chapter 2, I will discuss modeling of the distribution of charge and potential in the EIS system. This will serve two purposes. The first is to enable conscientious design decisions, especially for understanding the scaling of parameters that affect sensitivity. The second is to provide a framework for quantitative interpretation of measurements. Chapter 3 will orient the reader to the fabrication process used to produce the sensors studied in this work. Electrical characterization of these sensors will be discussed in Chapter 4. Chapter 5 examines the sensor response to two different modes of biologically relevant charge: pH titration, and adsorption of polyelectrolytes. DNA hybridization and high-affinity binding of the biotin-avidin system will be examined as two cases of molecular recognition, in Chapter 6. Chapter 7 examines length scaling in terms of sensing capabilities and fabrication capabilities. The conclusions presented in Chapter 8 will detail the specific contributions of this thesis and directions for future work.

Chapter 2

MOS and EIS Theory and Scaling

The general EIS problem encompasses the interaction of the ionic charge system in the electrolyte and the electronic charge system in the solid-state portion of the device. Analysis will be approached by first decoupling the system, addressing the solid-state portion first. The physics of metal-oxide-semiconductor systems will be described, in order to guide sensor design and build intuition about the complete EIS system. Then, the electrolyte portion of the problem will be considered in isolation. The potential drop at the isolated electrolyte-insulator interface is determined by pH, ionic concentration, equilibrium constants and the site density of the insulator surface. Finally, the interaction of the entire system will be discussed, describing the charge and potential equilibrium through all portions of the system.

Throughout this chapter, I will use a dual notation where Φ refers to electrostatic potentials with respect to the silicon bulk and Ψ refers to electrostatic potentials with respect to the electrolyte bulk. This is shown in Figure 2-1, which schematically shows the charge and potential variation through the entire EIS system. This system can be represented by the series connection of five capacitances, shown from left to right in Figure 2-1: the capacitance associated with the diffuse charge layer in solution, C_{diffuse}; the capacitance between the Outer Helmholtz Plane (OHP) and the Inner Helmholtz Plane (IHP), C_{OHP}; the capacitance between the IHP and the oxide surface, C_{IHP}; the oxide capacitance, C_{ox}; and the silicon space-charge capacitance, C_{S}.

For the most part, EIS systems behave as MOS systems, with the exception that the electrolyte portion of the device contributes a potential in series with any applied gate voltage. The electrical potential contributed by the electrolyte is generally taken to be established purely by the electrochemical equilibrium at the electrolyte-insulator interface and is unaffected by the surface charge

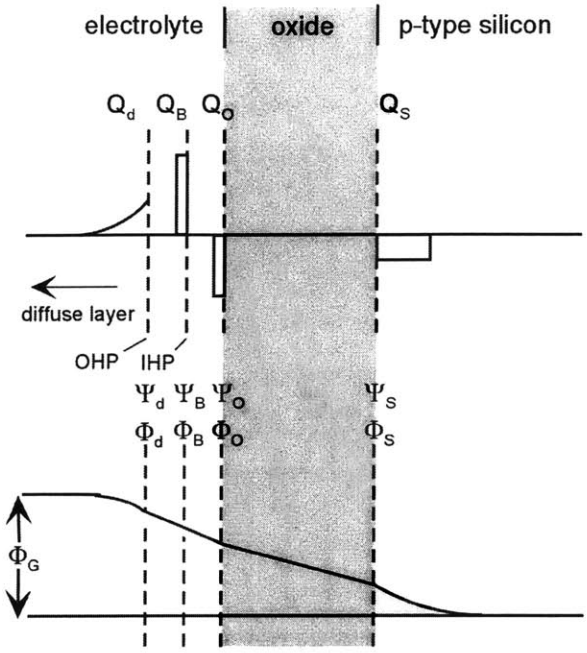

Figure 2-1: Schematic representation of charge and potential distribution in EIS structure
Adapted from Fung et al.[1].

state of the silicon, or by applied bias potential. This assumption is justified for EIS systems with moderately thick (> tens of nanometers)gate insulators, where the capacitance of the oxide and the silicon depletion region are much smaller than any capacitance arising in the electrolyte. The capacitance of an oxide tens of nanometers thick is on the order of tens of nanoFarads per cm^2, while C_{diffuse} is typically hundreds of $\mu F/cm^2$, C_{IHP} is taken to be $140\mu F/cm^2$ and C_{OHP} is taken to be $20\mu F/cm^2$ (see Fung[1] and references therein). As the gate oxide is scaled down to a thickness of tens of Angstroms, it's capacitance is in the range of a few $\mu F/cm^2$. It is not immediately obvious that the electrolyte and silicon portions of the system can be treated as decoupled in systems with very thin gate dielectrics, as those used in this work. The validity of the decoupled approach will be investigated and the entire system will be analyzed with a coupled approach.

[1]C. D. Fung, P. W. Cheung, and W. H. Ko. "A Generalized Theory of an Electrolyte-Insulator-Semiconductor Field-Effect Transistor." *IEEE Trans. Electron. Dev.* **ED-33** 8 (1986).

2.1 MOS Models to Inform Sensor Design

Analysis begins with consideration of MOS physics, neglecting for the moment the electrolyte portion of the problem.

2.1.1 Poisson-Boltzmann Formulation

In describing the silicon portion of the system, the following assumptions and simplifications will be made: silicon doping levels are non-degenerate, such that Boltzmann statistics apply; charges are treated as point charges and volumetric effects are neglected; surface states and fixed charge at the $Si - SiO_2$ interface are neglected, as well as any fixed or mobile charge which may be present in the oxide as processing artifacts. The boundaries of these assumptions will be discussed as they become relevant. All capacitances are area-normalized, in units of F/cm^2.

Boltzmann statistics can be used to describe the relationship between charge carrier density and potential at any point. This is combined with the Poisson equation, which describes the spatial distribution of charge density and potential, to formulate the Poisson-Boltzmann equation describing the space charge region in the gate region of the silicon:

$$\frac{d^2\Phi}{dx^2} = -\frac{qN_D}{\epsilon_s}\left((e^{(-\frac{q\Phi}{kT})} - 1) - \frac{n_i^2}{N_D^2}(e^{(\frac{q\Phi}{kT})} - 1)\right) \tag{2.1}$$

where q is the elementary charge, N_D is ionized donor density, k is Boltzmann's constant, T is temperature, n_i is the intrinsic carrier concentration in silicon, and ϵ_S is the permittivity of silicon. After integration, it is easiest to express the spatial potential distribution and electric field, E, in terms of the $F(\Phi)$ function:

$$\frac{d\Phi}{dx} = -\sqrt{\frac{2kTN_D}{\epsilon_s}}\, F(\Phi) = -E \tag{2.2}$$

$$F(\Phi) = \frac{\Phi}{|\Phi|}\sqrt{\left(e^{(-\frac{q\Phi}{kT})} + \frac{q\Phi}{kT} - 1\right) + \frac{n_i^2}{N_D^2}\left(e^{(\frac{q\Phi}{kT})} - \frac{q\Phi}{kT} - 1\right)} \tag{2.3}$$

Using the potential value at the $Si\text{-}SiO_2$ interface, Φ_S, the total space-charge in the silicon, Q_S, is:

$$Q_S = -\sqrt{2\epsilon_s kTN_D}\, F(\Phi_S) \tag{2.4}$$

The small-signal capacitance of the silicon portion of the MOS structure is defined as the change in space-charge-region charge corresponding to a small change in the silicon surface potential.

$$C_S = \frac{dQ_S}{d\Phi_S} \tag{2.5}$$

So, the general expression relating capacitance to applied voltage, applicable in all regimes of operation is:

$$C_S = \sqrt{2\epsilon_s kTN_D}\frac{dF(\Phi_s)}{d\Phi_s} \tag{2.6}$$

2.1.2 Scaling of Fabrication Parameters

The sensitivity parameter for our sensor is dC/dV–the change in silicon capacitance per applied gate voltage. This is simply the slope of the capacitance-voltage characteristic. This slope is maximal in the regimes of depletion and weak inversion. Using the depletion approximation we can simplify equation 2.6 to the simple formulation:

$$C_{\text{dep}} = \frac{\epsilon_s}{x_{\text{dep}}} \tag{2.7}$$

In this approximation, the depletion capacitance is treated as a parallel plate capacitor, where the distance between the plates is the extent of the space-charge region, x_{dep}. This space-charge region (SCR) width has a voltage dependence of :

$$x_{\text{dep}} = \frac{\epsilon_s}{C_{\text{ox}}}\left(\sqrt{1 - \frac{2C_{\text{ox}}(V - V_{\text{FB}})}{\epsilon_s q N_D}} - 1\right) \tag{2.8}$$

Where $C_{\text{ox}} = \frac{\epsilon_{\text{ox}}}{t_{\text{ox}}}$, an V_{FB} is the flat-band potential of the structure.

To maximize the capacitive response, the response of the depletion region width, dx_{dep}/dV should be maximized. The most significant factor affecting the CV slope is the oxide thickness. This trend is illustrated in Figure 2.1.2. The CV response shows increased sensitivity on both an absolute scale (left) and also a normalized scale (right), where CV characteristics have been scaled relative to the maximum capacitance for each respective oxide thicknesses. Conveniently, the oxide thickness is the parameter over which we have most control during the fabrication process. It is a simple matter to grow different thicknesses of oxide, and etch back existing layers to vary the thickness as an experimental parameter.

The doping level also affects the CV response and should be minimized. The CV response for fixed oxide thickness and variable doping levels is shown in Figure 2-3.

There is a lower limit to the oxide thickness, which is imposed by practical concerns. How thin can the gate oxide be reproducibly fabricated? How thick must the gate oxide be to be stable in the electrochemical cell? How do problems of leakage and drift influence the gate oxide thickness demands? As a first approach, there is insight to be gleaned from the literature of several disciplines.

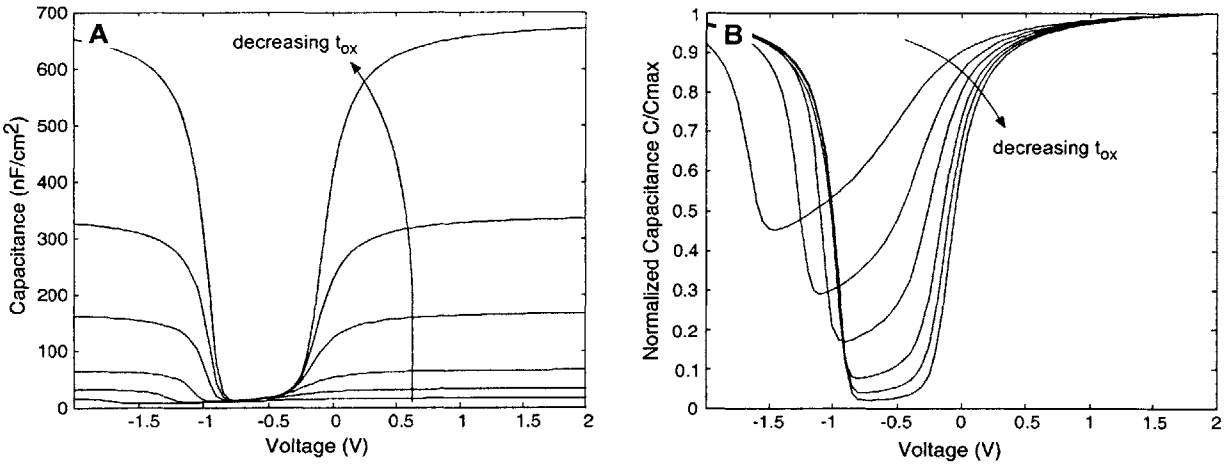

Figure 2-2: Oxide thickness scaling
CV characteristics modeled for MOS structures with gate oxide thickness ranging from 40 nm to 5 nm. A: Absolute scale. B: Normalized $C/C_{\max}$

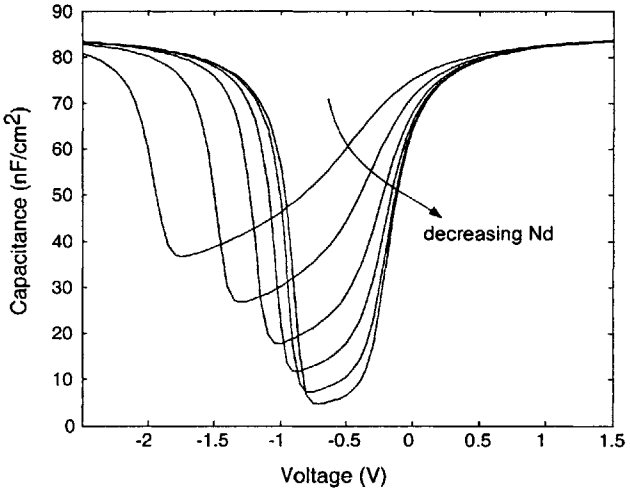

Figure 2-3: Dopant level scaling
CV characteristics modeled for MOS structures with 1.5 nm gate oxide and doping levels ranging from 10^{14} to 3×10^{16}.

Ultimately, these questions must be addressed empirically for our particular system design. This characterization work will be detailed in subsequent chapters.

Scaling the gate dielectric is an important research direction in the development of higher speed and higher density integrated circuits. MOSFET scaling is concerned with minimizing applied power supply voltage. This can be achieved by maximizing the drain current response to applied gate voltage bias. Just like the EIS system, this can be accomplished by reducing the gate oxide thickness. For current high-performance processors, silicon dioxide gates with thicknesses less than 40 Å are used, and MOS devices with thermally grown dielectrics as thin as 15 Å have been demonstrated experimentally.[2] Issues that arise for the IC community include dielectric thickness variation, introduction of impurities through the gate, reliability and lifetime.

The CV behavior of MOS devices with ultra-thin gate oxides are found to show significant deviation from the classical MOS model earlier in this chapter.. The sum of these phenomena can contribute 10-25% attenuation of measured gate capacitance, compared with predicted oxide capacitance in MOS structures. Several factors contribute to this. First, Maxwell-Boltzmann statistics no longer apply, and Fermi-Dirac statistics must be applied in accumulation and inversion, because of degeneracy of states in the narrow space-charge region created by these regimes of operation. Carriers occupy higher-energy states than predicted with Maxwell-Boltzmann statistics, such that a larger surface potential change is required for a given change of charge — dQ/dV, the small-signal capacitance of the silicon depletion region.[3] Second, MOS capacitors with polysilicon gates exhibit bias-dependent gate depletion. This contributes a bias-dependent series capacitance. The capacitance slopes downward in the accumulation regime, as the space-charge region in the polysilicon increases. Even at high doping levels, the polysilicon does not behave as an ideal metal gate for MOSCAPs with ultrathin gate insulators. The polysilicon depletion region is analogous to the space-charge region in the electrolyte. For thicker oxides, space-charge regions are negligibly small for both the polysilicon gate and the electrolyte gate. As the gate dielectric is scaled down, however, potential drop in these space-charge regions become significant, causing additional series capacitances, which lower total measured capacitance.

We might also consider a more theoretical consideration: at what thickness does an oxide cease to exhibit its bulk insulating properties? Muller and colleagues use electron-energy-loss spec-

[2]D.A. Buchanan. "Scaling the gate dielectric: Materials, integration, and reliability." *IBM Journal of Research and Development* **43** 245 (1999).

[3]K.S. Krisch, J.D. Bude, and L. Manchanda. "Gate Capacitance Attenuation in MOS Devices with Thin Gate Dielectrics." *IEEE Electron Device Letters* **17** 521 (1996)

troscopy to resolve interfacial states which spill over from the silicon conduction band wavefunctions into the oxide.[4] They found that the extent of the interface states between Si and SiO_2 sets the fundamental limit of gate oxides at 0.7 nm. With average SiO_2 bond lengths on the order of 1.6 Å, this is about 4 units across.[2]

In biosensing research, ultra-thin gate insulators have been used for impedance measurements with highly doped silicon electrodes. For impedance measurements of the sensor-electrolyte interfacial capacitance, highly doped silicon is used to minimize the contribution of the silicon depletion capacitance. Since the total capacitance of a series connection of capacitances is dominated by the lowest capacitance, minimizing gate oxide thickness maximizes the oxide capacitance, enabling greater sensitivity to capacitances in the electrolyte solution. In the work by Abdelghani et al.,[5] silicon electrodes were stripped of oxide by etching HF, and then a chemical oxide was grown in a piranha solution. Abdelghani's work mainly analyzes the quality of the chemically grown oxide gate, and the impedance contribution of a supported lipid bilayer is demonstrated. In the work of Berney and coworkers,[6] passivation layers were "mechanically degraded" by scribing to reveal a large area ($2 \times 10^5 \mu m^2$) of bare silicon, over which presumably a native oxide formed either in the air ambient, or in solution. These sensors were used to detect 100 pmol quantities of DNA, where the signal-inducing mechanism was interpreted as series capacitance of molecular layers.

2.2 Charge and Potential Distribution at the Electrolyte-Insulator Interface

Turning attention to the electrolyte portion of the problem, the following section describes the mechanisms and modeling of charge and potential distribution in the electrolyte. The electrolyte-insulator interface is considered in isolation, independent of any applied bias potential. It is assumed that the electrolyte concentration is low enough that Boltzmann statistics apply.

The charge and potential distribution at the electrolyte-insulator interface ultimately arises from surface groups on the insulator which become ionized in solution. Tightly bound complexes can also be formed with small ions (e.g. Na^+, Cl^-) from the electrolyte. This surface charge must be

[4]D. A. Muller, T. Sorsch, S. Moccio, F. H. Baumann, K. Evans-Lutterodt, and G. Timp. "The electronic structure at the atomic scale of ultrathin gate oxides." *Nature* **399** 758 (1999).

[5]A. Abdelghani, C. Jacqwuin, M. Huber, R. Detschmann, and E. Sackmann. "Supported lipid membrane on semiconductor electrode." *Materials Chemistry and Physics* **70** 187 (2001).

[6]H. Berney, J. West, E. Haefele, J. Alderman, W. Lane, and J. K. Collins. "A DNA diagnostic biosensor: development characterization and performance." *Sensors and Actuators B* **68** 100 (2000).

balanced by equal and opposite charge, which is distributed in a diffuse layer that nominally extends a few nanometers into the electrolyte. The charge and potential distribution in this electrical double layer depends on pH, ionic type and concentration, equilibrium constants, and number of active surface sites.

The site-binding model, proposed by Yates et al.[7] and expanded by Davis et al.[8] provides a good description of the surface ionization and complexation events at the electrolyte-insulator interface that give rise to pH sensitivity. This model provides a reasonably complete method for estimating the stoichiometry of surface reactions, and the charge and potential distribution at the electrolyte-insulator interface.

The charge at the surface of the silicon dioxide, Q_o, arises from ionizable hydroxyl groups on the oxide surface. The hydroxyl groups are amphoteric sites, meaning that they can act as both charge donors and acceptors. The equilibrium constants which describe each of the surface ionization processes are:

$$\mathrm{K_+} = \frac{[\mathrm{SiOH}][\mathrm{H^+}]_\mathrm{S}}{[\mathrm{SiOH_2^+}]} \tag{2.9}$$

$$\mathrm{K_-} = \frac{[\mathrm{SiO^-}][\mathrm{H^+}]_\mathrm{S}}{[\mathrm{SiOH}]} \tag{2.10}$$

Small ions in solution form tightly bound pairs ('surface complexes'), creating a plane of charge denoted by Q_B. The plane of closest approach, the Inner Helmholtz Plane (IHP), for these ions is typically 1-1.5 Å from the oxide surface. Using an NaCl solution as an example of a monovalent, symmetrical electrolyte, the surface complexation can be described by:

$$\mathrm{K_-^{Na}} = \frac{[\mathrm{SiO^-}][\mathrm{Na^+}]_\mathrm{S}}{[\mathrm{SiO^- - Na^+}]} \tag{2.11}$$

$$\mathrm{K_+^{Cl}} = \frac{[\mathrm{SiOH_2^+}][\mathrm{Cl^-}]_\mathrm{S}}{[\mathrm{SiOH_2^+ - Cl^-}]} \tag{2.12}$$

Values for rate constants that govern both surface ionization surface complexation appear in the literature.[1,8] The remainder of interfacial charge is distributed in a diffuse region extending from the OHP to the bulk of the solution. The OHP is the plane of closest approach for hydrated ions. The

[7]D.E. Yates, S. Levine, and T.W. Healy, "Site-binding model of the electrical double layer at the oxide/water interface." *Journal of the Chemical Society. Faraday Transactions I* **70** 1807 (1974).

[8]J. A. Davis, R. O. James, and J. O. Leckie. "Surface ionization and complexation at the oxide/water interface, I: computation of electrical double layer properties in simple electrolytes." *Journal of Colloid Interface Science* **63** 480 (1978).

potential drop over this layer, called the Zeta potential, is described by the Gouy-Chapman theory based on applying the Poisson-Boltzmann formulation to an ionic conductor. For a monovalent symmetrical solution, the total charge in this layer is related to the Zeta potential as[9]

$$Q_d = -\sqrt{8e_w kTqC_o}\sinh\left(\frac{q\Psi_\zeta}{2kT}\right) \tag{2.14}$$

We can relate the concentration of a species at any point to its bulk concentration according to the Boltzmann distribution:

$$[\mathrm{X}]_\mathrm{i} = [\mathrm{X}]\mathrm{e}^{\left(\frac{-\mathrm{q}\Psi_\mathrm{i}}{\mathrm{kT}}\right)} \tag{2.15}$$

This allows us to relate surface concentrations of species to their bulk values:

$$\mathrm{K}_+ = \frac{[\mathrm{SiOH}][\mathrm{H}^+]}{[\mathrm{SiOH}_2^+]}\mathrm{e}^{\left(\frac{-\mathrm{q}\Psi_\mathrm{O}}{\mathrm{kT}}\right)} \tag{2.16}$$

$$K_- = \frac{[SiO^-][H^+]}{[SiOH]}e^{\left(\frac{-q\Psi_O}{kT}\right)} \tag{2.17}$$

And we know the bulk hydrogen concentration from the pH:

$$\mathrm{pH} = -\log[\mathrm{H}^+] \tag{2.18}$$

$$\mathrm{K}_-^{\mathrm{Na}} = \frac{[\mathrm{SiO}^-]}{[\mathrm{SiO}^-\ \mathrm{Na}^+]}\mathrm{c_o e}^{\left(\frac{-\mathrm{q}\Psi_\beta}{\mathrm{kT}}\right)} \tag{2.19}$$

$$\mathrm{K}_+^{\mathrm{Cl}} = \frac{[\mathrm{SiOH}_2^+]}{[\mathrm{SiOH}_2^+\ \mathrm{Cl}^-]}\mathrm{c_o e}^{\left(\frac{\mathrm{q}\Psi_\beta}{\mathrm{kT}}\right)} \tag{2.20}$$

$[X]$ and c_o are in units mol/L. The surface species, $[X]$, areconstrained in number by the total number of active sites available, Ns. The surface density of each species, σ_i, in units #/cm^2 can be related to $[X]$ as:

$$\sigma_i = Ns\frac{[i]}{[\mathrm{total}]} \tag{2.21}$$

[9]This relationship is also known as the Grahame Equation when used as an approximation of the total potential drop in the electrical double layer :

$$Q_o = -\sqrt{8e_w kTqC_o}\sinh\left(\frac{q\Psi_O}{2kT}\right) \tag{2.13}$$

where

$$[\text{total}] = [\text{SiOH}] + [\text{SiO}^-] + [\text{SiOH}_2^+] + [\text{SiO}^- - \text{Na}^+] + [\text{SiOH}_2^+ - \text{Cl}^-] \tag{2.22}$$

And the various surface charge densities can be described as:

$$Q_o = (\sigma_{[\text{SiOH}_2^+]} + \sigma_{[\text{SiOH}_2^+\ \text{Cl}^-]} - \sigma_{[\text{SiO}^-]} - \sigma_{[\text{SiO}^-\ \text{Na}^+]})q \tag{2.23}$$

$$Q_B = (\sigma_{[\text{SiO}^-\ \text{Na}^+]} - \sigma_{[\text{SiOH}_2^+\ \text{Cl}^-]})q \tag{2.24}$$

For EIS sensors with thick gate dielectrics, the charge in the silicon portion of the device does not alter the charge distribution in the electrolyte, since the electrolyte capacitance is much higher than the dielectric or the silicon capacitance. In this case, the charges in the electrical double-layer sum to zero:

$$0 = Q_B + Q_o + Q_d \tag{2.25}$$

Further, we can related the IHP, OHP, and surface potentials through capacitances:

$$\Psi_O - \Psi_\beta = \frac{Q_o}{C_{\text{IHP}}} \tag{2.26}$$

$$\Psi_\beta - \Psi_\zeta = -\frac{Q_d}{C_{\text{OHP}}} \tag{2.27}$$

C_{IHP} is taken to be $140\mu\text{F/cm}^2$ and C_{OHP} is taken to be $20\mu\text{F/cm}^2$ (Fung[1] and references therein). Fung et al. have shown through modeling that pH response of the ISFET has little sensitivity to the value of C_{IHP} over a range of 100s of $\mu\text{F/cm}^2$. [1]

2.3 Bringing it All Together: the Total EIS Picture

The electrochemical representation of the EIS system can be written as:

metal | **Silicon** | **Insulator** | **Electrolyte** | **Reference Electrode** | **metal′**

When ohmic contacts are supplied to the silicon and to the reference electrode in solution (**metal** and **metal′** in the above representation) and connected to allow the structure to come to

equilibrium, there will nominally be a built-in potential, $\Phi_{\rm bi}$ across the structure. This built-in potential arises because of the difference in electrochemical potentials of the various materials in the system. Traversing the circuit, the total built-in potential can be written as:

$$-\Phi_{\rm bi_{EIS}} = E_{\rm ref} - \Psi_o + \chi_{\rm sol} - \Phi_{Si} \tag{2.28}$$

where the effects of trapped, fixed, or mobile charge in the insulator, as well as interface dipole potentials noted by some authors[10,11] have been neglected. This can be compared to the built-in potential of an MOS system:

$$-\Phi_{\rm bi_{MOS}} = \Phi_M - \Phi_{Si} \tag{2.29}$$

$E_{\rm ref}$, the 'reduced absolute electrode potential,' is the potential of the reference electrode relative to vacuum, which can be found by adding 4.7 V to the reference electrode voltage relative to a Normalized Hydrogen Electrode (NHE). A silver-silver chloride (Ag/AgCl) electrode has a potential of ~0.2 V vs. NHE,[12] although this value varies with electrolyte composition. The junction potential of a reference electrode is minimized so that the reference electrode contribution is constant with applied bias voltage. $\Psi_{\rm o}$ represents the potential dropped in the space charge region at the electrolyte-insulator interface, described in Section 2.2. $\chi_{\rm sol}$ is the electrochemical potential of the electrolyte solution (analogous to a work function defined for a metal or semiconductor).

For most EIS devices, relatively thick dielectric materials are used, such that the silicon and dielectric capacitances are much smaller than any of the electrolyte capacitances. This means that a gate bias voltage applied at **metal**' is dropped primarily over the dielectric and the silicon, with negligible effect on the electrochemical equilibrium in the electrolyte, implying bias-independence of $\Psi_{\rm o}$. Because of the bias independence of $\Psi_{\rm o}$ and $\chi_{\rm o}$, the CV characteristic for the EIS structure is similar to the CV characteristic of an equivalent MOS structure, except that it is shifted along the voltage axis.

It is convenient to discuss this shift in terms of the flat-band voltage, $V_{\rm FB}$, the gate voltage at which there is no potential drop in the silicon and, correspondingly, no space-charge region. Here it is simply $-\Phi_{\rm bi}$. In reality, it is difficult to know $E_{\rm ref}$, $\chi_{\rm sol}$, and $\Psi_{\rm o}$ absolutely, so it is

[10]L. Bousse. "Single electrode potentials related to flat-band voltage measurements on EOS and MOS structures." *Journal of Physical Chemistry* **76** 5128 (1982).

[11]L. Bousse, N.F. De Rooij, P. Bergveld. "Operation of Chemically Sensitive Field-Effect Sensors As a Function of the Insulator-Electrolyte Interface." *IEEE Transactions on Electron Devices* **ED-30** 1263 (1983).

[12]A.J. Bard, and L.R. Faulkner. *Electrochemical Methods : Fundamentals and Applications.* Wiley. New York. 2001.

instructive, therefore to discuss empirical EIS flat-band voltages relative to the flat-band voltages of MOS structures from the same fabrication process. A further discussion of this will be deferred until measurements are presented in Chapter 3.

For the majority of EIS sensors, then, the behavior of the entire system can be captured succinctly. Chemical interactions in the electrolyte affect Ψ_O, which determines the $V_{\mathrm{FB_{EIS}}}$. Standard MOS physics apply, where $\mathrm{V_{FB_{MOS}}}$ is replaced by $\mathrm{V_{FB_{EIS}}}$.

The sensors used in this work feature very thin gate dielectrics, which enable improved surface potential resolution. It is not immediately obvious that the same modeling approach used above is sufficient to describe this EIS system for accurate interpretation of measurements. The assumption that Ψ_O is bias-independent is particularly suspect as the gate dielectric thickness approaches the length scale of charge screening in solution.

For example, biasing of the surface potential has been exploited in recent microfluidic work, in order to control the magnitude and direction of electro-osmotic flow.[13,14] In the resulting device, a metal electrode is separated from the microchannel by a dielectric on the order of tens to hundreds of nanometers thick. In recent work, the developement of channels with thinner dielectric walls has reduced the voltages which must be applied, although the channel walls are still much thicker than the gate dielectrics considered in the work of this thesis. The voltages used in this work are typically in the range of tens of volts, much greater than our bias voltage range of interest, but the channel walls are still much thicker than the gate dielectrics considered in this thesis. This example describes a scenario which would greatly complicate our system. Not only would a bias dependent Ψ_O complicate data interpretation, it might also disrupt the chemistry at the electrolyte-insulator surface.

In investigating the coupled behavior of the system, the electrode contacts will be neglected in order to focus on the inner potential between the electrolyte bulk and the silicon bulk. The goal of the approach below is to put a bound on the potential variation expected the electrolyte portion of the sensor over the bias voltages typically used.

We start by considering an MOS capacitor, using the Poisson-Boltzmann model described above. The CV characteristic for an ideal MOS capacitor with 1.5 nm gate oxide is shown in Figure 2-4A. For ultra-thin gate dielectric MOS devices, deviations from this model have been observed. In par-

[13]R.B.M. Schasfoort, S. Schlautmann, J. Hendrikse, and A. van den Berg. "Field-Effect Flow Control for Microfabricated Fluidic Networks." *Science* **286** 942 (1999).

[14]C. S. Lee, W. C. Blanchard, and C. T. Wu. "Direct Control of the Electroosmosis in Capillary Zon Electrophoresis by Using and External Electric Field." *Analytical Chemistry* **62** 1550 (1990).

ticular, quantum mechanical effects are considered, and Fermi-Dirac statistics must be employed to accurately describe the silicon capacitance in accumulation and inversion due to the non-negligible volume of the space charge layer in these regimes.[15,3] Quantization effects are shown to slightly increase the threshold voltage of MOS devices, but the effect is small for lightly-doped silicon,[15] and it will be neglected here. The effect of the finite width of the inversion and accumulations becomes significant when the dielectric capacitance approaches the SCR capacitance in these regimes, and diminishes the total measured capacitance in these regimes. A more complete model would account for these effects, but since the primary goal here is to show a worst-case approximation , it will be sufficient to use the Maxwell-Boltzmann description — infinitesimal SCR width will only increase any apparent effects in the electrolyte.

First, we can replace the oxide capacitance with total equivalent capacitance of the series connection of C_{ox}, C_{IHP}, C_{OHP}, and C_{diffuse}. Initially, we will assume each of these to be independent of bias potential. The capacitance of the diffuse charge region, C_{diffuse_o}, is

$$C_{\text{diffuse}_o} = \sqrt{\frac{2\epsilon_w q^2 c_o}{kT}} \cosh\left(\frac{q\Psi_{\zeta_o}}{kT}\right) \tag{2.30}$$

where Ψ_{ζ_o} is assumed, at this point, to be insensitive to bias. For the modeling shown below, an ionic concentration of $c_o = 10\text{mM}$, and an initial Zeta potential of $\Psi_\zeta = -.105\text{V}$ was used. The site-binding model was used to derive this Zeta potential for a 10 mM symmetric, monovalent electrolyte solution at pH 6. The equivalent series capacitance is then

$$C_{\text{eq}_o} = \left(\frac{1}{C_{\text{ox}}} + \frac{1}{C_{\text{IHP}}} + \frac{1}{C_{\text{OHP}}} + \frac{1}{C_{\text{diffuse}_o}}\right)^{-1} \tag{2.31}$$

Using this as the gate capacitance, we can revise our estimate of the CV curve, as shown in Figure 2-4A (C_{EIS}), which shows a noticeable decrease in series capacitance compared with the original ideal oxide capacitance.

Next, we can look at the potential dropped in the various regions of the device. We can plot the silicon surface potential and compare it to the potential dropped over the new compound gate dielectric, Figure 2-4B. Here we see that the series connection C_{eq} is affected by a voltage of about 1 to 1.5 V. We can further determine how much of $(V_G - \Phi_S)$ is applied over the diffuse charge region in the electrolyte. For this, we will assume that the oxide capacitance, C_{IHP} and C_{OHP} are insensitive to bias. The portion of $(V_G - \Phi_S)$ dropped over the diffuse layer is

[15]S.-H. Lo, D.A. Buchanan, and Y. Taur. "Modeling and characterization of quantization, polysilicon depletion, and direct tunneling effects in MOSFETS with ultrathin oxides." *IBM Journal of Research and Development* **43** 327 (1999).

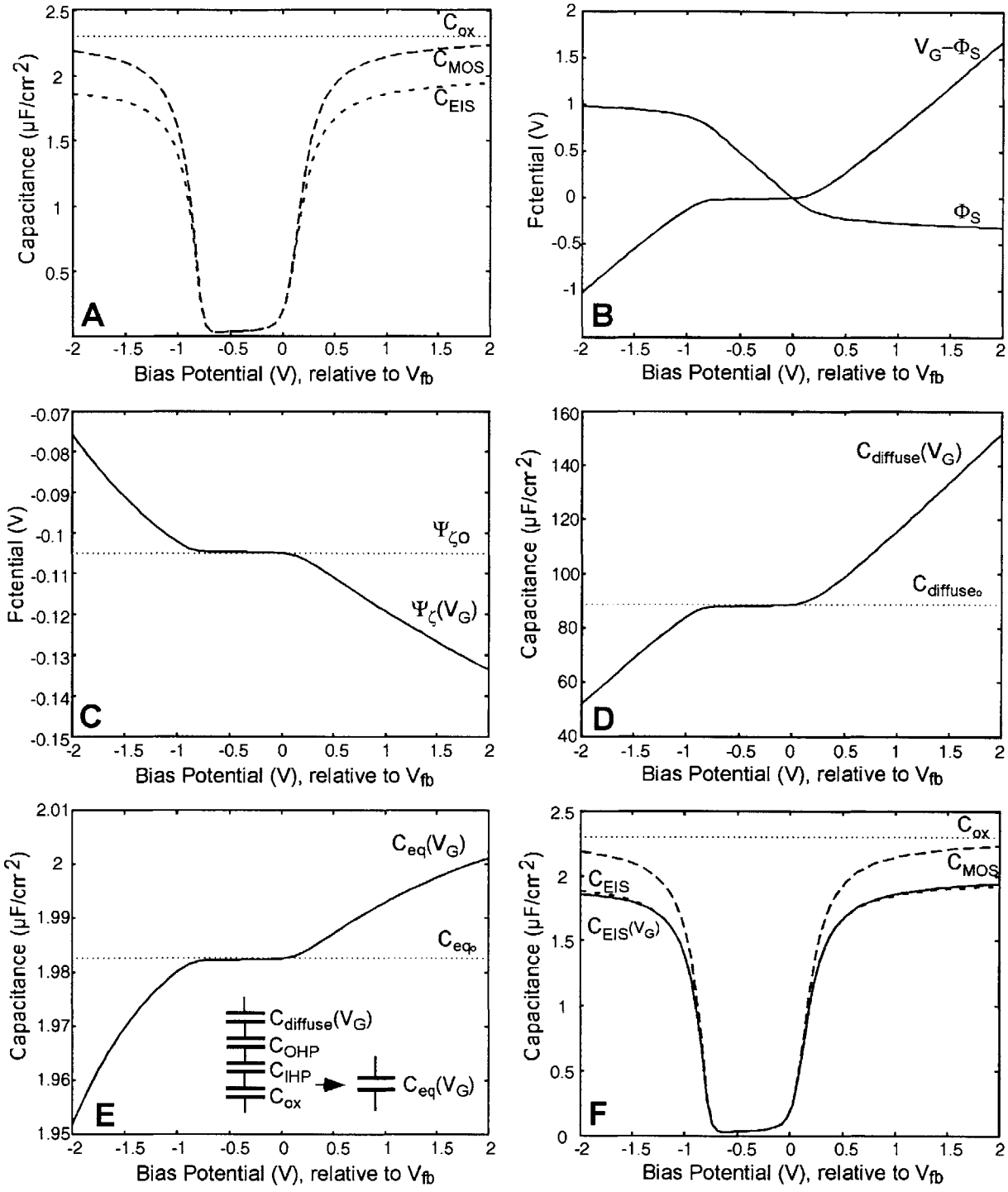

Figure 2-4: Electrolyte depletion modeling (see text for details)

$$\Psi_\zeta = \frac{C_{\text{eq}}}{C_{\text{diffuse}}} \; V \tag{2.32}$$

can be used in its differential form to relate potentials and capacitances.

$$dV = \frac{C_{\text{diffuse}}}{C_{\text{eq}}} \; d\Psi_\zeta \tag{2.33}$$

Integrating, we can relate the new zeta potential to its equilibrium value:

$$\int_0^{V_G - \Phi_S} dV' = \frac{1}{C_{\text{eq}}} \sqrt{\frac{2\epsilon_w q^2 c_o}{kT}} \int_{\Psi_{\zeta_o}}^{\Psi_\zeta} \cosh\left(\frac{q\Psi_\zeta}{kT}\right) \tag{2.34}$$

$$\Psi_\zeta(V_G) = \frac{2kT}{q} \sinh^{-1}\left[\left(\frac{qL_d C_{\text{eq}}}{2kT\epsilon_w}\right)(V_G - \Phi_S + \sinh\left(\frac{q\psi_{\zeta_o}}{2kT}\right)\right] \tag{2.35}$$

This bias-dependent potential, $\Psi_\zeta(V_G)$ is plotted in Figure 2-4C, compared with the initial, bias-independent Zeta potential.

Next, we can apply this potential to the equation for the Gouy capacitance to place bounds on the expected capacitance variation, shown in Figure 2-4D. Replacing the original Gouy capacitance with this new bias-dependent version results in the equivalent series capacitance shown in Figure 2-4E. Applying this bias dependent capacitance to our CV model results in the final characteristic, $C_{\text{EIS}}(V_G)$, in Figure 2-4F. This differs only slightly from the bias-independent model that considered the series capacitances of the electrolyte in equilibrium. There is a trend, in inversion and accumulation showing the modulation of the diffuse layer capacitance. The most important feature of this trend is the bias-dependent reduction of the capacitance in accumulation. This effect is qualitatively similar to the polysilicon depletion effect observed in ultra-thin gate dielectric MOS structures.[15,16] However, the effect for the electrolyte-gated structures shows far less deviation than the polysilicon gated structures, since the permittivity of the electrolyte solution is much greater than that of polysilicon, so the depletion effect is much weaker. While it is expected that electrolyte depletion effects will be minor for our sensor configuration, it is unclear how this change in the local electrochemical environment could affect biomolecules on the surface.

Although several simplifications were made in the above model, it places an upper bound on the effect we expect to see from electrolyte depletion effects. This modeling emphasizes the difficulty in predicting the CV characteristics of an EIS system with a thin oxide gate dielectric. Among

[16]R. Rios, N.D. Arora, and C.-L. Huang. "An analytic Polysilicon Depletion Effect Model for MOSFET's" *IEEE Electron Device Letters* **15** 129 (1994).

other effects, the CV response will depend on variations in surface chemical equilibria, the variable nature of the gate oxide thickness, the surface condition of the chemically grown oxide, variations in buffer conditions, temperature, etc. Nevertheless, there are several conclusions that can be drawn from this exercise. First, this model predicts that IHP, OHP, and diffuse layer capacitances add in series to the oxide capacitance such that a smaller gate capacitance is observed than is predicted for the ideal gate insulator. Second, the effect of bias potential on the charge distribution at the electrolyte-insulator interface is small for moderate voltage excursions. In depletion and weak inversion, the electrolyte depletion effects are minimized since additional potential is dropped over the silicon depletion region. Only minor electrolyte depletion effects are expected in inversion and accumulation regimes.

This analysis can be generalized to describe depletion effects in the electrolyte solution by considering the capacitance of the diffuse space-charge layer over a range of Zeta potentials and buffer conditions. The diffuse layer capacitance is plotted versus Zeta potential in Figure 2-5A for ionic concentrations between 0.1 mM and 100 mM, where C_{IHP}, C_{OHP} C_{ox} are also plotted for comparison. The effect of this bias-dependent diffuse layer capacitance on the total series capacitance, C_{eq} in equation 2.31, is shown in Figure 2-5B for various Zeta potentials. First, it can be seen that lower ionic concentrations create smaller diffuse-layer capacitances, which in turn affect the total series capacitance to a greater degree. This trend is analogous to dopant concentration scaling in semiconductor, where lower doping levels create larger space-charge regions, and a greater voltage dependence. Second, the diffuse layer capacitance reaches a minimum at a Zeta potential of zero. Physically, this corresponds to the sensor being in solution whose pH is the pH of zero charge for the oxide. Zero Zeta potential implies no surface charge and zero surface potential. For silicon dioxide, the pH of zero charge is around pH 3. The modulation of the series capacitance takes place for Zeta Potentials a few hundred millivolts around the zero charge condition. So we expect less bias-dependence of the series capacitance at high pH values, and when there is a high surface charge density.

To examine how the Zeta potential-dependence of the diffuse-layer capacitance maps to the capacitance-voltage characteristic of the entire EIS system, I have simulated the CV response for several ionic concentrations and initial zeta potential values. These are shown in Figure 2-6. For high ionic concentration, and high surface charge conditions, there is electrolyte depletion effect. However, at low concentrations, and lightly charge surfaces, there is some bias-dependent electrolyte depletion effect. This primarily affects the accumulation capacitance value. For low-surface charge

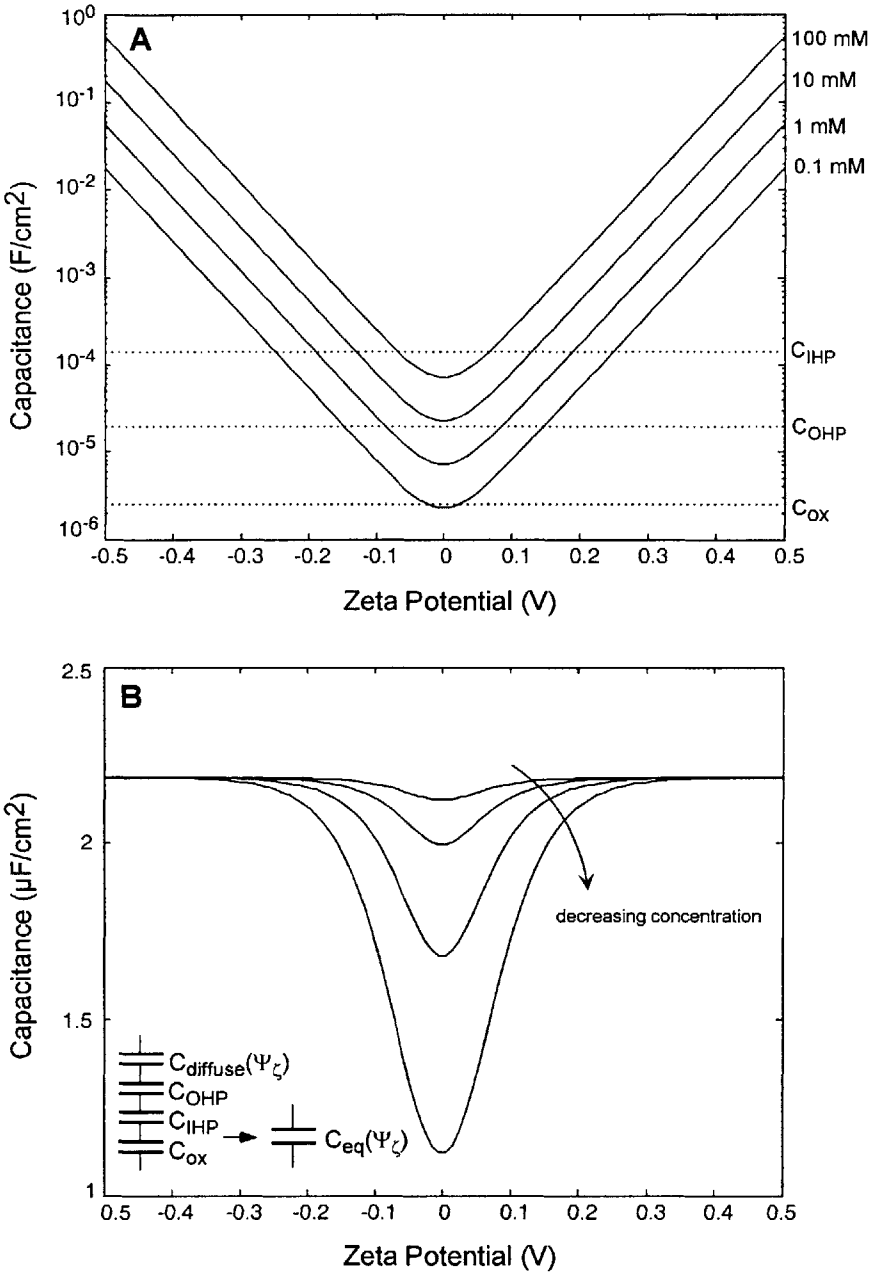

Figure 2-5: Total series capacitance of oxide and electrolyte capacitances, modeled over a range of surface potentials and electroltye concentrations

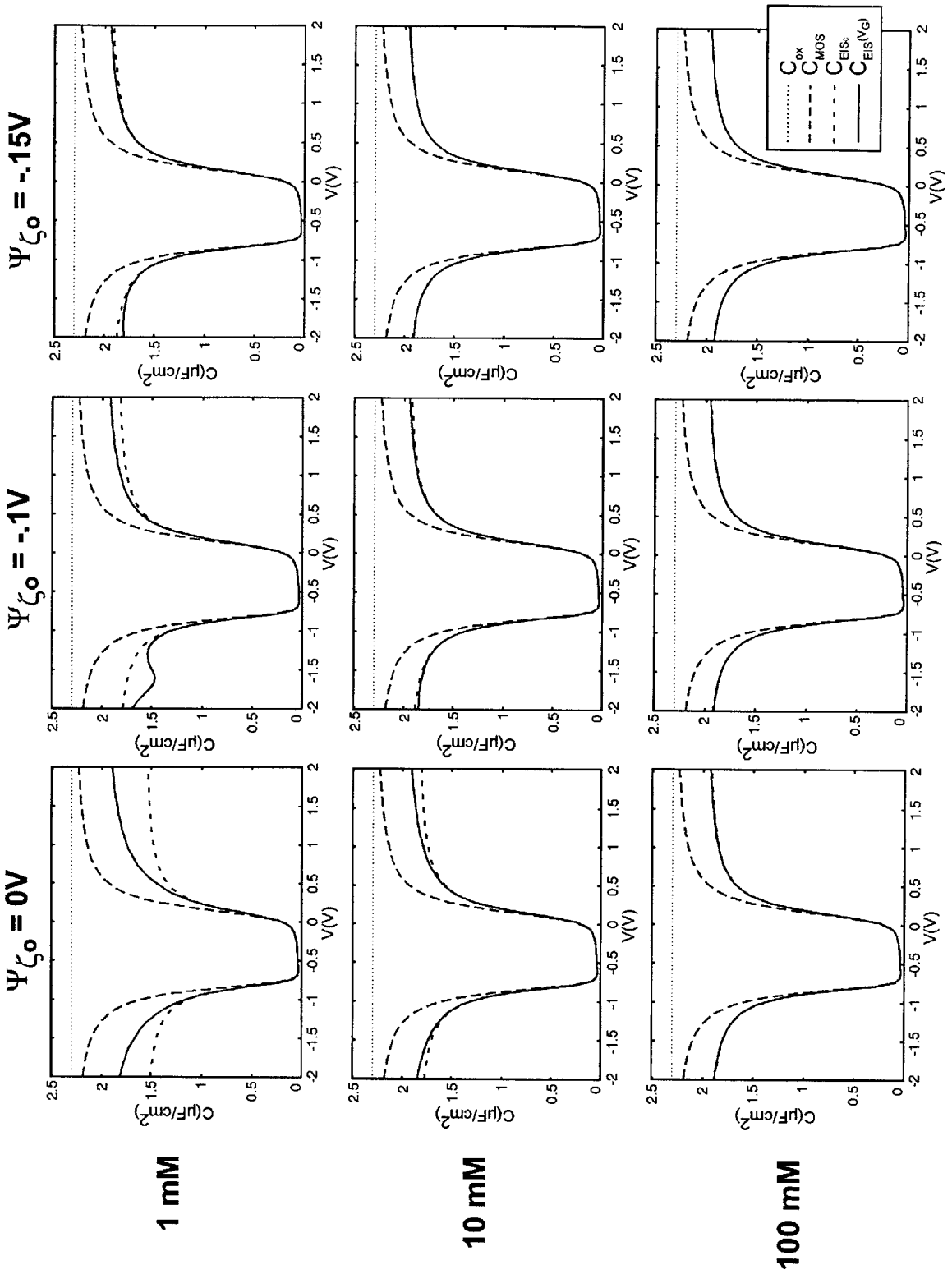

Figure 2-6: CV characteristics accounting for electrolyte depletion effects
CV characteristics were modeled for a range of ionic concentration and starting Zeta potentials.

conditions, the apparent accumulation capacitance will be higher than predicted by assuming a bias-independent depletion-layer capacitance derived from the equilibrium zeta potential. This is because the bias potential increases the diffuse-layer capacitance at higher absolute zeta potentials.

For pH values in the biological range, pH 6-9, Zeta potentials will be between -.1 and -.2 V. For buffer conditions typically used in experiments, in the 1-100 mM range, this modeling work predicts that there will be little effect on the CV curve from bias-depedent electrolyte depletion effect. Since the silicon capacitance quickly dominates the capacitive response of the device when there is a silicon space-charge region, the dC/dV sensitivity sees little effect from the electrolyte depletion.

Chapter 3

Device Design and Fabrication

In this section, the geometry of the sensor used in this work will be introduced. Relevant design criteria will be discussed. An overview of the microfabrication process will be given.

In the present work, sensors are fabricated at the tips of free-standing cantilevers, forming a microprobe whose tip acts as a potentiometer. A cross-section of this design is shown in Figure 3-1. The microprobe design enables the sensors to access small volumes of analytes. The sensors are packaged in a small-volume, closed fluid cell, and the cantilever positions the sensors to sample analyte in the center of the flow stream, where flow is most uniform. The cantilever geometry further enables a simple method for individually functionalizing sensors by introducing each cantilever into a distinct micropipette which delivers a distinct type of probe molecule to each sensor. Purely potentiometric measurements are made by the sensor; mechanical bending[1,2] or resonance are not considered.

3.1 Microfabrication

Most of the sensor processing was accomplished using established, high-yield microfabrication processes. Fabrication begins with silicon-on-insulator wafers, with a 2-micron silicon device layer, and 1 micron of buried oxide. The sensor is fabricated from the silicon device layer, and the handle wafer is used as a supporting die after the cantilevers are released. Conventional, batch micromachining techniques are followed by post-fabrication surface modifications to achieve an extremely

[1] J. Fritz, M.K. Baller, H.P. Lang, H. Rothuizen, P. Vettiger, E. Meyer, H.-J. Güntherodt, C. Gerber, and J.K. Gimzewski. "Translating biomolecular recognition into nanomechanics." *Science* **288** 316 (2000).

[2] C.A. Savran, A.W. Sparks, J. Sihler, J. Li, W. Wu, D.E. Berlin, T.P. Burg, J. Fritz, M.A. Schmidt, and S.R. Manalis. "Fabrication and characterization of a micromechancical sensor for differential detection of nanoscale motions." *Journal of Microelectromechanical Systems* **11** 703 (2002).

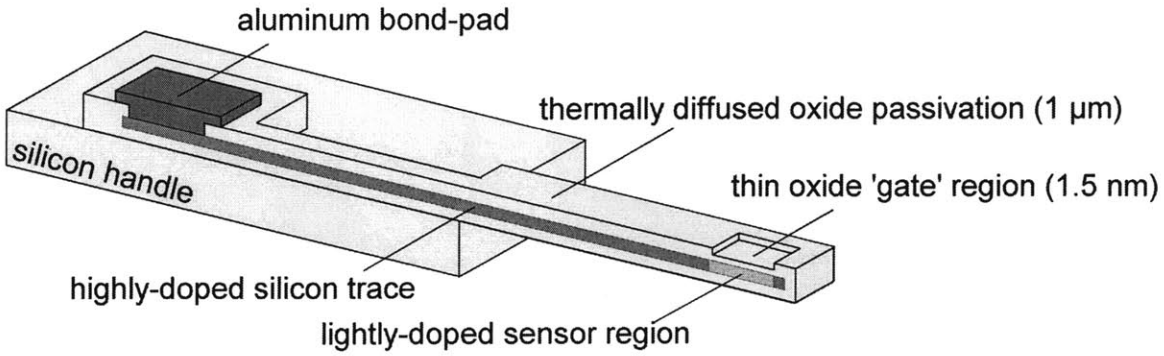

Figure 3-1: Device schematic showing cross-section and geometry

thin gate oxide. A ~1-micron thick layer of field oxide passivates the remainder of the structure. The sensor area is formed by a region of lightly doped silicon passivated with a silicon dioxide gate. This sensing area is surrounded by heavily doped silicon, forming an electrical trace between the sensor and contact pad on the die. The cantilever geometry simplifies the post-fabrication etching steps, since they can be performed exclusively at the cantilever tips, without endangering other features (electrical connections, etc.) on the die.

Much of the work concerned with the design and fabrication of field-effect biosensors has been presented elsewhere.[3] This work produced sensors that are robust through multiple cleaning and experimentation cycles, and this robustness critically enabled the developments presented in this thesis. I will present a brief overview of this work here to familiarize the reader with several design decisions which laid the foundation for the continuing work with these sensors.

3.2 Process Considerations

The primary design consideration was the passivation of the electrical trace connecting the sensor at the tip of the cantilever to the metal wire-bonding pad on the die. Previous devices were observed to easily develop electrical shorts between the solution and the electrical trace running the length of the cantilever, resulting in destruction of the sensor.[4] Many sensors failed after cleaning in acid solutions between experiments. A more robust electrical trace was fabricated by using heavily-doped silicon along the length of the cantilever, allowing the structure to be passivated with thermally-

[3]E.B. Cooper. *Design, Fabrication, and Testing of a Scanning Probe Potentiometer.* Master's Thesis, Massachusetts Institute of Technology, Cambridge (2000).

[4]S.R. Manalis, E.B. Cooper, P.F. Indermuhle, P. Kernen, P. Wagner, D.G. Hafeman, S.C. Minne, and C. F. Quate. "Microvolume field-effect pH sensor for the scanning probe microscope." *Applied Physics Letters* **76** 1072 (2000).

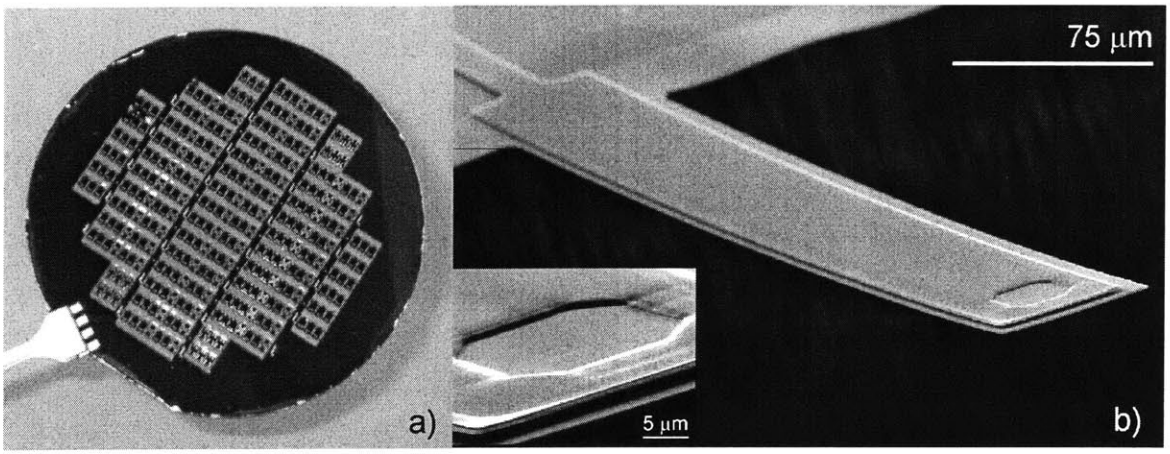

Figure 3-2: Microfabricated Sensors
A: Optical micrograph of released wafer of devices. B: Scanning electron micrograph of individual sensor

grown silicon dioxide. These sensors have proven to be robust to cleaning methods used between experiments through multiple cleaning and experiment cycles.

A secondary consideration was the balance of stress at the oxide-silicon interfaces on the top and bottom of the cantilever. The interface between silicon and thermally grown silicon dioxide typically has 0.2 to 0.3 gPa compressive stress, which can cause significant beam deflection if left uncompensated. In order to minimize out-of-plane deflection of the cantilever, it is necessary to match the stress induced at the top side of the cantilever with that at the silicon-buried oxide (BOX) interface. This stress can be controlled by matching the thickness and the diffusion conditions of the top-side passivation oxide to those of the BOX.

Processing was simulated using TSUPREM software to optimize doping levels and film growth parameters to achieve desired electrical performance. Devices were fabricated in the Microsystems Technology Laboratories. Fabricated devices are shown in Figure 3-2 and a complete microfabrication process description is given in Appendix A.

3.3 Geometry Considerations

The portion of the silicon that contributes to the measured depletion capacitance is composed of uniformly doped silicon, at the background doping level of the wafers ($\sim 10^{15}\text{cm}^{-3}$). The uniform doping level enables a straightforward calculation of anticipated CV characteristics. The boundaries of this region are defined laterally by regions of higher doping ($\sim 10^{18}\text{cm}^{-3}$). In the fabrication of

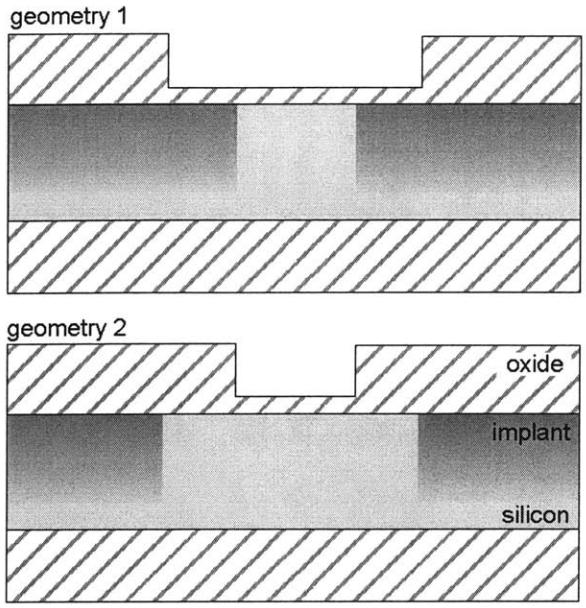

Figure 3-3: Schematics of two device geometries considered

the sensors used in this work, a window over the lightly doped sensing region is cut into the thick field oxidation and the gate oxide is subsequently thermally grown. Two designs were evaluated when considering how the field oxide and doping regions should overlap. These two designs are shown in Figure 3-3. In conventional MOS fabrication, this issue does not arise, since self-aligning the gate dielectric with ion-implantation is both convenient and necessary for high-performance devices.

In the previous sensor designs,[3] the window cut in the field oxide was larger than the doping window, as shown in the first geometry in Figure 3-3. Applications under consideration at the time included measurements with immobilized lipid bilayers or metabolic measurements of small numbers of adherent cells. In each case, there was concern that discontinuities at corners of the field-oxide trenches would adversely affect measurements. The doping window was therefore designed to be smaller than the cut in the field oxide so that it would be exposed only to uniform central region. As we move toward molecular scale assays, the primary design concern has been to minimize parasitic capacitances which distort and obscure the depletion capacitance in the gate region. CV curves were therefore calculated for the two geometries shown in Figure 3-4 and then compared to the ideal 1-D MOS CV curve, which assumes uniform doping level, and no edge effects at the interface between different doping levels. A carrier density of $N_{d_{low}} = 10^{15}\#/cm^3$ was used for the sensing

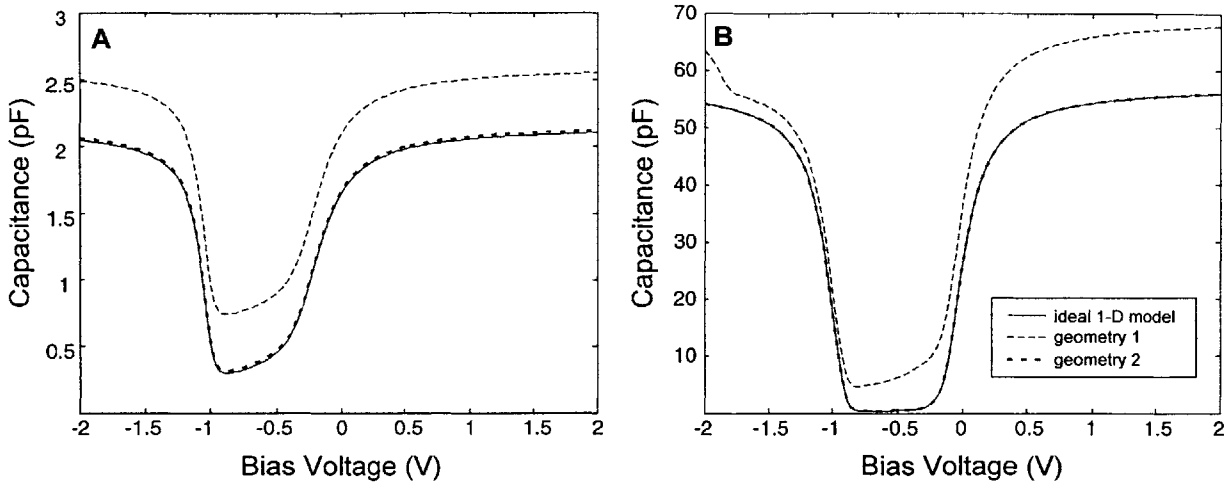

Figure 3-4: CV models for proposed sensor geometries.
A) for sensors with 40 nm gate oxide. B) for sensors with 1.5 nm gate oxide. The reference model is the ideal 1-D MOSCAP with a gate area of 2500 μm^2, dopant density of N_{dlow}, and the gate oxide thickness. The region framing the gate area is a 5-μm wide band surrounding the gate, which has a total area of 1100 μm^2. The first geometry was modeled as the reference model in parallel with a MOSCAP with N_{dhigh} and the gate oxide and the area of the frame. The second geometry was modeled as the reference model in parallel with a MOSCAP with Ndlow and the field oxide.

area and $N_{d_{high}} = 5 \times 10^{18} \#/cm^3$ was used for the highly-doped region. The field oxide thickness was 1 μm and results are shown for the as-fabricated 40 nm gate oxide thickness Figure 3-4A, as well as the final gate oxide thickness of 1.5 nm Figure3-4B.

Geometry 1 causes significant capacitive offset due to the relatively large parallel capacitance. For devices with 40 nm gate oxide, the offset capacitance is roughly constant over the voltage range of interest, and does not significantly change the form of the CV curve. For the thin gate oxide, the distortion is significantly more pronounced. Besides the parallel capacitive offset, the slope in depletion to mild inversion is altered. While the first geometry causes distortion the the CV curves, the steepest depletion-regime slope, i.e. the sensitivity in the operating regime of interest, is affected little. The second geometry was chosen to simplify data interpretation.

3.4 Post-Fabrication Gate Modification

To increase the surface potential response of the EIS structure, sensors underwent a post-fabrication etch procedure to thin the gate oxide. Typically, devices were stripped of the ~40 nm-thick thermally diffused gate oxide in Buffered Oxide Etch (BOE), a buffered solution of HF, for ~25 seconds.

Sensors were etched by dipping the cantilever tips into a small volume of BOE. This results in etching of the field-oxide as well, but a 40 nm variation in a micron-thick field oxide has negligible effect on the CV characteristics of the sensor. Cantilevers were rinsed for 2 minutes in nanopure de-ionized water and air dried. The devices were subsequently exposed to *piranha*, a 1:3 mixture of hydrogen peroxide and sulfuric acid, for 90 seconds. Devices were again rinsed in nanopure DI water for 2 minutes and air dried before being introduced into the fluid cell for measurements.

Between experiments, sensors were cleaned according to the following sequence:

- piranha: 90 seconds
- DI rinse: 120 seconds
- HF dip: 5 seconds
- DI rinse: 120 seconds
- piranha: 90 seconds
- DI rinse: 120 seconds

Chapter 4

Device Characterization

This chapter describes electrical characterization of sensors applied through the remainder of this thesis. EIS sensors are compared to MOS structures in order to identify microfabrication artifacts. The surface potential, noise, leakage, and drift of the sensors is then characterized and compared to previously reported EIS devices.

4.1 System Overview

4.1.1 High-Frequency CV Method

The capacitance of our system, and subsequently electrolyte-insulator interface potential, is measured by a high-frequency CV measurement method, typically used in integrated circuit diagnostics. In this method, a small sinusoidal voltage,

$$v(t) = V_{\mathrm{AC}} \cos(\omega t) \tag{4.1}$$

is applied across the capacitor and measuring the current response:

$$i(t) = |H(j\omega)| V_{\mathrm{AC}} \cos(\omega t + \Phi) \tag{4.2}$$

where the transfer function that relates these two is

$$H(j\omega) = \frac{i_{\mathrm{out}}}{v_{\mathrm{in}}} \tag{4.3}$$

the admittance of the structure. The amplitude of the current response is the product of the voltage amplitude and the magnitude of the admittance, which is expressed by

$$|H(j\omega)| = \sqrt{\left(\Re(H(j\omega))\right)^2 + \left(\Im(H(j\omega))\right)^2} \tag{4.4}$$

The phase shift of the current response relative to the input voltage is

$$\Phi = \arctan \frac{\Im(Y(j\omega))}{\Re(Y(j\omega))} \tag{4.5}$$

For a purely capacitive element, $Y = j\omega C$, the current response will be

$$i(t) = \omega C V_{rmAC} \cos(\omega t + \frac{\pi}{2}) \tag{4.6}$$

In this ideal case, the amplitude of the current response is directly proportional the capacitance, frequency, amplitude of excitation. The phase of the current response leads the input voltage by 90 degrees.

For device characterization and measurements, the small-signal AC voltage described above is superposed on a DC voltage which is used to bias the sensor in various regimes of operation. CV characteristics are measured by sweeping the DC bias voltage slowly, while measuring the small signal capacitance at each bias voltage.

In reality, series resistances complicate the straight-forward capacitive measurement described above, and the above simplified model no longer applies at moderate frequencies. This non-ideality will be characterized in the latter part of the chapter, and measurement consequences will be discussed.

4.1.2 Test Setup

For testing and experimentation, EIS sensors are immersed in an electrolyte, and a Ag/AgCl wire is used as a counter electrode in solution. Typically, a 100 mV AC voltage, at 1-10 kHz is supplied to the counter-electrode to generate an AC charging current. The charging current is amplified with a current pre-amplifier (Keithley 428), which supplies a bias voltage to the sensor. The root-mean-square (RMS) amplitude is monitored with a lock-in amplifier (Stanford Research Systems SR830 DSP), while gain and offset are adjusted either with a differential amplifier or with the offset and expand capabilities of the lock-in amplifier. The amplified signal is captured with Labview data acquisition hardware and software. This measurement arrangement is shown in Figure 4-1. For CV characterization, the differential amplifier is bypassed.

4.1.3 Packaging

The fluidic chamber used in this work is shown in Figure 4-2. It is composed of 3 separate layers, which can be bound together to tightly seal the chamber. Individual sensor dice are broken out

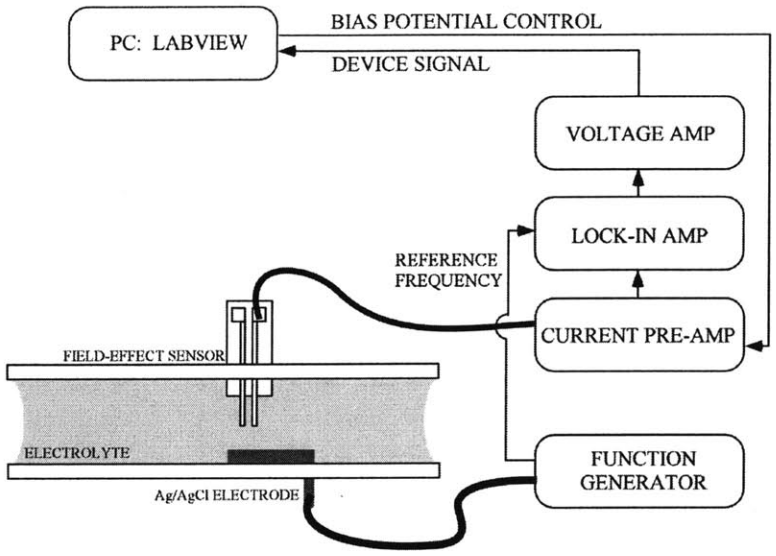

Figure 4-1: Schematic representation of readout

of the wafer from which they were fabricated, and bonded to a ceramic chip that has gold bond pads to which electrical leads are soldered. This assembly is fixed into a delrin frame (top layer in Figure 4-2, left) with silicon RTV (Dow), which is suitably inert. The volume of the fluid chamber is defined by the thickness of a rubber o-ring held in place by a thin plastic frame (center layer). Inlet and outlet channels are machined into a plastic block (bottom layer). The entire assembled device, including electrical and fluidic connections, is shown in Figure 4-2,right.

4.2 Fabrication Characterization

Before beginning biomolecular assays, the electrical performance of the sensors was characterized. As a starting point, cantilever-based EIS sensors were compared with MOS structures that were fabricated on the same wafer, and to the same geometry (see Chapter 2), in order to characterize the electrical performance of the sensors, and to identify and isolate effects caused by the fabrication process from those arising because of the electrolyte portion of the EIS sensor.

Capacitance versus voltage curves were measured and compared to a theoretical CV curve calculated for an ideal 1-D MOS structure.[1,2]

[1]E. H. Nicollian and J. R. Brews. *MOS (Metal Oxide Semiconductor) Physics and Technology.* Wiley. New York. (1982).

[2]J. A. del Alamo. *Integrated Microelectronic Devices: Physics and Modeling* Unpublished manuscript (2000).

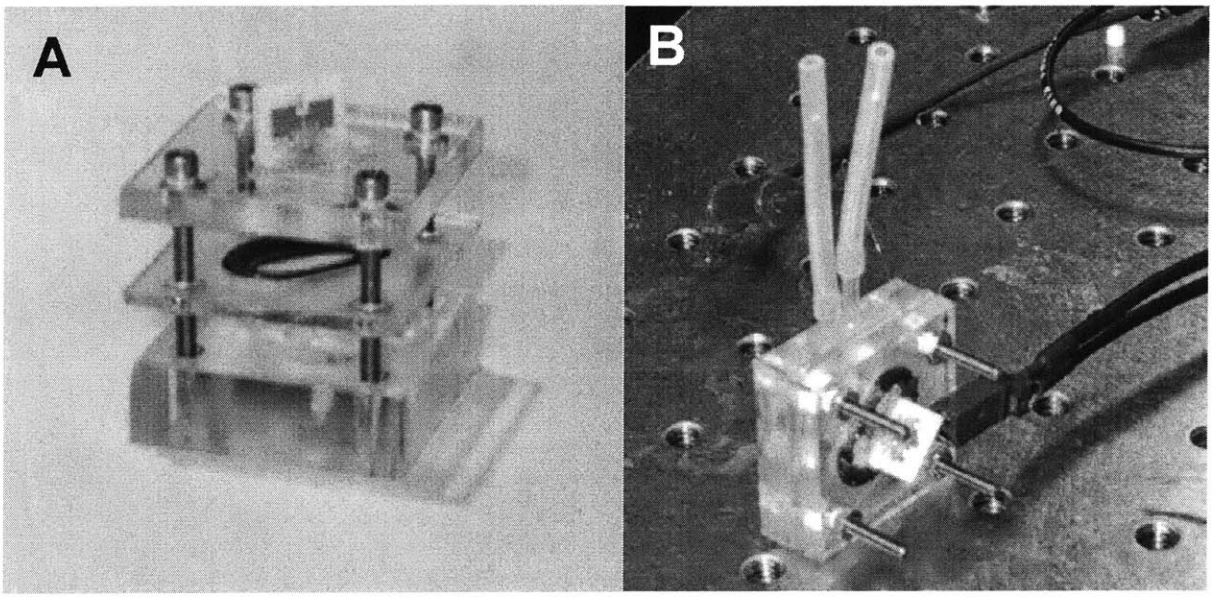

Figure 4-2: Fluidic chamber used for EIS cell

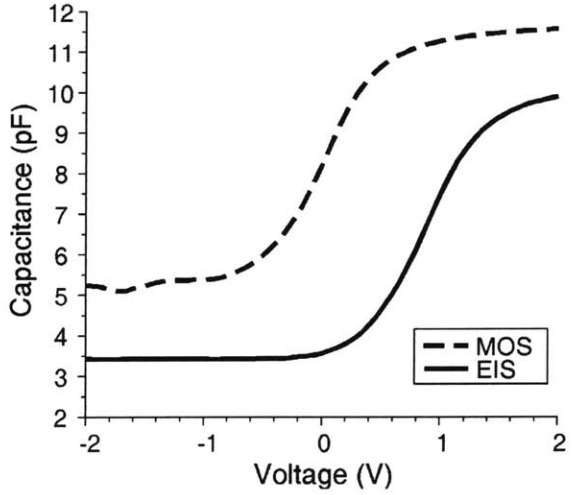

Figure 4-3: Measured MOS and EIS CV characteristics

EIS measurements made by immersing only the cantilever tip[3] in 100 mM sodium phosphate buffer at pH 7.05. The measured CV characteristics are shown in Figure 4-3. Both MOS and EIS curves show significant capacitance appearing in parallel with the sensor region. In the case of the EIS structure, the parallel capacitance is caused by the portion of the cantilever immersed in solution. This capacitance is formed between the electrolyte and the silicon trace, with 1 μm thick field oxide as the dielectric. The electrolyte contacts both the front and the back of the cantilever, creating a parasitic capacitance between the electrolyte and the highly doped silicon electrical trace. The capacitive offset in the MOS structure is caused similarly by the region where the gate contact extends beyond the sensor surface, forming a capacitor between the gate aluminum and the highly doped silicon trace, with 1 μm field oxide as the dielectric.

Ideally, we would like to compare our devices to simple models whose only parameters are oxide thickness and doping level. However, the unknown offset capacitance in each case complicated the process of extracting fabrication parameters. Ideal, 1-D, low-frequency MOS curves were calculated and fit to the measured data based on the assumption that the bulk dopant density in the gate silicon portion of these two sensors would be similar, while the gate oxide thickness measurements taken during fabrication indicated thicknesses between 405 $\pm$ 15 Angstroms. Plots of each curve, with fit data is show in Figure 4-4. In each case, the measured curves were offset along both the capacitance and voltage axes so that they could be overlayed with theoretical curves to analyze quality of fit.

For the MOS structure, a sheet resistivity of .65 ohm-cm (corresponding to a dopant density of 6.4×10^{15} $\#/cm^3$) and a gate thickness of 400 Å provided a good fit to the slope and amplitude of the curve. The ideal 1-D model used here is a low-frequency model and it neglects the effects of interface charge, and fixed and mobile charges in the oxide, which are artifacts of the microfabrication environment. The MOS curve showed a 3.1 pF offset capacitance, and a +.375 V flat-band voltage shift, corresponding to an interface charge density of -3.23×10^{-8} C/cm^2, or 2.02×10^{11} $charges/cm^2$. From the direction of the shift, this corresponds to negative charge in the oxide. This is a surprisingly high quantity of interface charge since a forming gas anneal was performed on these devices. The forming gas anneal typically enables the out-diffusion of defects at the $Si - SiO_2$ interface.

The dopant density of 6.4×10^{15} $\#/cm^3$ was assumed for the EIS structure, and an oxide thickness of 380 Å provided a good fit to the amplitude of the curve. The EIS curve had 1.2 pF

[3]Note that this is a different test arrangement than the fluid chamber described in section 3.1.2

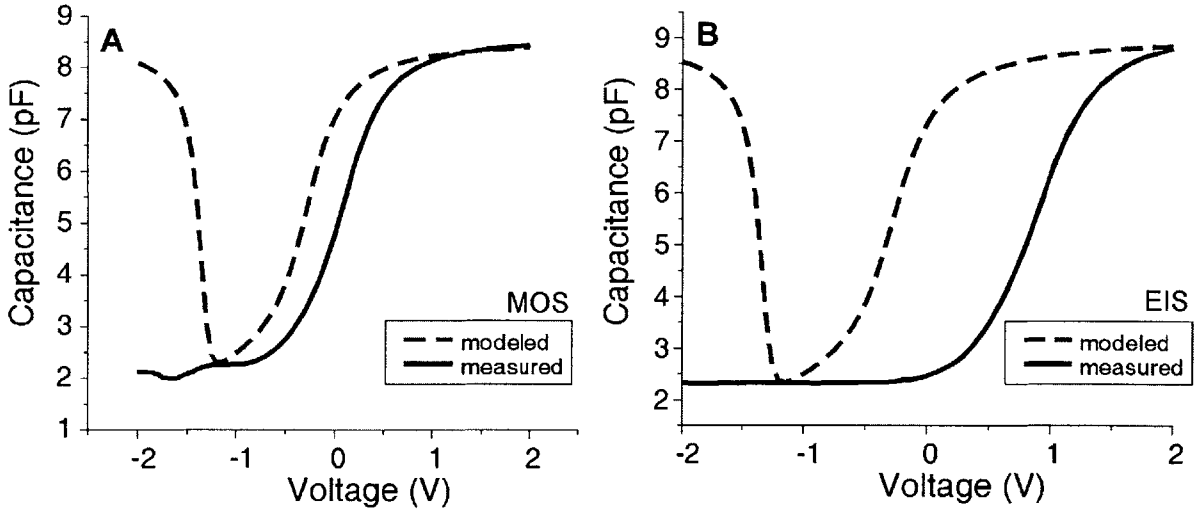

Figure 4-4: A) MOS and B) EIS CV characteristics overlayed with model

offset capacitance. The flatband voltage of the EIS structure was found to be 0.969 V, a +.772 V shift compared to the measured MOS structure. This is due to the sum of contributions from the electrolyte: the reference potential, potential drop in the electrolyte space-charge region, and electrochemical potnetial of the buffer, as described in Chapter 2.

4.3 Characterizing Sensors with Thin Oxide Gates

4.3.1 CV Slope: dC/dV

Our sensors are prepared by etching the gate oxide in HF, and chemically growing a thin oxide layer in piranha, as described in Chapter 3. CV characteristics measured for various gate insulator thicknesses are shown in Figure 4-5. Subsequent etching beyond 21 seconds for this device did not further alter the CV response, so we conclude that etching of the thermally grown silicon dioxide gate was complete at this point.

This yields an effective etch rate of 19 Å/s. This is somewhat higher than etch rates observed in our lab for 7:1 Buffered Oxide etch at 22.8 22.8 °C, which were found to be about 15 Å/s from ellipsometric measurements of oxide thickness after varying etch times. The etch times can be used as a rough approximation of the oxide thickness, assuming linear dependence of etch rate versus time.

The slope of the CV curve expresses a sensitivity metric of the EISCAP structure: dC/dV.

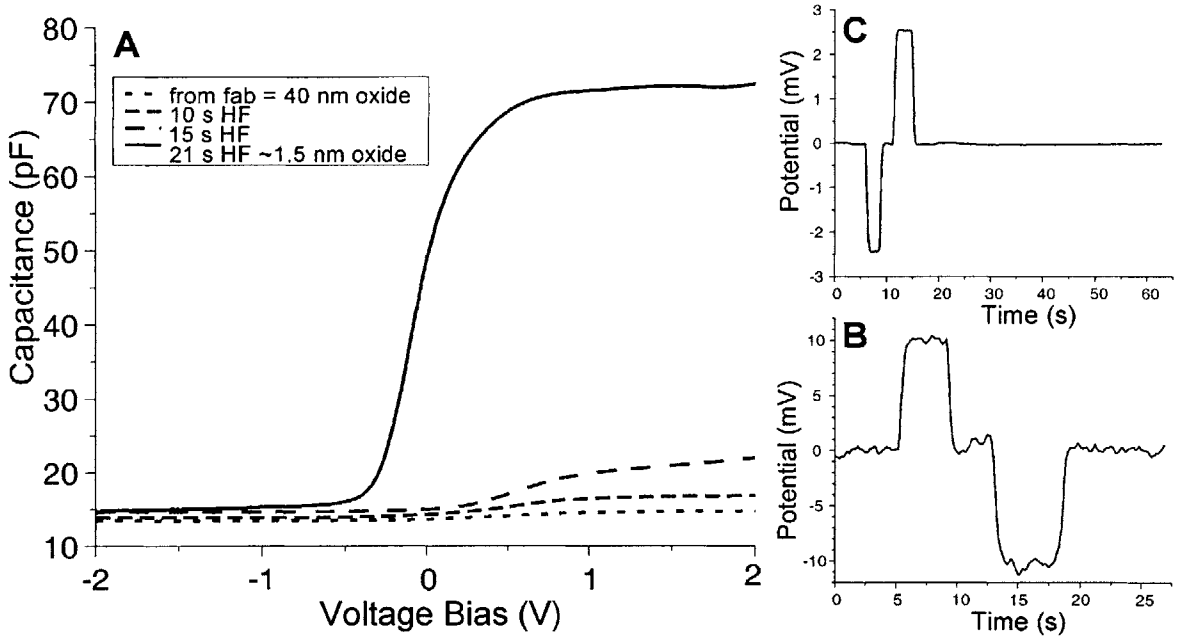

Figure 4-5: Measured characteristics of sensors with very thin gate oxide: A) CV characteristic B) Noise demonstration for sensor with 40 nm oxide C) noise demonstration for sensor with ~1.5 nm oxide.

This is analogous to the transconductance, g_m, of a FET structure (dI_{ds}/dV_G). The CV sensitivity increases from .85 pF/V for a sensor with a 40 nm thick gate oxide to 112.5 pF/V for the piranha-grown gate oxide. Sensitivity values are plotted against oxide thickness in Figure 4-6 for each of the CV curves shown in Figure 4-5. Overlayed with these data points are modeled values for CV slopes calculated for an MOS structure of equivalent dimensions and a doping level of $5 \times 10^{15}/\text{cm}^2$, using Maxwell-Boltzmann statistics for all oxide thicknesses.

4.3.2 Noise Characterization

Timecourse measurements shown in Figure 4-5B and C give a sense of the voltage resolution of sensors with various oxide thicknesses. Figure 4-5B shows data from a sensor with 40 nm gate oxide, calibrated with a voltage step of 10 mV. Figure 4-5C shows a measurement from a sensor with piranha-grown oxide, calibrated to a 2.5 mV applied voltage step. An estimate of the voltage noise over a limited bandwith is shown in Figure 4-7, showing the RMS value of 10 seconds of data sampled at 10 Hz.

To get a more accurate sense of the sensor noise, power spectral densities were measured. Figure 4-8 shows the power spectral densities for both the sensor (top) and the ceramic capacitor (bottom)

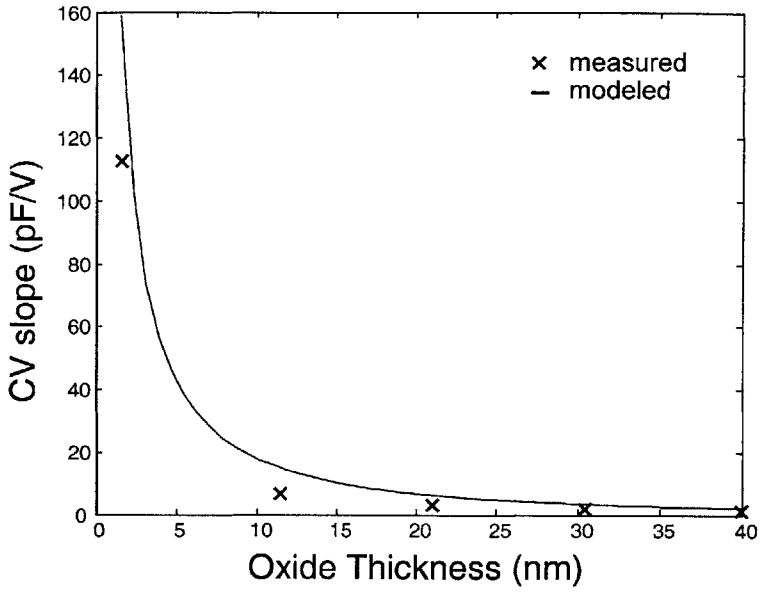

Figure 4-6: Surface potential sensitivity:
Measured dC/dV slopes were extracted from CV curves shown in Figure 4-5. Model data was derived from a 1-D MOS model with a doping level of $5 \times 10^{(}15)\#/cm^3$ and an equivalent geometry as the sensor.

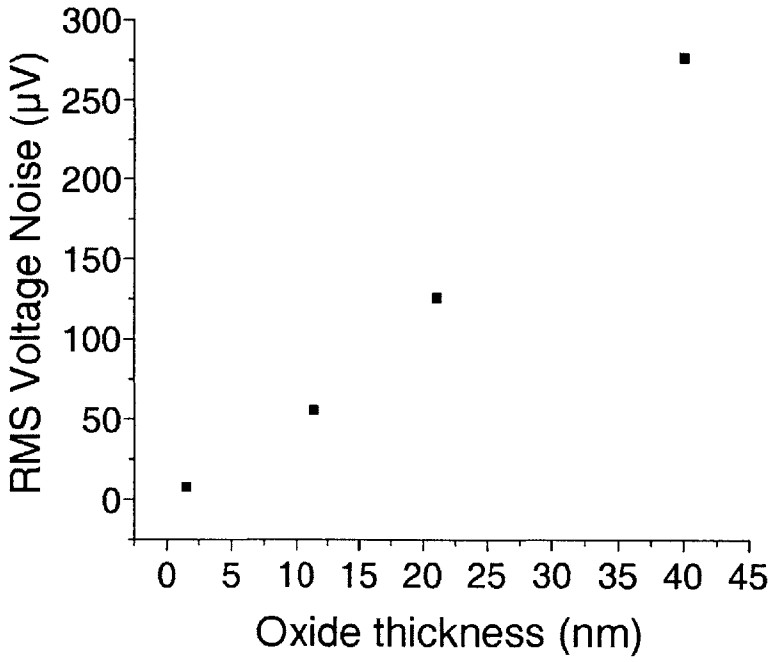

Figure 4-7: RMS voltage noise

over the frequency range of 0.01 to 10 Hz. Overall, the shape of the noise is similar in each case. Integrating over this spectrum, we find the RMS noise on the sensor to be 16.5 fF and the RMS noise on ceramic capacitor to be 42.4 fF over the frequency range 0.01 - 10 Hz. The similarities of these trends leaves little to extract about mechanisms that are unique to the EIS system and independent of our measurement setup.

It might be expected that leakage of carriers through the sensor interface may be a source of noise, or possibly a DC offset. It is not immediately obvious that a thin, chemically-grown silicon oxide layer should sufficiently passivate the sensor surface. One might expect tunneling, or a breakdown of the oxide. Such interfacial reactions would have a detrimental affect on the lifetime and stability of the sensor, as well as the stability of the surface chemistry. In particuar, local leakage could affect the local pH at the insulator-electrolyte interface, the stability of the surface biochemical functionalizatiuon, and binding events with target molecules.

The breakdown field strength of silicon dioxide is about .07 V/Å (although this is dependent on a number of factors: trap density, operating time, temperature, etc. and the breakdown process is still not well-understood).[4] For an oxide layer 1.5-2 nm thick, we would expect breakdown when ~1 - 1.5 V is applied across the oxide. This occurs at bias voltages of about $V_{FB} - 2V$ (in inversion) and $V_{FB} + 1,5V$ (in accumulation)— very moderate voltage excursions. As mentioned in Chapter 2, the work of Muller et al.[5] sets the fundamental limit of oxide gate thickness at 0.7 nm. Another limiting factor will be the density of the oxide, and bias voltages used for measurements.

The manifestation of leakage in MOS devices with ultrathin gate oxides deviates from that observed with thicker gates. Weir et al. report on observed 'soft breakdown' characteristics, whereby only small offsets in DC characteristics are observed, but an abrupt increase in noise is observed.[6] They attribute this to trap-assisted conduction through the oxide. For 2 nm oxides, they observed that stress-induced leakage current increased continuously prior to breakdown, with no catastrophic change observed following soft breakdown.

To investigate DC leakage, measurements were made over a range of DC bias points with the function generator disconnected from the system. This arrangement differed from that described at the beginning of the chpater. The Ag/AgCl wire was grounded, and bias voltages were applied

[4]Y. Tsividis. *Operation and Modeling of The MOS Transistor.* McGraw-Hill. Boston (1999).

[5]D. A. Muller, T. Sorsch, S. Moccio, F. H. Baumann, K. Evans-Lutterodt, and G. Timp. "The electronic structure at the atomic scale of ultrathin gate oxides." *Nature* **399** 758 (1999).

[6]B.E. Weir, P.R. Silverman, D. Monroe, K.S. Krisch, M.A. Alam, G.B. Alers, T.W. Sorsch, G.L. Timp, F. Baumann, C.T. Liu, Y. Ma, and D. Hwang. "Ultra-thin gate dielectrics: they break down, but do they fail?" *IEEE Electron Devices Meeting, Technical Digest 1997* 73 (1997).

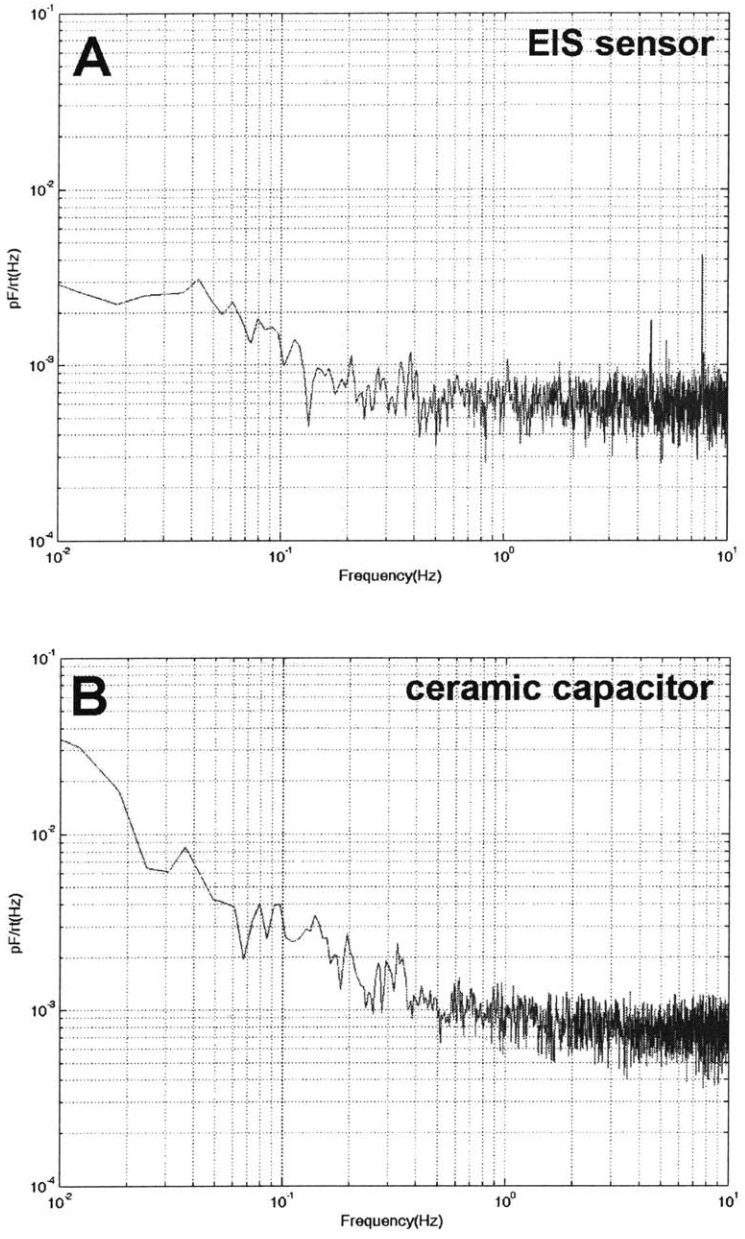

Figure 4-8: Power spectral densities for EIS sensor and ceramic capacitor
A bias voltage of .65 V was applied to the sensor, to set the total device capacitance to 39 pF. A 100 mV charging voltage was applied at 10 kHz. A 1 ms (12 dB) time constant was used on the lock-in amplifier. 10^7 gain on the pre-amp, 1 V sensitivity on the lock-in, and 50x gain applied at the lock-in. a 5 mM phosphate buffer with 10 mM NaCl at pH 6 was used as the electrolyte solution in the EIS cell. Data was sampled at 100 Hz for 1000s. The sampling rate was chosen to be lower than the update frequency of the digital lock-in, which is 512 Hz. A similar measurement was made with a 39 pF ceramic capacitor, and all other equipment settings the same.

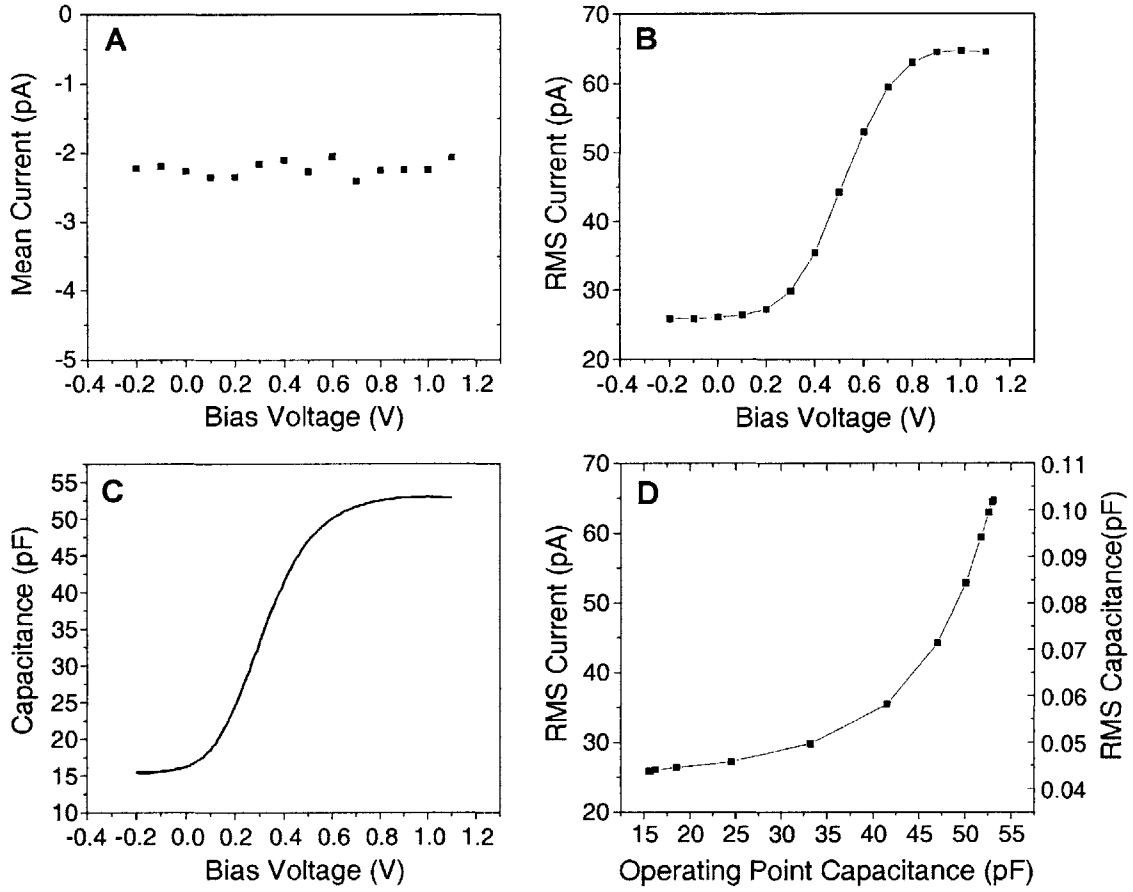

Figure 4-9: Leakage current

A) Mean leakage current vs. bias voltage. B) RMS noise current amplitude vs. applied bias voltage. C) Capacitance vs. bias voltage. D) RMS noise current and RMS noise capacitance vs. operating point capacitance. Capacitance values were derived from current values according to $C_{RMS} = \frac{i_{RMS}}{\omega V_{AC}}$.

to the back contact of our sensors through the current pre-amp. This is the same method used to apply the DC bias voltage during experiments. The gain on the pre-amp was set to 10^9, and the output of the pre-amp was fed directly to Labview, bypassing the lock-in amplifier. Measurements were made at 0.1 V intervals over the range of -.2 to +1.2 V, the range of biases typically applied to the sensor during experiments. Data was sampled at 10 kHz for 30 seconds at each bias point.

It was found that the mean current measured by this technique varied little with applied bias, as shown in Figure 4-9A. In all cases, the mean current was found to be between -2 and -2.5 pA. This is commensurate with the quoted accuracy of the current pre-amp: $\pm$ 2.5 + 3 pA (% input + offset). As a further test, the same measurement was made with a 39 pF ceramic capacitor in place of the EIS cell. One lead was grounded, and the other connected to the input of the current pre-amp. The capacitor was swept through the same bias voltages applied to the EIS sensor. This measurement showed about -1.9 pA mean current, commensurate with measurements of EIS cell. Measured current values in either case are limited by the pre-amp accuracy and reveal nothing particularly unique to the sensor. We can, however, conservatively concluded that the leakage current through the sensor is not more than a few picoAmps, or on the order of 10^{-8} A/cm^2. This can be compared to reported leakage currents through experimental poly-gate MOS structures with ultrathin silicon dioxide gates. Leakage currents of 10^{-12} A/cm^2 have been measured for 35 Å silicon dioxide gates, and 10 A/cm^2 for 15 Å gate oxide.[7] The charge transfer at the electrolyte gate differs significantly from that at the polysilicon gate. The energy barrier associated with the transfer of electronic charge to ionic charge would accounts for the lower leakage current observed in comparison to polysilicon-gated structures. Higher current levels would be expected if Faradaic processes were occurring at the interface. We conclude, therefore, that the thin oxide gate is suitably stable for assay development, over the voltage range of interest.

The RMS amplitude of the current, however, varied significantly with applied bias, as shown in Figure 4-9B. The RMS noise specification quoted for the current pre-amp is ~10 pA, and the resolution of Labview sampling corresponds to 1 pA for these conditions. The characteristic of the noise amplitude follows the high-frequency CV curve. A CV curve, measured by the standard AC technique used elsewhere in this thesis, is shown in Figure 4-9C. This CV measurment was used to translate bias voltages to operating point capacitance values. On this scale, noise current varies monotonically, though not linearly, with the capacitance of the sensor. This non-linearity may be

[7] D.A. Buchanan. "Scaling the gate dielectric: Materials, integration, and reliability." *IBM Journal of Research and Development* **43** 245 (1999).

due to the difference in excitation of the two measurements. For the CV measurement, a voltage is applied at a specific frequency, and the response is filtered with the lock-in amplifier. For the noise current measurement, both the excitation and measurement bandwidths are much greater. The noise current can be considered the response to a *very small* small-signal excitation, and appears to be dominated by high frequeny noise.

Noise current measurements can be scaled by typical operating conditions to get an equivalent noise capacitance for the system, according to equation 4.6. For a 100 mV AC voltage at 1 kHz, the effective noise capacitance can be plotted as a function of the bias capacitance shown on the right-hand axis of Figure 4-9D. From this perspective it can be seen that the equivalent voltage noise for a measurement will depend not only on the slope of the CV curve, but also the operating point where measurements are made. As a practical consideration for the readout electronics currently used, it is advantageous to operate at as low a capacitive bias point as possible within the linear regime of the CV curve.

4.3.3 Oxide Characterization

The CV characteristics presented in Figure 4-5 show an accumulation-regime capacitance that is nearly independent of bias voltage. These show negligible leakage and electrolyte depletion effects. Not all sensors showed such model accumulation-regime behavior after chemical growth of a thin oxide layer. As shown in Figure 4-10, there can be a great deal of variation among CV characteristics of a sensor over several cleaning cycles. This is most likely due to variability in temperature and mix ratio of the piranha solution. These factors are difficult to control working in small volume.

The chemical oxidation of silicon in piranha (also known as SPM for sulfuric/peroxide mix) is a topic of current research of particular importance to the development of effective cleaning strategies for microfabrication. Unlike thermal oxidation, which has been well-characterized, the process of wet chemical oxidation is not well understood. It is believed that the process is initiated by oxidative attack by a strongly oxidizing radical, such as the hydroxyl radical. Subsequently, oxygen diffuses through the surface layer to the receding $Si - SiO_2$ interface. The rate of oxidation dramatically slows down as the piranha and the silicon surface reach electrostatic equilibrium, resulting in an oxide a few monolayers thick,[8] typically 0.6 to 2.0 nm thick.[9] Okorn-Schmidt has used open-circuit

[8]E.P. Boonekamp, J.J. Kelly, J. van de Ven, and A.H.M. Sondag."The chemical oxidation of hydrogen-terminated silicon (111) surfaces in water studied *in situ* with Fourier transform infrared spectroscopy." *Journal of Applied Physics* **75** 8121 (1994).

[9]H.F. Okorn-Schmidt. "Characterization of siliocn surface preparation processes for advanced gate dielectrics." *IBM Journal of Research and Development* **43** 351 (1999).

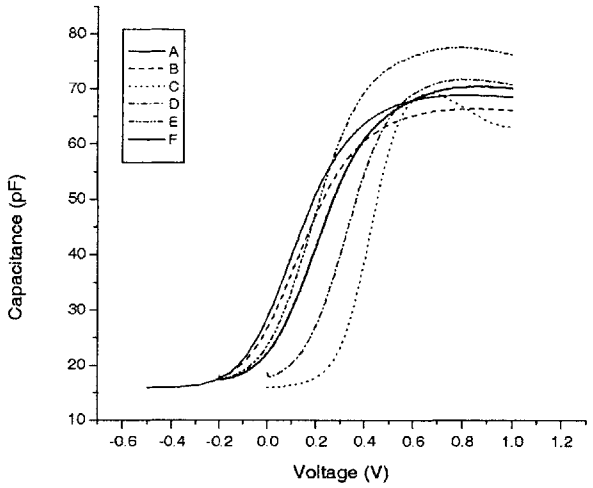

Figure 4-10: Variation in chemical oxide growth

CV curves were measured for a single device after 6 successive cleaning cycles. Variation in CV characteristics are caused by variations in temperature and mixing ration of piranha solution used to chemically grow the gate oxide.

potential measurements to monitor *in situ* the oxidizing power of piranha at various temperatures.[9] Not only the oxide thickness, but also the equilibrium interface potential were found to be strongly dependent on temperature of the piranha. Oxide thicknesses determined by ellipsometry were found to be 0.6 nm after exposure to piranha at 21 C, compared with 1.1 nm for piranha at 95 C. This range corresponds oxide capacitances of 3 to 5.5 $\mu F/cm^2$. The observed variablity in accumulation regime capacitances shown in Figure 4-10 is less dramatic: the maximum capacitance is $\sim$30

As a point of comparison, we have investigated the CV characteristic of devices which have been stripped of oxide in an HF solution, but have not had a new oxide chemically grown in piranha. The results of this are shown in Figure 4-11. The black curve was produced after the sensor underwent a typical piranha-HF-piranha cleaning procedure. The same device was then removed from the fluid cell, cleaned in piranha, and stripped in HF. The resulting CV curve is shown in red. It is likely that some form of native oxide formed during this handling. The hydrophobic surface that is created when silicon oxide is removed from the silicon surface in hydrofluoric acid is known to have a low surface state density, due to hydrogen passivation of the silicon surface. This passivation layer can be stable over a period of hours, although this stability is only exhibited when the hydration is uniform and complete. Typically, etching in HF produces mixed surfaces with both hydrophilic and hydrophobic regions. Unless careful rinsing and drying procedures are followed, the surface can re-oxidize during these subsequent steps.

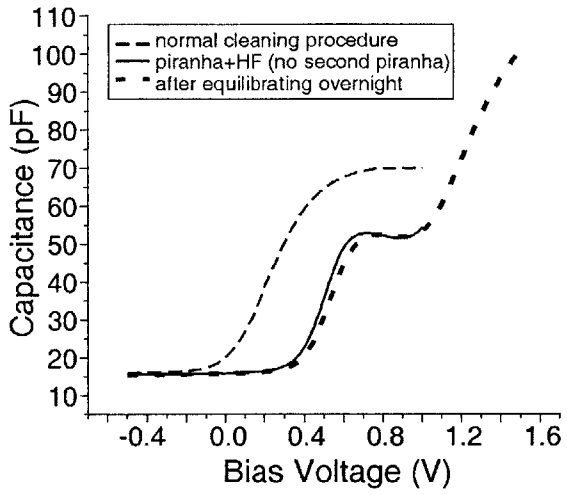

Figure 4-11: CV-HF and drift versus concentration

It is expected that the HF dip and any subsequent native oxide growth would leave the silicon-oxide interface in a different (and unknown) state than results from the thin oxide growth in piranha, and the condition of the silicon oxide interface (fixed charge, traps, roughness, etc) shifts the observed flat-band voltage. The shift along the voltage axis, corresponds to a flat-band voltage shift of +480 mV.

In MOS characterization, a shift in flatband voltage is usually indicative of interfacial charge states at the silicon/silicon oxide interface. The magnitude of fixed interface charge can be extracted from the observed voltage shift as:

$$\Delta V_{\mathrm{FB}} = -\frac{Q_{\mathrm{int}}}{C_{\mathrm{ox}}A} \tag{4.7}$$

It is reasonable to think that a similar effect might cause the observed voltage shift in this case. Assuming the charge to be concentrated at the $\mathrm{Si} - \mathrm{SiO_2}$ interface is a simplification. It is likely that there is some distribution of defects throughout the thin oxide layer. In comparing two MOS structures, independent measurements of the oxide thickness can be made, and the bulk permittivity of oxide can be assumed. Here, however, the dielectric thickness cannot be measured independently, and the condition of the oxide is unclear. Comparing flatband voltages will require a few assumptions. If a nominal capacitance of 2.3×10^{-6} F/cm^2 is assumed, and the charge is assumed to be at the $\mathrm{Si} - \mathrm{SiO_2}$ interface, the effective change in defect density is 6.9×10^{-12}. The direction of the flatband voltage shift corresponds to increased negative charge at the interface.

The shape of the CV characteristic is also significantly altered. The CV characteristic demon-

strates significantly lower accumulation capacitance, nominally indicating a thicker layer, or a more porous oxide with lower permittivity than the original layer. Between $\sim$.75 V and $\sim$1 V, the accumulation capacitance shows a downward slope, indicative of leakage through the oxide. The original sensor surface remains flat through accumulation biases of interest, indicating negligible leakage. The steep rise in capacitance above $\sim$1.0 V indicates breakdown of the insulator layer.

The sensor was then left overnight at a bias voltage of 0.5 V with respect to the gate, to assess the stability of the (non-piranha) oxide. The primary observed effect is that the CV characteristic has shifted along the voltage axis to a lower V_{fb}, with a slight increase in the total difference between the inversion regime capacitance and the accumulation regime capacitance. A bias voltage of 0.5 V on the gate makes the silicon portion of the device act as a the cathode; if anything, we would expect oxidation at this interface. The stability of the CV characteristic suggests that there is some form of native oxide is already present on the surface.

This 'native oxide' CV curve is much lower in accumulation capacitance, and shows a more significant flatband voltage shift than any of the curves that result from variability in the piranha-mediated chemical oxide growth. Because little drift was observed after allowing the 'native oxide' device to equilibrate over night, we can describe it in electrochemical terms as being in a highly oxidized state.[10]

The sensor was subsequently removed from the fluid cell and prepared in piranha. The resulting CV characteristic was similar in shape to the original CV characteristic, although the accumulation capacitance was lower ($\sim$ 60 pF), and the flat-band potential was several millivolts lower than that observed in the first measurement, which had been allowed to equilibrate for several days. The discrepancy bewteen this CV characteristic, and the original CV characteristic was in the range shown in Figure 4-10.

From this investigation, we conclude that a thin oxide grown in piranha differs qualitatively from a native oxide produced after HF cleaning and subsequent rinsing. The piranha-grown oxide shows a higher accumulation regime capacitance, corresponding to either a thinner dielectric, or a denser dielectric. While CV curves from sensors prepared in piranha show significant variation, it seems that the 'native oxide' curve produced from the HF procedure represents a 'lower bound' on the oxide quality. It is worth noting, however, that the variability of dC/dV sensitivity—the slope of the CV curves— is small for the bias points of interest.

[10]This nomenclature is confusing. When we describe oxidation in the microfabrication context, we refer to the growth of an SiO_2 film. In the electrochemical context, we refer to a change in charge state that can be mediated by a number of different mechanisms.

4.3.4 Drift

The operation of EIS sensors is confounded by slow drift processes which limit the sensor resolution at long time scales. The observed drift is a slow shift of the CV curve, independent of change of the electrolyte composition. For EIS systems with moderately thick gate insulators, drifts are characterized by a change in flatband voltage of the sensor: CV curves reported for these devices simply shift along the voltage axis with no other qualtiative changes. The time characteristic of the flatband voltage shift follows a stretched exponential decay. The initial drift rate can be quite high. After several hours of equilibration, the drift will slow, and exhibit a nearly-linear profile.

Figure 4-12 shows equilibrium drift measurements taken in 5 mM phosphate buffer with variable NaCl concentration for the thin-oxide gated sensors used int his work. Drift measurements were made after sensors were equilibrated at least 12 hours. The observed drift was typically in the range of 1-10 mV/hour, which is commensurate with previously drift reported for SiO_2 -gate sensors with thicker gate oxides.[11] Other gate insulators such as silicon nitride ($<$ 1 mV/hr)[10,12] or aluminum oxide (1-10 mV/hour)[10] typically exhibit less drift. As a point of comparison, Jamasb finds the equilibrium drift in MOSFETS to be $\sim$.033 mV/hr.[13]

From the measurements shown in Figure 4-12, it can be seen that the drift rate can be quite low for some measurements. After several hours of equilibration, the drift is nearly linear over the course of a few hours. But using a differential readout with two sensors, it is possible to eliminate drift effects as long as the drift is linear over the time scale of the experiment.

Both positive and negative directions of voltage shift is observed, although positive shifts are small in magnitude. It is likely that these positive drifts represent temperature fluctuations, which are extreme in our laboratory. Other proposed mechanisms imply monotonic drift characteristics. These include electric-field enhanced ion migration in the gate insulator, reduction (injection of electrons) at the insulator under anodic polarization, and slow hydration of the insulator surface. Jamasb and coworkers have done extensive modeling work on the hydration mechanism,[13,14,15]

[11]W.H. Baumann, M. Lehmann, A. Schwinde, R. Ehret, M. Brischwein, and B. Wolf. " Microelectronic sensor system for microphysiological application on living cells." *Sensors and Actuators B* **55** 77 (1999).

[12]D.G. Hafeman, J.W. Parce, and H.M. McConnell. "Light-Addressable Potentiometric Sensor for Biochemical Systems." *Science* **240** 1182 (1988).

[13]S. Jamasb, S. Collins, and R. L. Smith. "A physical model for drift in pH ISFETs." *Sensors and Actuators B* **49** 146 (1998).

[14]S. Jamasb, J.N. Churchill, S.D. Collins, and R.L. Smith. "Accurate Continuous Monitoring Using ISFET-based Biosensors Based on Characterization and Modeling of Drift and Low Frequency Noise." *Proceedings of the 20th Annual International Conference of the IEEE Engineering in Medicine and Biology Society* **20** 2864 (1998).

[15]S. Jamasb, S.D. Collins, and R.L. Smith. "A Physical Model for Threshold voltage Instability in $Si_3N_4-GateH^+$-Sensitive FET's (pH ISFET'S).

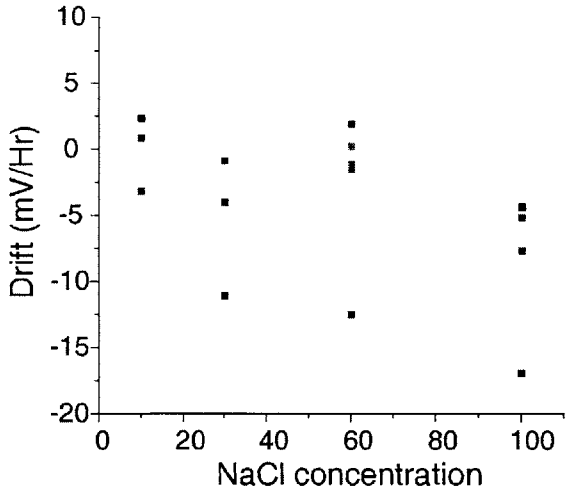

Figure 4-12: Typical drift values measured in buffers of various NaCl concentrations

describing it as a dispersive transport of hydrogen into the insulator. Bousse and coworkers have described hysteretic effects at the insulator-electrolyte interface which affect sensor signals up to a few hours after injection of an analyte.[16] While they discuss these effects as distinct from drift mechanisms, if surface hydration is the drift mechanism, it would additionally create buried titratable sites that would contribute to long time-scale pH response.

In contrast to EIS sensors with thicker oxides, the flatband voltage shift was accompanied by an attenuation of accumulation regime capacitance sensors with thin gate oxides. CV characteristics taken after three successive cleaning and equilibration cycles are shown in Figure 4-13. In each case, the sensor was allowed to equilibrate at least 12 hours before the 'equilibrated' characteristic was measured. While the initial CV curves show very different qualitative characteristics, the equilibrated curves are far more similar in both accumulation regime capacitance and flatband voltage. Typically, the flatband voltage will shift 150 to 400 millivolts higher than before equilibration. The attenuation of the accumulation capacitance observed to be between 5% and 17% . It is interesting to compare these trends to the CV curves observed for a sensor with a natively formed oxide produced after HF cleaning described in the previous section and shown in Figure 4-11. The drift mechanism causes either a thicker oxide to be formed, or the oxide to become more porous—more similar to the natively formed oxide.

The typical observation during experiments is that as the sensor equilibrates at a fixed bias

[16]L. Bousse, D. Hafeman, and N. Tran. "Time-dependence of the Chemical Response of Silicon Nitride Surfaces." *Sensors and Actuators B* **1** 361 (1990).

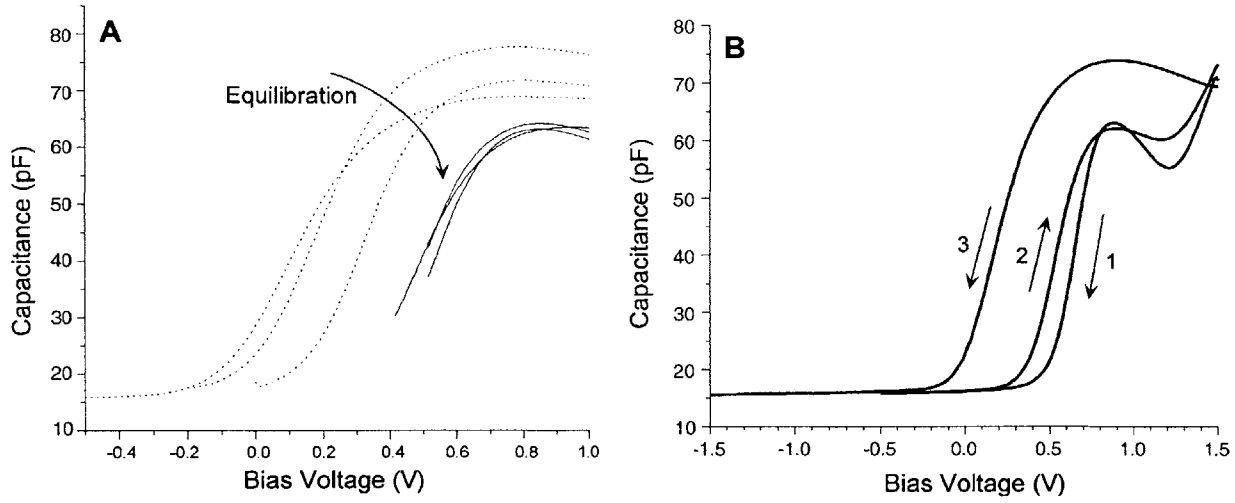

Figure 4-13: CV curves showing initial and equilibrated characteristics.
A) CV curves from several trials showing equilibration characteristics. Dotted line = initial measurement. Solid line = characteristic after 12 hours' equilibration. B) CV characteristics showing reversibility of drift characteristics under negative bias conditions.

point, the V_{FB} will shift to more positive values (surface potential measured at fixed bias point moves to more negative potentials). However, upon moderate bias voltage excursions, driving the sensor into inversion, the CV curve will shift back to more negative V_{FB} values, restarting the drift process. This trend is illustrated in Figure 4-13.B. This demonstrates that the drift mechansim is *reversible*, and can be re-set by applying a large negative gate voltage. Typically, CV curves are measured by sweeping the voltage from inversion to accumulation, to produce a CV characteristic independent of minority carrier generation rate.[17,18] For this measurement, CV curves were taken sweeping first from accumulation to inversion (curve 1), and then from inversion to accumulation (curve 2). This results in a shift to lower V_{FB}, and a change in the accumulation regime behavior. A more extreme negative bias of -1.5 V further shifts both the V_{FB} and the accumulation behavior. At this polarity, a current would cause a reduction of the silicon/oxide structure[19]. A reduction of the surface would account for the higher accumulation regime capacitance. This can be understood in one of two ways. First, the reduction may simply thin the oxide layer. Second, it may produce a denser oxide, possibly expelling ionic charge which may have diffused into the oxide.

The direction of the V_{FB} shift after application of anodic potential at the silicon electrode,

[17]B.J. Gordon. "C-V Plotting: Myths and Methods." *Solid State Technology* **36** 57 (1993).
[18]E. H. Nicollian and J. R. Brews. *MOS (Metal Oxide Semiconductor) Physics and Technology.* Wiley. New York. (1982).
[19]electrochemistry nomenclature describes this as an oxidation current, where it is the *electrolyte* that is oxidized

however, is typically indicative of injection of positive charge into the oxide. It is non-intuitive that reduction at the oxide surface could cause positive charge to be injected into the gate, since reduction implies the *gain of electrons* by the oxide. However, if reduction is thought of as the *loss of protons*, a self-consistent scenario can be described: holes may be injected into the oxide, displacing protons and injecting positive charge into the dielectric.

This hypothesis seems plausible based on the recent observation of anode hole injection in ultrathin silicon dioxide films.[20] The possibility of hole transport in silicon dioxide gate layers has been debated for decades (see references in DiMaria[20] and electron injection current has typically dominated measurements. However, for the anodic bias conditions analogous to applying negative gate voltage to our devices, DiMaria and Stathis observe hole injection while electron injection is blocked. Since the anodic bias conditions re-set the flat-band voltage to lower values, it seems that the drift mechanism is reversible. If the slow hydration is believed to be the mechanism of the drift, it is possible that the reduction of the silicon/oxide structure could involve both injection of holes — electronic charges — from the silicon into the oxide and expulsion of protons — ionic charge — from the oxide to the insulator.

Many commercial EIS sensors rely on nitride gate dielectrics, which are less permeable to ionic charge than oxides, and there may be interest in developing thin-gate-dielectric EIS sensors with nitride gates. However, it is believed that the stretched exponential time-course of drift in nitride insulators corresponds to the saturation of a hydration layer to a thickness of tens of Angstroms.[13] This work suggests that thin nitride layers would become completely hyrdrated, allowing charge transfer through the oxide below. It is unclear whether using thin nitride gates offers significant advantages over thin oxide gates, since nitride layers would have to be several nanometers thick to lower drift values and the dC/dV sensitivity decreases rapidly with even a few nanometers of gate dielectric.

Broadening our scope from the discussion of the flat-band potential shifts in Figure 4-13, the consideration of the entire CV characteristic merits attention. Above bias voltages $\sim$.75 V, the initial CV curve displays a bias-dependent accumulation capacitance. The bias dependence is too dramatic to be accounted for solely as electrolyte-depletion effect; it is instead suggestive of leakage through the gate. The rapid increase in capacitance above $\sim$1.1 V represents the onset of breakdown of the oxide; higher potentials result in direct current through the device. The bias-dependence of

[20]D.J. DiMaria and J.H. Stathis. "Anode hole injection, defect generation,a nd breakdown in ultrathin silicon dioxide films." *Journal of Applied Physics* **89** 5015 (2001).

the accumulation capacitance is ameliorated when the silicon is negatively biased, and the flatband potential has a more negative value. It seems that the equilibrated gate dielectric may be less dense, and more susceptible to breakdown.

4.3.5 Series Resistance

In reality, the complex impedance of our system is not a pure capacitance, and we must be prepared to deal with parasitic elements. It has been shown in Chapter 2 that capacitances arising in the electrolyte portion of the structure are far greater than either the silicon depletion capacitance or the oxide capacitance, and have little effect on the measured capacitance.

In the simplest model, we will consider a resistance in series with the EIS capacitance. Most prominently, series resistances are introduced by (1) contact resistance between the electrolyte and reference electrode in solution, (2) the resistance of the electrolyte volume,(3) the resistance of the highly-doped silicon electrical trace connecting the sensor region at the tip of the cantilever to the aluminum contact on the die, and (4) contact resistance between the silicon trace and the aluminum contact. For simplicity, we will lump these resistances together in a single series resistance R_S. The effect of the series resistance has been noted for both MOS structures[17,18] and EIS structures.[21] Prasad and Lal have found that the electrolyte resistance was a significant source of error in the CV curves for their EIS sensor structures. For the series connection, the admittance is given by:

$$Y_s = \frac{1}{R_s} + j\omega C_{\text{EIS}} \tag{4.8}$$

It is useful to perform a bit of algebra to formulate this equation such that real and imaginary parts are clear:

$$Y_s = \frac{j\omega C_{\text{EIS}} + \omega^2 R_s C_{\text{EIS}}^2}{1 + \omega^2 R_s^2 C_{\text{EIS}}^2} \tag{4.9}$$

taking the magnitude and phase of this expression,we can derive the current output given a sinusoidal voltage input:

$$i(t) = \frac{\omega C_{\text{EIS}} V_{\text{AC}}}{1 + \omega^2 R_s^2 C_{\text{EIS}}^2} \cos\left(\omega t + \arctan\left(\frac{1}{\omega R_s C_{\text{EIS}}}\right)\right) \tag{4.10}$$

We can see then, that the apparent measured capacitance relates to the actual EIS structure capacitance as:

$$\omega C_{\text{measured}} = \frac{\omega C_{\text{EIS}}}{1 + \omega^2 R_s^2 C_{\text{EIS}}^2} \tag{4.11}$$

[21] B. Prasad and R. Lal. "A capacitive immunosensor measurement system with a lock-in amplifier and potentiostatic control by software." *Measurement Science and Technology* **10** 1097 (1999).

It is instructive to examine the limits of this expression. When $\omega^2 R_s^2 C_{\text{EIS}}^2 << 1$, the apparent capacitance converges to the actual EIS capacitance. Note that this is true when the series resistance is small. When the capacitance is small, and at low frequencies, however, the resistance must be quite large to affect the signal.

In the limit where $\omega^2 R_s^2 C_{\text{EIS}}^2 >> 1$ the charging current will converge to $i(t) = \frac{1}{\omega R_s C_{\text{EIS}}} V_{\text{AC}} \cos \omega t$

In Figure 4-14 the frequency response of the EIS sensor is examined to identify series resistance contribution to the apparent measured capacitance. The sensor response is compared to the frequency response of a ceramic capacitor, which shows little deviation from a purely capacitive response. The EIS sensor, however, showed significant series resistance: a series resistance of 320 kΩ provided a good fit to the data. This resistance is unexpectedly high.

Specific contact resistance at the aluminum-silicon interface was measured to be $1.6 \times 10^{-4} \Omega\text{cm}^2$, which is moderate, but for our geometry contributes about 8 ohms. Resistivity of the highly-doped silicon trace was measured by the Van der Pauw method[22] to be 11.3 Ω/square, in moderate agreement with 14 Ω/square predicted by TSUPREM software simulation of the fabrication process. For our geometry, the trace resistance totals $\sim$ 500Ω. It is likely that the large series resistance is contributed by the electrolyte and the electrolyte-reference electrode contact.

In Figure 4-15, the CV characteristic of the sensor is shown at various frequencies. Here, two effects can be seen clearly. First, the series resistance effect is shown for frequencies below $\sim$ 20 kHz. At higher frequencies, the sensor response is affected by the low-pass behavior of the current pre-amp. For the 10^7 gain used in these measurements, the -3 dB point of high-freqency cuttoff of the current pre-amp is 35 kHz. The 50 kHz CV characteristic is clearly diminished by this effect.

In spite of both effects described here—series resistance, and low-pass behavior of the pre-amp—the slope of the CV curves — which is the sensitivity parameter of our system — is affected little by non-idealities.

[22] D.K. Schroder. *Semiconductor material and device characterization.* Wiley. New York (1990).

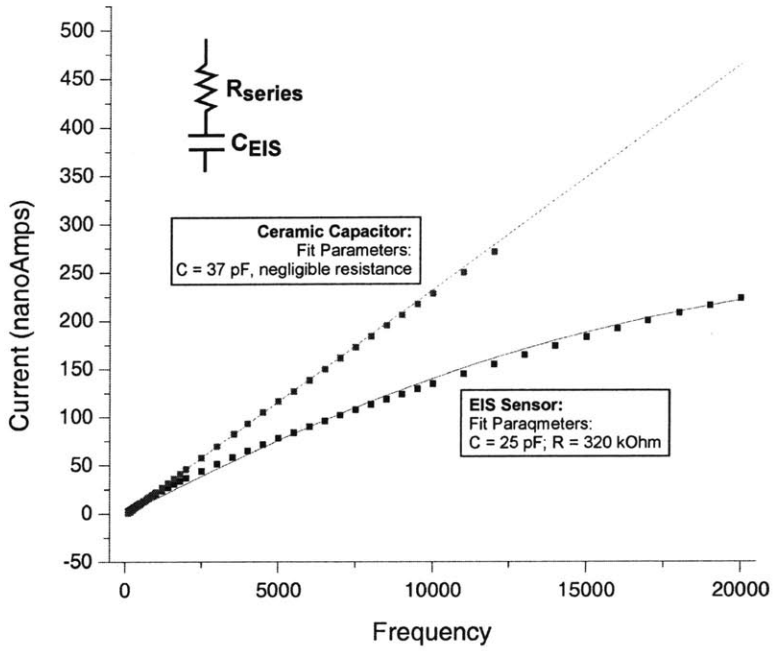

Figure 4-14: Frequency response of EIS sensor and ceramic capacitor.
An AC voltage of 100 mV was applied at frequencies between 100 Hz and 20,000 Hz; a lock-in time constant of 100 ms at 12 db was used. The EIS sensor was biased to the steepest part of its CV curve with a gate voltage of .7 V. This same DC bias voltage was applied to the ceramic capacitor, which was nominally 39 pF ±5

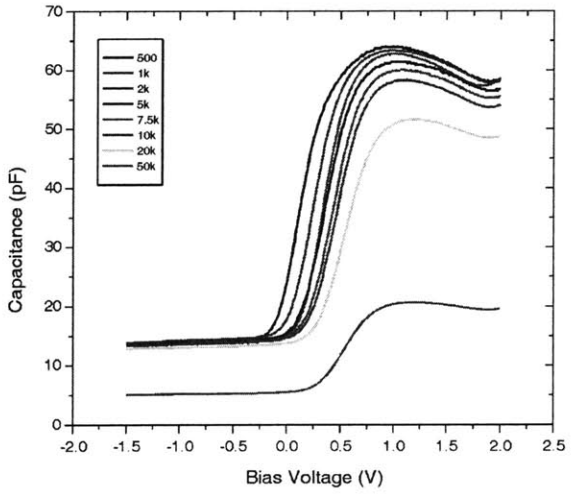

Figure 4-15: Amplitude and frequency of AC charging voltage

Chapter 5

Investigating Ionic and Molecular Charge Interactions

5.1 Introduction

The previous chapter discussed the characterization of the silicon portion of the EIS sensor, the total assembled EIS cell, and the effects of using an extremely thin gate oxide. This chapter continues the characterization of our sensor as we investigate its sensitivity to two systems of ionic charge. First, the sensor response to pH—the reversible titration of the gate oxide—is measured. Second, the sensor response to electrostatic adsorption of highly charged macromolecules is measured. Understanding the sensor response to these systems lays the foundation for work on specific molecular recognition, which will be presented in Chapter 6.

5.2 pH Response

Ion-Sensitive Field-Effect Transistors (ISFETs) have long been used as pH sensors, and several commercial devices based on this technology are available. Until the mid 1980s, the mechanism of pH sensitivity of silicon dioxide insulators was not well understood, and several models were proposed. Diot, Martin, and Clechet disproved the notion that pH sensitivity arose from interaction of hydrogen species with interface states at the Si/SiO2 interface.[1] Instead, they proposed that the ionization and complexation events at the electrolyte-insulator interface that give rise to pH

[1] J.L. Diot, J. Joseph, J.R. Martin, and P. Clechet. "pH dependence of the Si/SiO2 interface state density for EOS Systems." *Joural of Electroanalytical Chemistry* **195** 75 (1985).

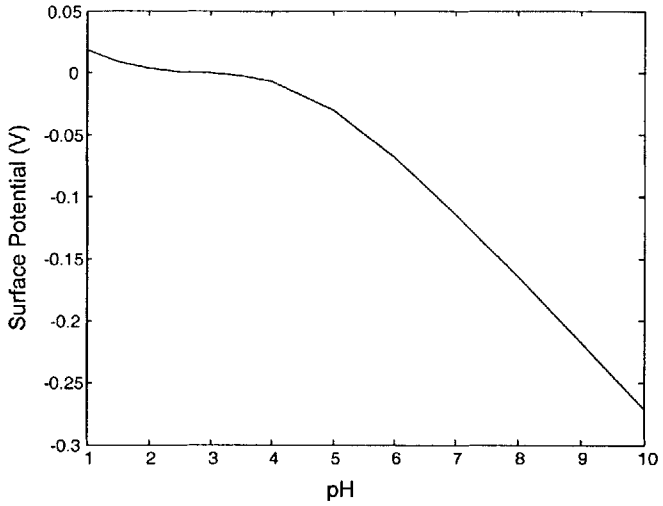

Figure 5-1: Surface potential response to pH for oxide.
Calculated using the site-binding model, described in Chapter 2, with a pH_{pzc} of 3 and $N_s = 5 \times 10^{14}/cm^2$.

sensitivity are described well by the site-binding model reviewed in Chapter 2. The pH response of field-effect sensors is primarily fast and reversible. Field-effect sensors are well-suited to this type of reversible measurement because of their real-time readout. Applications of pH sensing include metabolic studies on large and small numbers of cells.

Boltzmann distribution predicts a maximum pH sensitivity of $2.303\frac{kT}{q}$ V/pH unit, or 60 mV/pH unit, the so-called Nernstian response. The pH response of an oxide surface can be estimated using the site-binding model, as shown in Figure 5-1. The equilibrium constants, total number of surface sites, and pH of zero charge are all parameters that vary according to the oxide surface condition and the environment. In particular, oxide surfaces typically exhibit fewer active surface sites than the model assumes. Various correction factors for this deviation appear in the literature.[2,3,4]

While it is well-known that silicon oxide surfaces demonstrate sub-Nernstian pH response, and surfaces like silicon nitride or aluminum oxide make better pH sensitive surfaces, it is nevertheless instructive to identify the pH sensitivity of the devices. Primarily, it yields insight into the surface condition of the oxide.

[2]L. Bousse, N.F. De Rooij, and P. Bergveld. "Operation of Chemically Sensitive Field-Effect Sensors As a Function of the Insulator-Electrolyte Interface." *IEEE Transactions on Electron Devices* **ED-30** 1263 (1983).

[3]P. Bergveld, R.E.G. van Hal, and J.C.T. Eijkel. "The remarkable similarity between the acid-base properties of ISFETs and proteins and the consequences for the design of ISFET biosensors." *Biosensors and Bioelectronics* **10** 405 (1995).

[4]R.E.G. van Hal, J.C.T. Eijkel, and P. Bergveld. "A general model to describe the electrostatic potential at electrolyte oxide interfaces." *Advances in Colloid and Interface Science* **69** 31 (1996).

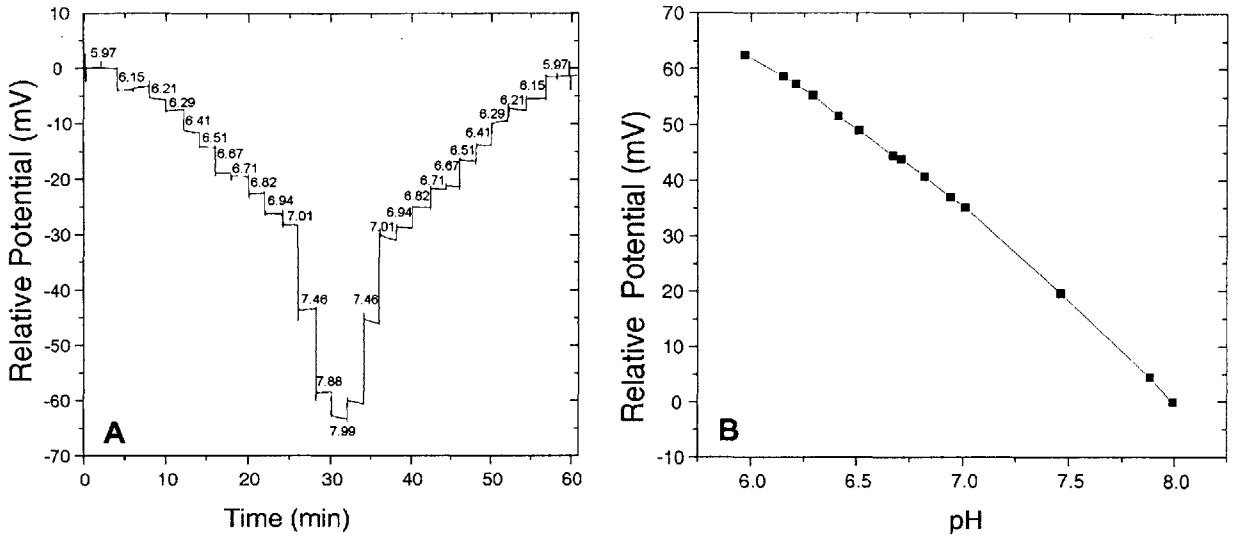

Figure 5-2: Sensor response to pH

A: At 5 minute intervals, phosphate buffer at various pH values as injected into the fluid cell. B: Relative surface potential versus pH value

The pH response of the sensor was tested in the biologically relevant range of pH 6 to pH 8 in phosphate buffer. 100 mM monobasic and dibasic phosphate solutions were prepared with 10 mM NaCl, and then mixed in varying proportions to produce an array of pH values at the same concentration. The sensor was equilibrated in the fluid chamber for several hours in a pH 6 solution. At five minute intervals, buffers of different pH values were injected in succession, as shown in Figure 5-2A. The equilibrium surface potential after each injection is recorded in Figure 5-2B for each of the pH values used. The surface potential response was calibrated by applying a 2.5 mV bias signal at the current pre-amplifier, and the data are scaled to this signal.

A non-linear pH dependence is observed in this range, with an approximate slope of ~31 mV/pH. The non-linearity and slope is affected by several factors: the pH of zero charge, pH_{pzc}, the density of surface sites, N_s, and equilibrium constants for surface ionization and complexation. The pH of zero charge, which is defined as the pH value at which there is no net surface charge, and therefore no space charge region in the electrolyte, has been reported to be between pH 1.5 and pH 3.7 for silicon oxide (see Bousse[4] and references therein). The number of surface sites has a maximum value of 5×10^{14}, but typically, only some fraction of the sites are active. From the pH response demonstrated here, a relatively high pH_{pzc}, as well as a low density of surface sites is evident. However, precise values for these factors cannot be extracted from the data independently of each

other and the surface equilibrium rate constants.

For an RMS noise value of $\sim$10 μV, a pH resolution of $\sim 3 \times 10^{-4}$ pH units is achievable with this sensor. This is commensurate with the pH resolution demonstrated by the LAPS, 5 to 10×10^{-4} pH units.[5]

5.3 Electrostatic adsorption of polyionic multilayers

While the previous section described the sensors' response to a rapidly reversible charge system, this section analyzes the response to effectively irreversible adsorption of highly-charged molecules. The molecules used in this study inhabit significantly greater volume than the ionic charge responsible for pH response. This section develops understanding of charge effects near the sensor surface and investigates the relative contributions of surface potential effects versus interfacial impedance effects on the measurement.

Bergveld has proposed[6] an EIS measurement technique that would analyze both the surface potential change and the increased interfacial capacitance induced by binding of a charged molecular layer. The idea was to analyze the entire CV curve to record the combination of effects that may occur upon the binding of charged molecules in order to enable more comprehensive measurements.

In the handful of work that addresses this proposal, measurements have been made which were sensitive to impedance or surface potential, but not both. Impedance spectroscopy records the interfacial impedance across a frequency spectrum. Typically devices used for this are metal electrodes or extremely highly doped silicon electrodes, passivated with oxide. Silicon-based devices for impedance spectroscopy are usually operated in accumulation where the silicon depletion capacitance is negligibly high and will not obscure interfacial capacitances. The silicon substrate is typically highly doped to minimize surface potential resolution in all regimes of operation. In contrast, EIS capacitors that are used to measure surface potential are typically biased in depletion or weak accumulation regimes where the dC/dV sensitivity is highest, and are typically lightly doped to maximize this sensitivity (see discussion of sensitivity in Chapter 2).

Bataillard and coworkers demonstrate the direct detection of immunospecies by monitoring accumulation capacitance with an EIS structure with 70 nm of gate oxide and unspecified dop-

[5]H.M. McConnell, J.C. Owicki, J.W. Parce, D. L. Miller, G.T. Baxter, H.G. Wada, and S. Pitchford. "The Cytosensor Microphysiometer: Biological Application of Siliocn Technology" *Science* **257** 1906 (1992).

[6]P. Bergveld. "A Critical Evaluation of Direct Electrical Protein Detection Methods." *Biosensors and Bioelectronics* **6** 55 (1991).

ing level.[7] They found significant decrease in accumulation capacitance upon grafting surface functionalization layers, but no significant flatband potential shift of their curves. From the accumulation capacitance, the layer thicknesses of immobilized molecules were deduced. Relatively large molecules were studied by this technique; typical layers were several nanometers thick.

Although potentiometric sensors and interfacial impedance sensors require different fabrication parameters for optimization, Bergveld's proposal brings up a possible ambiguity that could confuse the interpretation of measurements made at a fixed bias point. Interpreting a signal purely as a surface potential shifting the CV curve along the voltage axis would lead to erroneous conclusions if interfacial capacitances were in fact shifting the CV curve along the capacitance axis.

We describe three sets of data which enable insight into the relative contributions of series impedance modulation and surface potential shifts. In the first set, successive layers of highly positively charged Poly-L-Lysine (PLL) and highly negatively charged DNA are electrostatically adsorbed onto the surface. Ellipsometric measurements of grafted layer thickness are compared with surface potential signals observed during successive adsorption events. In the second set of experiments, PLL and Poly-L-Glutamic acid (PLG) multilayers are formed, and CV measurements are made after each addition so that the entire capacitance characteristic can be examined. In the last set, we examine specific binding between biotin and avidin, monitoring fixed-bias-point measurements taken in both accumulation and depletion regimes.

5.3.1 PLL and DNA multilayers

To demonstrate that the field-effect devices used in this work are sensitive specifically to the charge of adsorbed molecular layers as opposed to the thickness of the layers,[8] we monitored the growth of polyelectrolyte multilayers consisting of positively charged PLL and negatively charged oligonucleotides on the sensor surface, shown in Figure 5-3. Such layers bind to each other primarily by electrostatic interactions and are known to overcompensate for the surface charge of the previously adsorbed layer, which leads to a linear growth in multilayer thickness as positively and negatively charged molecules are successively applied to the surface.[9] Using ellipsometry, we determined the incremental thickness increase of PLL-oligonucleotide multilayers to be ~0.4 nm per layer. In contrast, the field-effect sensor showed an alternating response over five successive cycles of PLL and

[7]P. Bataillard, F. Gardies, N. Jaffrezic-Renault, C. Martelet, B. Colin, and B. Mandrand. "Direct Detection of Immunospecies by Capacitance Measurements." *Analytical Chemistry* **60** 2374 (1988).

[8]C. Berggren, B. Bjarnason, and G Johansson. "Capacitive Biosensors." *Electroanalysis* **13** 173 (2001).

[9]G. Decher. "Fuzzy Nanoassemblies: Toward layerer polymeric multicomposites." *Science* **277** 1232 (1997).

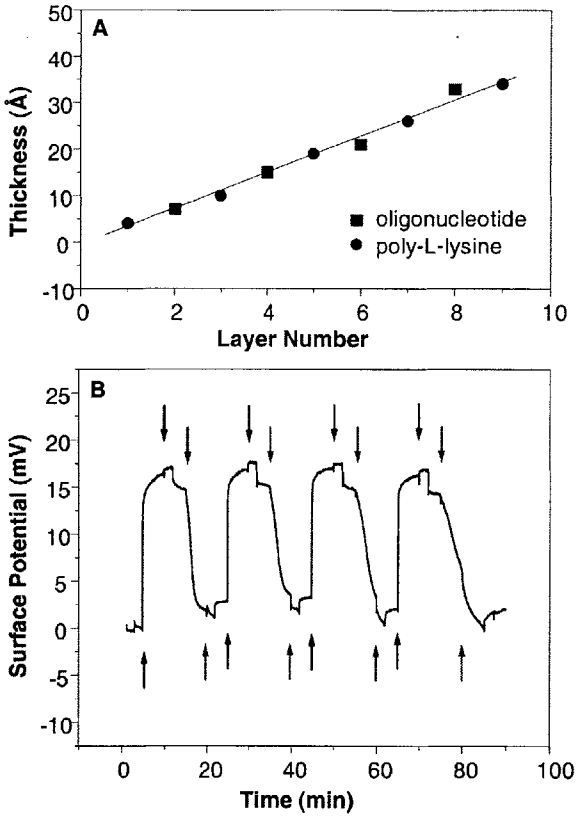

Figure 5-3: PLL and DNA multilayers.
Each polyelectrolyte solution was injected twice and followed by an injection of buffer before the next layer was adsorbed. Dark arrows indicate PLL injection, and light arrows indicate oligonucleotide injections. Ellipsometry: Experiments were done on 1-cm2 pieces of silicon that were prepared identically to the sensor surfaces. The incubation time was 15 minutes followed by 1 minute of equilibration in buffer. Ellipsometry measurements were done in air with a discrete wavelength ellipsometer (Sentech, Berlin). Buffer used was 5 mM sodium phosphate with 10 mM NaCl at pH 7.

DNA adsorption, with an increase of ~16 mV after the addition of PLL and a subsequent decrease of 14 mV after the addition of oligonucleotides, even though the total thickness grew. Thus, our device measures net charge rather than layer thickness.

5.3.2 PLL-PLG multilayers

Further polyelectrolyte adsorption measurements were made by monitoring the accumulation of PLL/PLG multilayers. Sensors were equilibrated in buffer solution over night. Two types of measurements were made: 1) capacitance vs. time at fixed bias voltage, as in the previous section; 2) CV curves after each layer addition to measure effects in all regimes of operation.

For fixed bias point measurements, sensors were biased such that they were in the depletion

regime of operation, at a point on the CV curve of maximal slope. Each injection was a 900 μL aliquot (fluid cell size is $\sim$500 μL). At least 10 minutes was allowed to elapse after each polyelectrolyte addition, and then buffer was injected twice at $\sim$5 minute intervals. An edited time-course of the experiment is shown in Figure 5-4A. It should be noted that over the course of the experiment ($\sim$6 hours) the signal drifted several mV, a feature that is more evident in the CV measurements. Since the silicon dioxide is typically negatively charged in solution, positively charged PLL is injected as the first layer, followed by PLG, and so on in alternating layers. The total absolute change in surface potential is plotted for each layer in Figure 5-4B. The first PLL layer shows a small surface potential step compared to subsequent layers since it is binding to the gate oxide, rather than to a layer of PLG. Subsequent injections of PLL to exposed PLG surfaces show a much greater surface potential step, since the PLG layer has a greater charge density than the oxide layer. It is known that on binding to a surface of relatively low charge density, a polyelectrolyte layer will expose a greater density of sites to subsequent layers, effectively increasing the surface functionality (see Decher[9] and references therein). Over many successive trials, we have noticed variation in the total potential step observed upon adsorption of the initial PLL layer. This is likely due to the variability of surface charge density primarily resulting in variation of cleaning conditions, as discussed in Chapter 4.

Subsequent adsorption of PLL/PLG results in 20-25 mV signal. Figure 5-5 shows the overlayed adsorption profiles for PLL layers (A) and PLG layers (B). In general, a slower response was observed for adsorption of the PLG layers than for the PLL layers. The negatively-charged PLG may be repelled by the net negative charge of the oxide surface, in spite of intermediate PLL layers. There is a clear trend of decreasing slope — increasing adsorption time with additional layers for both the PLL and PLG. It is unclear whether this is caused by a decrease in the rate of adsorption, or whether this trend is a result of slow annealing of the entire multilayer complex.

For a 10 mM mono-monovalent electrolyte, a Debye length of $\sim$3 nm would be expected (This is an approximation, based on the NaCl concentration. In fact, the ionic strength of the solution is higher, and a charge screening length less than 3 nm is predicted.). From ellipsometry measurements, the total thickness of the multilayer complex is expected to be $\sim$5 nm. If the layer coverage were sparse, we would expect the surface potential response to be screened after a few layers, resulting in a decrease in surface potential response with each additional layer. In fact, we observe that the total change in surface potential for each adsorbed layer *increases* slightly. This observation agrees well with the over-compensation of charge noted by other authors for adsorp-

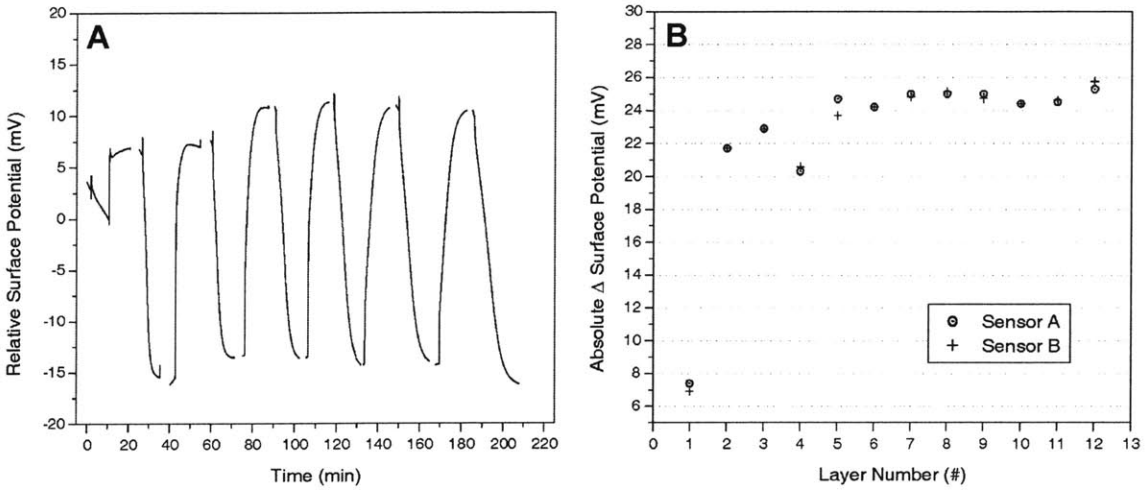

Figure 5-4: PLL-PLG adsorption timecourse

A: 1 mL aliquots of 50 mM PLL and PLG were injected in succession starting with PLL at t=10 minutes. B: Absolute value of change in potential measured after adsorption of each layer. Surface potential designations are relative to an arbitrary origin. Curves have been offset, and linear drift has been compensated. 50 nM concentrations of PLG and PLL in 5.3 mM phosphate buffer, 10.6 mM NaCl, pH 6.97 ± .05. 5 kHz, 40 mV_{pp} AC.

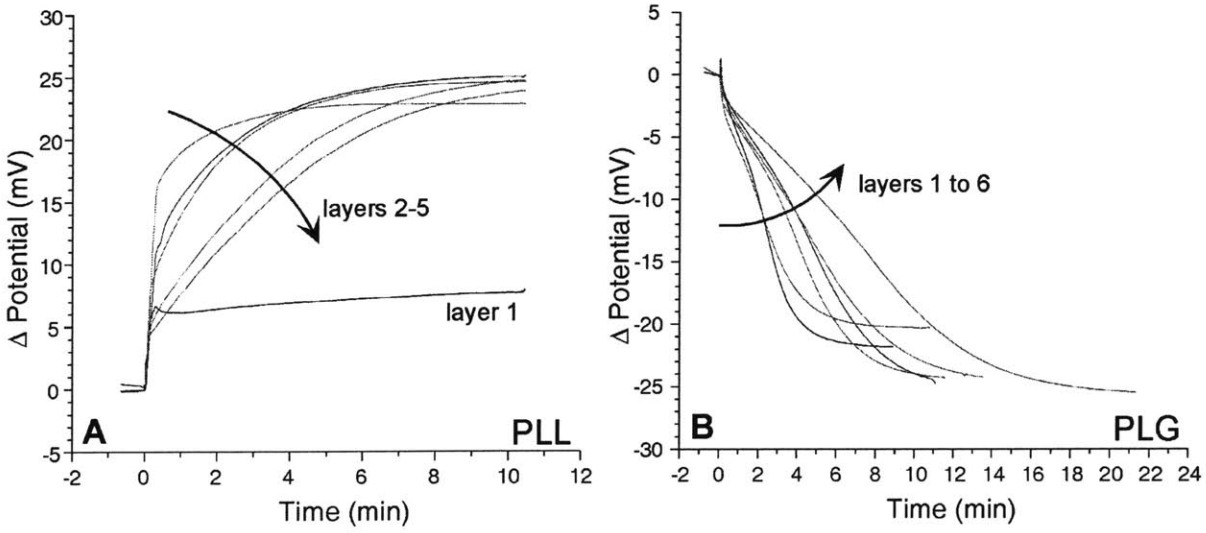

Figure 5-5: PLL-PLG adsorption timecourses

A: Overlayed surface potential response from PLL layers. B: Overlayed surface potential responses for PLG layers.

tion of polyelectrolyte multilayers.[9] Since the surface potential response is not attenuated as the multilayer thickness grows, it seems likely that the molecules are quite densely packed, with a pore size smaller than the Debye length, such that ionic charge is excluded from the matrix.

CV curves were measured after each layer addition. All curves are overlayed in Figure 5-6A. For clarity, the CV region of greatest slope is magnified in Figure 5-6B. The CV curve shifts left for first PLL addition, indicating a more positive surface potential. The CV curve shifts much farther to right for PLG addition. Subsequent layer additions continue this pattern. CV curve trends are more clearly visualized by looking at the capacitance values at certain bias values for each curve. Figure 5-6C shows this for biases of 1 V, .95 V, .65 V, and .6 V. In the depletion regime, a clear zig-zag is observed, overlayed with a drift of about 1.5 mV per hour. The long-term drift of the sensor is to higher V_{FB} values (CV curve shifts to the right).

The accumulation regime variation is much smaller, and is shown by itself in Figure 5-6D. The capacitance rises steeply after the first two injections, and then levels off, with a slight upward trend. This is a non-intuitive result. If the surface layers could be represented simply as an additional series capacitance, the accumulation capacitance would be expected to *decrease* linearly with the thickness of the total multilayer complex, as has been observed for large molecules in the work of Bataillard et al.[7] From previous ellipsometric measurements, we know each PLL layer to be approximately 4 Å thick, which is significantly thinner than layers measured in the Bataillard work, which may be why the impedance signal is less significant, even when the sensor is biased in accumulation.

Delving into an accurate interpretation that could account for the apparent increase in accumulation capacitance requires detailed consideration of the new surface equilibrium. Referring to the site binding model presented in Chapter 2, it can be seen that this model would have to be expanded by including the the competition between the polyelectrolyte molecules and buffer ions to satisfy the charge and potential equilibrium on the surface. The three-dimensional charge configuration near the surface is significantly more complex than the simple two-dimensional charge layer model that was considered in Chapter 2. The interface can no longer be thought of simply as planes of charge, but the volume and distribution of molecules and screening ions. The exact conformation of molecules within the structure cannot be known, but it is likely that the multilayer complex forms a matrix on the surface. The interaction of small ions within this matrix and at the surface plane of the matrix will necessarily alter the interfacial impedance between the gate oxide and the electrolyte bulk. As we have seen in the modeling work in Chapter 2, increasing the

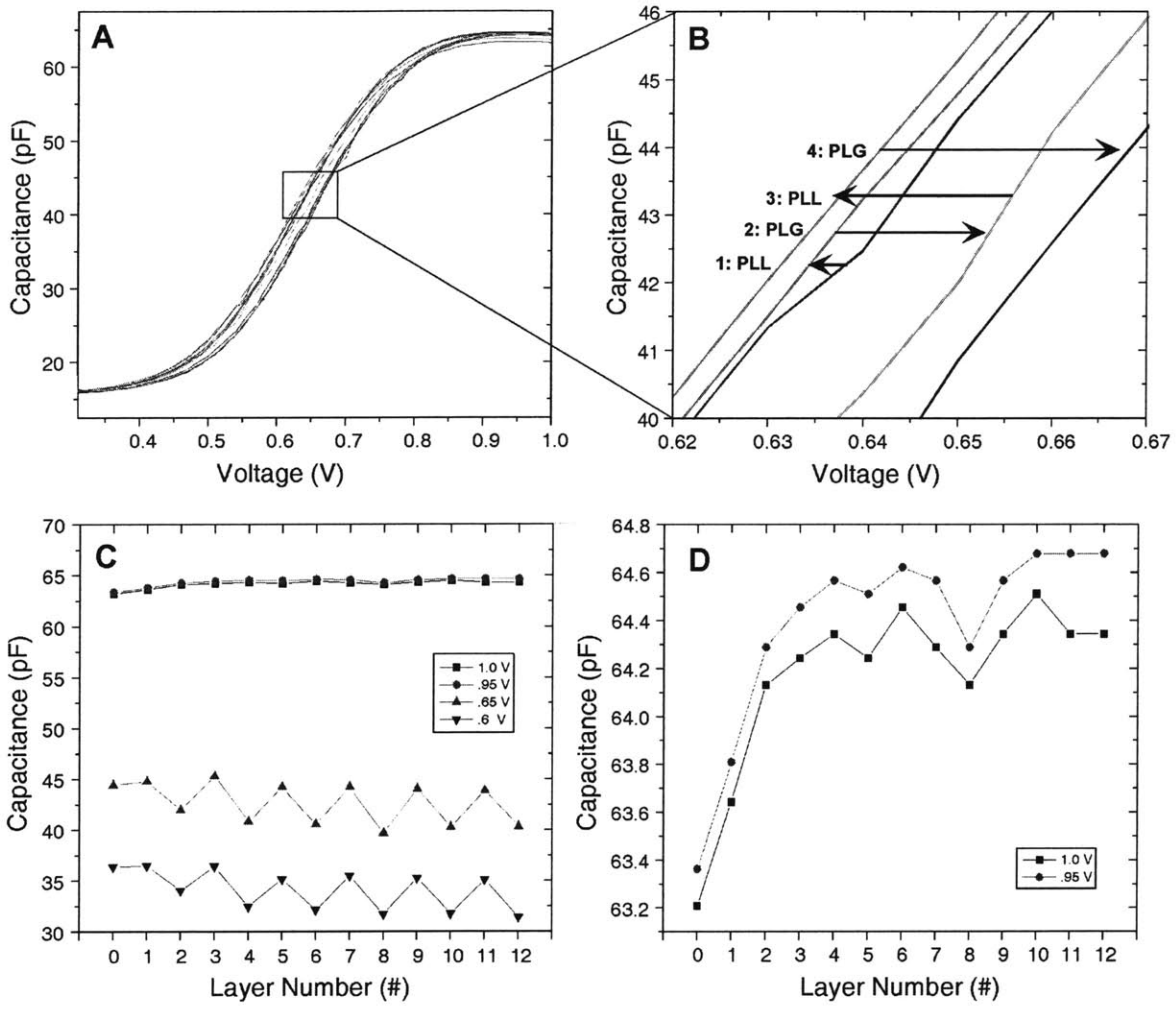

Figure 5-6: PLL-PLG adsorption CV curves:
A and B: CV curves measured after the adsorption of each layer of PLL or PLG. A 10 ms time constant was used on the lock-in. Data was taken at 10 mV steps, waiting 100 mS between each step. C: Accumulation and depletion regime capacitnace values at indicated bias potentials for each adsorbed layer. D: Accumulation regime capacitance values at indicated bias voltages.

capacitance of the screening layer increases the total accumulation regime capacitance.

The primary conclusion to draw from this investigation is that in the depletion regime, any molecular layer impedance caused by a total of a few nanometers of polyelectrolyte does not significantly affect the signal; the primary response is to surface potential for two main reasons. First, the silicon depletion capacitance is the dominant capacitance, far less than any series capacitance contribution of molecular layers. Secondly, for this system, the accumulation signal is much smaller than the depletion regime signal. In the limit of small, highly-charged molecules, the capacitance of the sensor is observed to be primarily dependent on surface potential, with little effect from interfacial capacitance.

5.3.3 Direct Accumulation Regime Measurements: Biotin-Avidin binding

Interfacial impedance measurements have proven useful by other researchers.[7,10] It is safe to conclude from the work presented by others that many systems of interests contribute a large impedance signal, but a very small surface potential signal. The ability to make sensitive surface potential measurements coupled with sensitive impedance measurements provides additional information about various systems.

However, measuring the entire CV characteristic has trade-offs. One drawback is a matter of dynamic range. By measuring at a fixed bias point, we can focus in on very small flatband voltage shifts by increasing the gain of the readout electronics. When entire CV curves are recorded, a greater range of capacitances must be measured. Since the readout system necessarily has resolution limits (digital resolution of the lock-in amplifier, digital resolution of Labview), these measurements are far less precise. The second issue is one of time resolution. Measuring the entire CV characteristic is bounded by the frequency of measurement and the settling time of the lock-in amplifier. The precision with which the CV characteristic can be measured is directly proportional to the time required to acquire the measurement. For our operating parameters, doping levels, frequency, excitation, etc. we make a much more sensitive measurement of surface potential than interfacial impedance, and we are able to achieve a greater time-resolution.

The biotin-avidin system forms a high-affinity complex that has been well-characterized. This system was used as a prototype system to interrogate the accumulation capacitance response of the sensors. Because of the dynamic range issues associated with making measurements of the

[10]E. Souteyrand, J.R. Martin, and C. Martelet. "Direct detection of biomolecules by electrochemical impedance measurements." *Sensors and Actuators B* **20** 63 (1994).

entire CV characteristic, measurements were made at fixed bias points. One of the two sensors was biased in the depletion regime where the sensor is normally operated, and the second was biased in accumulation. Both sensors were amplified to with the same gain. Both sensors were functionalized with biotinylated-BSA by incubating the surface with 1 mg/ml concentration of b-BSA in phosphate buffer. Two buffer solutions were prepared with 5 mM phosphate buffer (pH 6) and 10 mM or 100 mM additional NaCl

Sensors were equilibrated in buffer solution over night and calibrated for surface potential response. Several one-milliliter aliquots were injected at 5 minute intervals, and 0.05 mg/ml BSA was injected to passivate the walls of the fluid chamber in order to minimize nonspecific binding and concentration depletion of the target avidin. A 1-ml aliquot of .05 mg/ml avidin was injected and the surface potential was recorded. This procedure was repeated for both 100 mM and 10 mM NaCl concentrations, as shown in Figure 5-7A and B, respectively. The surface potential response shows a clear dependency on the concentration of the buffer; the effect of greater charge screening of the surface potential response is clearly demonstrated for the higher buffer concentration, as will be discussed in greater detail in Chapter 6. A capacitance shift of .58 pF is observed at 100 mM NaCl and a shift of 3.07 pF is observed for 10 mM NaCl. The capacitance response in accumulation is much weaker: -.04 pF at 100 mM NaCl, and -.01 mM at 10 mM NaCl. The relatively small capacitance response in accumulation indicates that the sensor response is dominated by surface potential effects, which modulate the silicon capacitance, rather than series capacitance of molecular layers at the electrolyte-insulator interface.

The technique of measuring both surface potential response and interfacial impedance may prove insightful for detection systems with large molecules with little charge. The combination of effects may provide a fingerprint of binding events where either measurement alone may be inconclusive. For the systems investigated in the remainder of this thesis, however, interfacial impedance contributes little to the measurand, enabling a straight-forward interpretation of data.

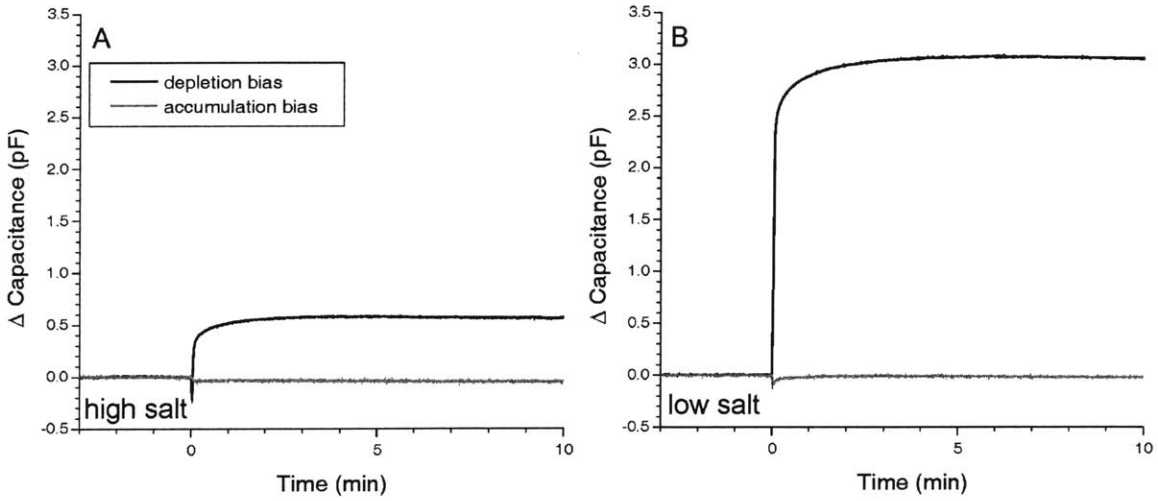

Figure 5-7: Biotin-Avidin binding response in accumulation and depletion regimes. At t=0, 1 mL of avidin at 760 nM is injected into the fluid cell. Sensors have been functionalzied with biotinylated-BSA. A)In 5 mM phosphate buffer + 100 mM NaCl. B)In 5 mM phosphate buffer + 10 mM NaCl.

Chapter 6

Molecular Recognition Experiments

As discussed in the first chapter, work toward field-effect detection of specific biomolecular interactions faces significant challenges. The simplest formulation of the argument against such work cites the seemingly insurmountable nuisance of charge screening in electrolyte solution, which can greatly neutralize net charge on target biomolecules. However, the surface potential resolution reported for many EIS sensors is on the order of 1-10 millivolts. This resolution is right at the boundary of surface potential responses predicted by Meixner and Koch's modeling for protein interactions,[1] so it is not surprising that label-free molecular detection could not be demonstrated with such devices. The fact that the LAPS showed an RMS noise level level of $\sim$30 μV suggests that high resolution measurement may not be the only key component to successful assay development. We approach the problem of specific biomolecular detection by combining the extremely high surface potential resolution achieved by using a thin oxide gate with a differential readout method and electrostatically bound surface chemistry. The work described below draws on the insight developed in previous chapters to demonstrate label free nucleic acids detection, and investigate aspects of charge screening through the model system of biotin-avidin.

6.1 Nucleic Acids Hybridization

The demonstration of direct field-effect detection of DNA hybridization is motivated within two distinct contexts.

First, nucleic acids are a choice model system for interrogating the parameter space for field-

[1] L.K. Meixner and S. Koch. "Simulation of ISFET operation based on the site binding model." *Sensors and Actuators B* **6** 315 (1992).

effect sensing: hybridization of complementary strands is highly specific; DNA is highly charged, and has a uniform charge distribution—each base has a single excess negative charge associated with it along the sugar-phosphate backbone; oligomers of various lengths (i.e. charge per binding event) can easily be produced; functionalization protocols are well established; and finally, DNA binding kinetics are well understood.

Second, field-effect sensors may prove useful for diagnostic application. In particular, such sensors would be well-suited for rapid, point-of-care measurements, particularly where fluorescence methods would be too time-consuming, or where the relevant equipment could not be readily available (e.g. environmental sensing, on-site health care). Such sensors may prove applicable within highly-integrated analytical systems where analyte handling can be optimized.

Although label-dependent methods used most routinely achieve the highest sensitivities,[2,3,4] eliminating the labeling steps has the advantage of simplifying the readout and increasing the speed and ease of nucleic acid assays, which is especially desirable for characterizing infectious agents, scoring sequence polymorphisms and genotypes, and measuring mRNA levels during expression profiling. The development of label-independent methods that can monitor hybridization in real-time is still in its infancy.[5,6,7,8] Souteyrand and coworkers report in 1997 the first demonstration of direct detection of DNA hybridization by silicon field-effect,[9] although their methods require *ex situ* hybridization, and real-time, room temperature measurements have proven difficult.[10]

---

[2]A. Castro and J.G.K. Williams. "Single-molecule detection of specific nucleic acid sequences in unamplified genomic DNA." *Analytical Chemistry* **69** 3915 (1997).

[3]W. Budach, A.P. Abel, A.E. Bruno, and D. Neuschafer. "Planar waveguides as high performance sensing platforms for fluorescence-based multiplexed oligonucleotide hybridization assays." *Analytical Chemistry* **71** 3347 (1999).

[4]T.A. Taton, C.A, Mirkin, and R.L. Letsinger. "Scanometric DNA array detection with nanoparticle probes." *Science* **289** 1757 (2000).

[5]S. Howorka, S. Cheley, and H. Bayley. "Sequence-specific detection of individual DNA strands using engineered nanopores." *Nature Biotechnology* **19** 636 (2001).

[6]J. Fritz, M.K. Baller, H.P. Lang, H. Rothuizen, P. Vettiger, E. Meyer, H.-J. Güntherodt, C. Gerber, J.K. Gimzewski. "Translating biomolecular recognition into nanomechanics." *Science* **288** 316 (2000).

[7]Y. Okahata, M. Kawase, K. Niikura, F. Ohtake, H. Furusawa, and Y. Ebara. "Kinetic Measurements of DNA Hybridization on an Oligonucleotide-Immobilized 27-MHz Quartz Crystal Microbalance," *Analytical Chemistry* **70** 1288 (1998).

[8]B.P. Nelson, T.E. Grimsrud, M.R. Liles, R. M. Goodman, and R. M. Corn. "Surface Plasmon Resonance Imaging Measurements of DNA and RNA Hybridization Adsorption onto DNA Microarrays." *Analytical Chemistry* **73** 1 (2001).

[9]E. Souteyrand, J. P. Cloarec, J. R. Martin, I. Lawrence, S. Mikkelsen, and M. F. Lawrence. "Direct Detection of the Hybridization of Synthetic Homo-Oligomer DNA Sequences by Field-Effect." *Journal of Physical Chemistry B* **101** 2980 (1997).

[10]J.P. Cloarec, N. Deligianis, J.W. Martin, I. Lawrence, E. Souteyrand, C. Polychronakos, and M.F. Lawrence. "Immobilization of homo-oligonucleotide probe layers onto Si/SiO2 substrates: characterization by electrochemical impedance measurements and radiolabeling." *Biosensors and Biolelectronics* **17** 405 (2002).

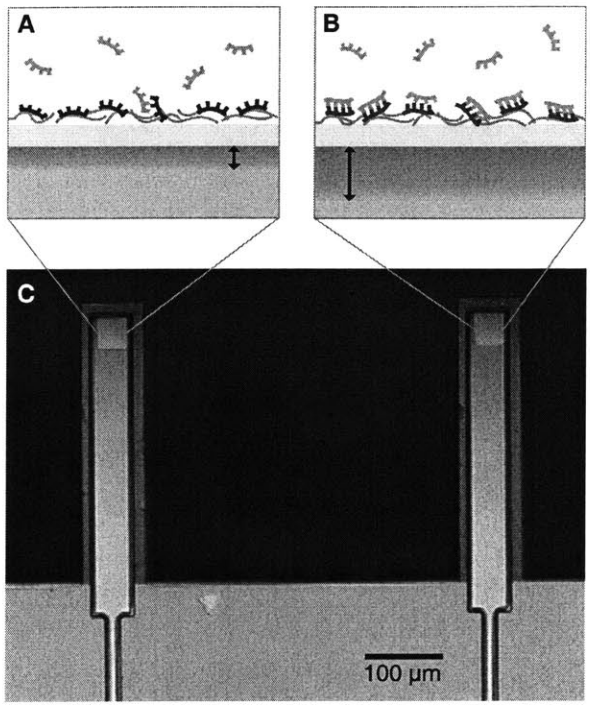

Figure 6-1: Functionalization schematic

a) and b) EIS interface of an n-type sensor. Probe DNA is bound electrostatically to a layer of PLL on the surface. a) Binding of negatively charged target DNA to its complementary probe on the sensor surface modulates the silicon space-charge region. b) No binding occurs between target DNA and non-complementary probe DNA. c) Optical micrograph of sensor.

6.1.1 Results and Discussion

To explore the utility of our field-effect sensor for detection DNA in solution, two sensors were first functionalized with a PLL layer. Next, the sensing area of one sensor was functionalized with the 12-mer oligonucleotide A (sensor 1), and the adjacent sensor was functionalized with the unrelated 12-mer oligonucleotide B (sensor 2).[11] Distinct functionalization, shown schematically in Figure 6-1, enables a differential measurement to be made by comparing the responses of the two sensors. The sensors were then mounted in a fluid cell. Solutions containing various target DNA oligonucleotides were injected in succession, and the surface potential of the sensors was measured. The addition of control solutions such as buffer or oligonucleotide B generated similar signals from both sensors (Figure 6-2A). These signals arose because the surface potential is sensitive to thermal fluctuations, drifts, nonspecific binding, and changes in electrolyte composition. However, because these unwanted signals are similar for both sensors, they can be eliminated by taking the differential response from the two sensors (sensor 1 - sensor 2). A similar differential approach has been adopted by fabricating ISFET structures in a differential pair.[12]

When oligonucleotide cA, complementary to A, was injected, the surface potentials of sensor 1 and sensor 2 diverged. The sensors showed a differential response of -3 mV for oligonucleotide cA and of +3 mV for the subsequent addition of cB Figure 6-2B. These observations demonstrate that a differential field-effect sensor configuration is able to measure the sequence-specific formation of $A - cA$ and $B - cB$ hybrids. As shown in Figure 6-2B, the drift of the differential measurement can be eliminated when sensors are equilibrated and the drift is linear over the time scale of the measurement.

We observed that sensors can be re-used more than 10 times by regenerating their surface with a piranha-hydrofluoric acid-piranha cleaning. After a new round of functionalization with PLL and oligonucleotides, the difference in signal amplitude between the original and regenerated surfaces was 10-20% for hybridizing oligonucleotides at a concentration of 80 nM.

[11] After cleaning with piranha solution (3:1 30% H2O2 in H2O:H2SO4), etching in hydrofluoric acid for 10 s (BOE, 7:1), and chemically growing oxide for 1 min in piranha solution, the sensors were equilibrated in buffer (5 mM sodium phosphate, pH7.0/10 mM NaCl), functionalized with 0.2 mg/mL Poly-L-Lysine (MW 16,000-22,100, Sigma) inside the fluid cell for 15-60 minutes and then incubated individually with 15 μl of 4-40 μM probe oligonucleotides for 15-60 minutes before being place back in the fluid cell. The cantilever design enables functionalization of individual sensors in distinct micropipettes. Each sensor is functionalized with a distinct oligomer sequence. Probe 12-mer oligonucleotide sequences were A=CTATGTCAGCAC, Am = CTATGTAAGCAC, B=AGGTCTAGTGCA, and C=CCTTCTTGGAGAA, and their corresponding compleentary target DNA sequences were cA, cAm, and cB (HPLC-purified, Synthegen, Houston). Hybridization was carried out at room temperature.

[12] H-S. Wong and M.H. White. "A CMOS-Integrated 'ISFET-Operational Amplifier' Chemical SEnsor Employing Differential Sensing." *IEEE Transactions on Electron Devices* **36** 479 (1989).

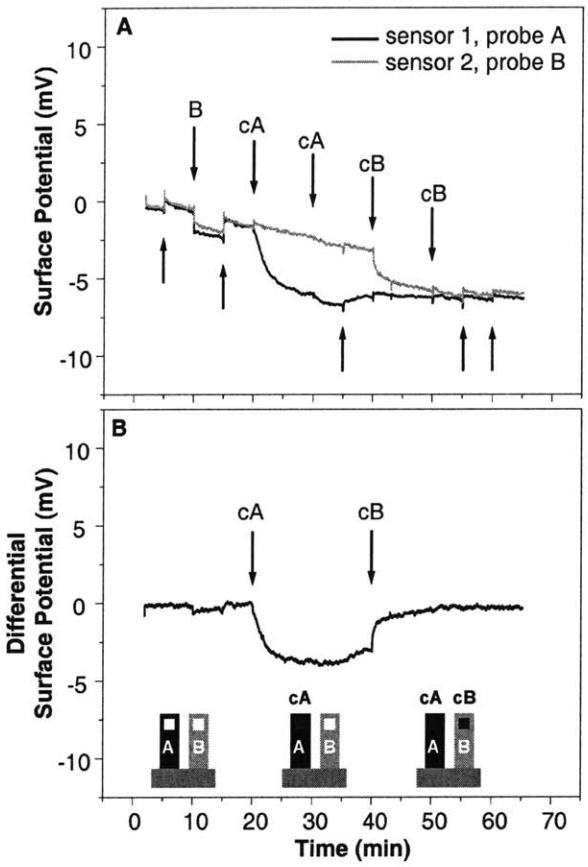

Figure 6-2: Field-effect detection of DNA hybridization

A) Surface potential response from sensor 1 (dark) functionalized with probe oligonucleotide A and sensor 2 (light) functionalized with probe oligonucleotide B during a hybridization experiment. Downward arrows indicate injections of oligonucleotides, and upward arrows indicate injections of buffer into the fluid cell. B) Differential signal obtained by subtracting the two sensor signals shown in (A). The order of injections was: buffer, B (80 nM), buffer, cA (80 nM), cA (200nM), buffer, cB (80 nM), cB (200 nM), and buffer. The second injection of either cA or cB did not result in a change in hybridization signal, indicating that saturation was reached.

The ionic strength of the buffer used in our experiments (23 mM) is much lower than that commonly used for DNA hybridization (e.g. 825 mM for 5x saline sodium citrate buffer). We chose such a low ionic strength because field-effect detection is most sensitive when counter-ion screening of the charged molecules is minimized.[13,14] However at low ionic strength, the electrostatic repulsion between two complementary DNA strands strongly reduces their probability of hybridization and extends the time required for binding.[15,16] Souteyrand and coworkers dealt with these competing ionic strength requirements by performing *ex situ* hybridization on their field-effect sensor at high ionic strength, and then performing the endpoint measurements at much lower ionic strength.[9] Although our measurement was made in real time in low ionic strength buffer, the data shown in Figure 6-2 indicates that saturation is reached within a few minutes of the addition of target oligonucleotides to the fluid cell, which is unusually rapid at this ionic strength. The positively charged PLL layer seems to compensate the negative charge on the probe DNA and reduce the electrostatic repulsion between target and probe DNA. In addition, a positively charged surface may increase the local concentration of target oligonucleotides near the surface.[17] The method of hybridizing nucleic acids on a charge-compensated surface at low ionic strength has been investigated recently for use in rapid microarray hybridization.[17] It might also be used for other field-effect sensing devices such as silicon nanowires,[18] which could lead to a dramatic size reduction of nucleic acids sensors.

We used autoradiography to verify selective hybridization with radiolabeled A, cA, and cB oligonucleotides. We found that the surface coverage after functionalization was approximately 1 probe oligonucleotide per 2 nm^2. Specific target oligonucleotides hybridized with an efficiency of 5% at 80 nM, whereas binding by non-complementary oligonucleotides was less than 0.6%. These experiments with radiolabeled DNA showed that a change in surface potential of $\sim$3 mV corresponds to the binding of 3×10^4 12-mer oligonucleotides per μm^2 or 15 ng of DNA per cm^2. The expected change in Zeta potential, Φ_ζ, for a given change in charge density, Q, can be approximated by,

[13] J. Israelachvili. *Intermolecular and Surface Forces.* Academic Press. London (1992).

[14] P. Bergveld. "The future of biosensors." *Sensors and Actuators A* **56** 65 (1996).

[15] A.P. Williams, C.E. Longfellow, S.M. Freier, R. Kierzek, and D.H Turner. "Laser temperature-jump, spectroscopic, and thermodynamic study of salt effects on duplex formation by DGCATGC" *Biochemistry* **28** 4283 (1989).

[16] J.G. Wetmur, and N. Davidson. *Journal of Molecular Biology* **31** 349 (1968).

[17] Y. Belosludtsev, I. Belosludtsev, B. Iverson, S. Lemeshko, R. Wiese, M. Hogan, and T. Powdrill. "Nearly instantaneous, cation-independent, high selectivity nucleic acid hybridization to NDA microarrays." *Biochemical and Biophysical Research Communications.* **282** 1263 (2001).

[18] Y. Cui, Q. Wei, H. Park, and C. M. Lieber. "Nanowire nanosensors for highly sensitive and selective detection of biological and chemical species." *Science* **293** 1289 (2001).

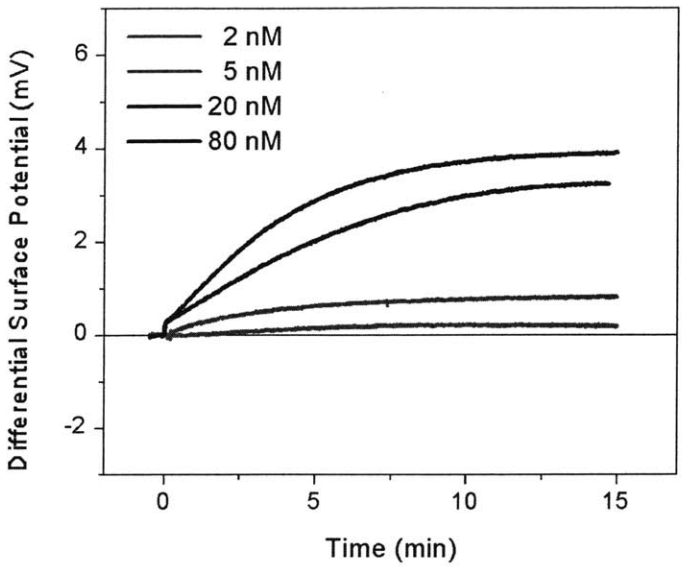

Figure 6-3: Concentration dependence and detection limit
Shown is the differential surface potential response for the hybridization of target oligonucleotides at concentrations of 2, 5, 20, and 80 nM.

$$Q = \sqrt{8\epsilon_w kTqC_o}\sinh\left(\frac{q\Phi_\zeta}{2kT}\right) \tag{6.1}$$

Starting with a surface charge density of silicon dioxide[19] of 0.8 C/m^2, we calculated that a change of the surface charge density from the 3×10^4 hybridized 12-mer oligonucleotides per μm^2 leads to a change in the surface potential of $\sim$ 3 mV which is in good agreement with the observed value. Here we assumed an upper value of 12 charges per oligonucleotide, although their effective charge may be less than that, which would reduce the calculated change in surface potential. The surface charge density of 0.8 C/m^2 is an upper limit for silicon dioxide, and using a lower effective surface charge density would increase calculated change in surface potential.

With an RMS noise voltage of $\sim$6 mV, we can calculate the mass resolution of this system to be 0.1 ng/cm^2, or about 100 molecules per square micron.[20] This is several orders of magnitude worse resolution than can be achieved with fluorescence detection, whose resolution limit is $\sim$0.1 fluorophores per square micron. On the other hand, the label-free methods of QCM and SPR achieve resolutions of $\sim$ 1ng/cm^2, which translates to $\sim$1000 molecules per square micron.[21]

[19]Y. Dong, S. V. Pappu, and Z. Xu, "Detection of Local Density Distribution of Isolated Silanol Groups on Planar Silica Surfaces Using Nonlinear Optical Molecular Probes." *Anal. Chem.* **70** 4730 (1998).

[20]D.J. Duggan, M. Bittner, Y. Chen, P. Meltzer, and J.M. Trent. "Expression profiling using cDNA microarrays." *Nature Genetics* **21, supplement** 12 (1999).

[21]C. Kößlinger, E. Uttenthaler, S. Drost, F. Aberl, H. Wolf, G. Brink, A. Stanglmaier, and E. Sackmann. "Com-

In comparing these systems in it important to keep in mind what parameter each measures. The detection limit of fluorescence is independent of the charge, size, or mass of the target molecule. This is a generalizable result, although the target molecule number resolution (number per unit area) will depend on the labeling efficiency of the system. QCM and SPR both essentially measure mass, so the target molecule number resolution depends on the molecular mass of the target species. QCM and SPR are therefore difficult to apply to low concentrations of small molecules. The field-effect detection limit depends on both size and net charge of target and probe molecules. Short oligonucleotide sequences such as those used in these hybridization detection experiments, are ideally suited to detection by field-effect, at a higher resolution than other label-free methods.

Because the sensor response depends on the change in surface charge during hybridization, the higher charge associated with longer DNA molecules will create a stronger signal per molecule. Whether this will improve the detection limit remains unclear, because the total number of duplexes creased during hybridization will also depend on the surface coverage of longer probe oligonucleotides as well as the affinity and unspecific binding of longer target oligonucleotides.

Figure 6-3 shows the dependence of the hybridization signal on target oligonucleotide concentration and demonstrates that a 2 nM concentration of 12-mer oligonucleotides or 8 ng/mL DNA can be detected easily. Although our detection method is less sensitive than state-of-the-art label-dependent methods[2,3,4] or typical microarray applications that have sensitivities in the tens of picomolar range, our detection limit of 2 nM is one of the lowest values reported thus far for label-independent methods.[5,6,7]

To demonstrate the specificity of our sensors, we investigated two cases where unspecific binding of oligonucleotides to the sensor surface can affect sensor response. First, we successfully detected a specific oligonucleotide within a high concentration of other unrelated oligonucleotides. Figure 6-4 shows the binding of 20 nM cA and cB to A and B, respectively, within a 10-times higher concentration (200 nM) of unrelated sequences. Comparing this signal with a signal from a pure oligonucleotide (Figure 6-3) shows that the high unspecific background reduces the hybridization signal by a factor of 3. Although conventional microarrays are operated at an even higher background to target ratio,[22] we anticipate that further improvement of surface functionalization and hybridization conditions will improve the specificity as well as the sensitivity of our sensor.[23] The

parison of the QCM and the SPR method for surface studies and immunological applications." *Sensors and Actuators B* **24-25** 107 (1995).

[22]E.S. Lander "Array of Hope." *Nature Genetics* **23** 29 (1999).

[23]M.L.M. Andersen. *Nucleic Acid Hybridization* Springer, New York (1999).

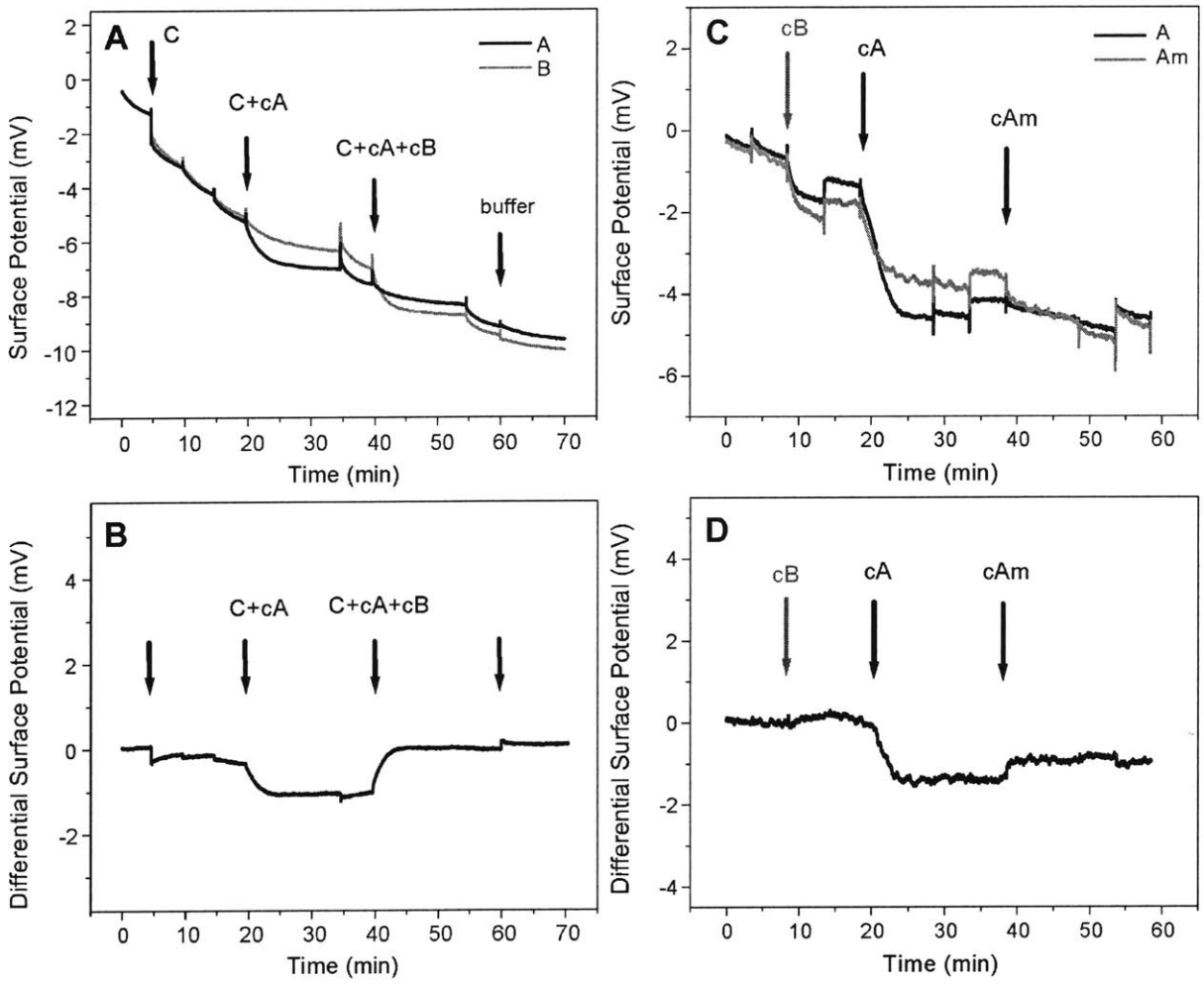

Figure 6-4: Detection within complex sample and detection of single base mismatch. A) Absolute surface potential and B) differntial surface potential for the hybridization of 20 nM oligonucleotides cA to A and cB to B within a 10-times higher concentration of unrelated oligonucleotides. All injections were made at a constant 200 nM concentration. Arrows indicate injections of 200 nM C, then 20nM cA + 180 nM C, and then 20 nM cB + 20 nM cA + 160 nM C. C) Absolute surface potential and D) differential surface potential from two sensors that were functionalized with probe oligonucleotides A and Am, which differ only by a single base. Control solutions with non-complementary target oligonucleotide cB show no differntial signal, whereas injection of 80 nM of complementary sequences cA and cAm both show a distinct hybridization signal.

ability to selectively accumulate and subsequently release analyte molecules within a microfluidic system, as has been recently demonstrated by Huber et al.,[24] may ultimately obviate the need for greater concentration resolution.

Second, Figure 6-4 shows that our field-effect device can identify a single base mismatch in 12-mer oligonucleotides, i.e., it can differentiate between a specific sequence and a sequence that differs only by one base. This is particularly important, because a potential application of DNA sensors is to detect DNA point mutations associated with disease. A pair of sensors was functionalized with oligonucleotides A and Am, a sequence that differs from A at a single base. When cA was injected, the differential signal decreased, showing specific hybridization to A. When cAm was injected the differential signal increased, showing hybridization to Am. The smaller differential signal from binding of cAm to Am compared with that of cA to A could result from a difference in surface functionalization of the two sensors with probe oligonucleotides. However, this trend was subsequently verified by radiolabeling experiments, suggesting that the difference could also result from the several degrees lower melting temperature of the $Am - cAm$ duplex relative to the $A - cA$ duplex. The smaller differential signal from cA in Figure 6-4 compared with that from cA in Figure 6-2 suggests that cA also binds unspecifically to some extent to Am and this reduces the differential signal. Nevertheless, the data in Figure 6-4 demonstrate that our device can distinguish between complementary and mismatched DNA sequences.

We target applications where rapid, parallel DNA analysis is needed, e.g., for characterizing pathogens, measuring mRNA levels during expression profiling or point of care applications. To approach these goals, we anticipate further research toward improvement of concentration sensitivity and of specificity through optimization of experimental conditions, improved surface functionalization, and integration in small-volume fluidic handling systems.

6.2 Investigation of a Model Protein System: Biotin-Avidin

The biotin-avidin complex is a robust molecular recognition system that has an extremely high binding affinity ($> 1000\ \ M^{-1}$). Avidin is a positively charged glycoprotein found in egg whites, with a mass of about 66 kiloDalton. Biotin is a much smaller molecule, 244.3 Dalton, and acts as a coenzyme for carboxylation reactions, necessary for fat and carbohydrate metabolism. Avidin has four binding sites for the much smaller biotin. Avidin's affinity for biotin is much greater than that

[24]D. L. Huber, R. P. Manginell, M. A. Samara, B-I. Kim, and B. C. Bunker. "Programmed Adsorption and Release of Proteins in a Microfluidic Device." *Science* **301** 352 (2003).

of streptavidin, avidin's bacterial counterpart, but also higher unspecific binding. The biotin-avidin system is used here as a well characterized model system for protein interactions. Compared to the DNA used in the previous section, avidin is much larger, an less densely charged.

6.2.1 Alternative Silicon-Based Protein Detection Systems

Many protein systems are difficult to label with fluorescent tags. Instead target proteins are labeled with the small biotin molecule. After binding the biotin-labeled target to the probe-functionalized detection surface, fluorescently labeled avidin binds to the biotin label, enabling fluorescent detection. This sandwich assay is an endpoint detection method that cannot be used for continuous measurement. Considering these limitations, it field-effect sensing is a desirable real-time, label-free detection method. But it's application is limited by practical concerns. In response to the "severe physical limitations, which prevent the often-proposed application as a direct immunosensor,"[25] several alternative detection schemes have been proposed for protein detection with field-effect sensors.

One approach presented by Koch and coworkers is the use of a differential pair of ISFETs arranged at opposite ends of a fused silica capillary to make streaming potential measurements.[25] Rather than measuring reactions taking place directly on the ISFET surface, the zeta potential of the fused silica capillary was measured after lysozyme was covalently bonded to the silanized silica surface along the length of the capillary. Zeta potential vs. pH curves were significantly altered after lysozyme binding, in good agreement with predictions of the site-binding model. Because of the measurement technique, however, this approach would be difficult to apply to real-time detection.

Another approach is the analysis of ISFET response to stepwise change in electrolyte concentration.[26,27,28] Upon a stepwise change in electrolyte concentration, the capacitance at the sensor surface changes almost immediately, according to the dielectric relaxation time of the system. The surface charge responds more slowly, limited by reaction kinetics. The surface potential is temporarily out of equilibrium. When species interact with the sensor surface, the transient potential

[25]S. Koch, P. Woias, L.K. Meixner, S. Drost. and H. Wolf. "Protein detection with a novel ISFET-based zeta potential analyzer." *Biosensors and Bioelectronics* **14** 417 (1999).

[26]R. B. M.Schasfoort, R. P. H. Kooyman, P. Bergveld, and J. Greve. "A new approach to immunoFET operation." *Biosensors and Bioelectronics* **5** 103 (1990).

[27]J. C. van Kerkhof, J. C. T. Eijkel, and P. Bergveld. "ISFET responses on a stepwise change in electrolyte concentration at constant pH." *Sensors and Actuators B* **18-19 56** (1994).

[28]P. Bergveld, R.E.G. van Hal, and J.C.T. Eijkel. "The remarkable similarity between the acid-base properties of ISFETs and proteins and the consequences for the design of ISFET biosensors." *Biosensors and Bioelectronics* **10** 405 (1995).

response is much greater than the steady state potential response. This method requires a complicated setup, and is also difficult to apply to real-time detection.

A third approach is the work by Bataillard and coworkers using EIS capacitors to make impedance, rather than potentiometric, measurements of immunospecies in a label-free way.[29] In this work, the capacitance of the EIS structure is measured at a fixed bias point in the accumulation regime as proteins adsorb at the interface. This method is limited to the detection of relatively thick layers, at least several nanometers. Since the silicon capacitance is fixed in this regime, change in capacitance of the structure is attributed to additional series capacitance contributed by the protein layer at the surface, and the thickness of such layers is estimated. Real-time measurements were presented for the binding of α-fetoprotein to anti-α-fetoprotein. In this configuration, the EIS structure is used as a convenient passivated electrode for impedance measurement, rather than as a field-effect sensor, per-se.

Given the improved surface potential resolution demonstrated by the sensors used in this thesis work, as well as the successful detection of nucleic acid hybridization, we are interested in investigating the detection of protein interactions. Meixner and Koch's modeling work[30] suggests that sensitivities in the millivolt range should be sufficient. Here we investigate whether the improved surface potential resolution is sufficient to enable detection of protein interaction, and whether higher resolution measurements can yield more detailed insight into charge screening issues.

6.2.2 Binding Experiments

In these experiments, avidin binding to biotinylated-Bovine Serum Albumin (bBSA) was measured across a range of buffer concentrations to investigate charge screening effects. A variable concentration of NaCl, (10, 30, 60, 100 mM) was added to 5 mM phosphate buffer at pH 6. Sensors were equilibrated in buffer for at least an hour, and then incubated individually with 0.1 mg/mL bBSA or BSA. Sensors were rinsed thoroughly iwth buffer, returned to the fluid cell and allowed to equilibrate for severalhours. Avidin concentration was typically 760 nM. This relatively high concentration was chosen to such that saturation binding would occur on tractable time scale. In other experiments, lower avidin concentrations were used, down to 10 nM. Binding rate slowed for lower concentrations, and subsequent injections were required before the surface potential response

[29]P. Bataillard, F. Gardies, N. Jaffrezic-Renault, C. Martelet, B. Colin, and B. Mandrand. "Direct Detection of Immunospecies by Capacitance Measurements." *Analytical Chemistry* **60** 2374 (1988).

[30]L.K. Meixner and S. Koch. "Simulation of ISFET operation based on the site binding model." *Sensors and Actuators B* **6** 315 (1992).

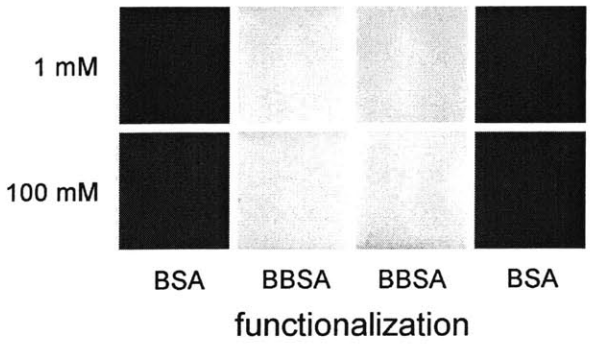

Figure 6-5: Fluorescence image of labeled avidin binding to BSA and bBSA functionalized surfaces at low and high ionic strength

saturated at a total value commensurate with saturation at higher concentrations.

Biotin-avidin binding is known to be high across a broad range of buffer concentrations. We verified this for our experimental procedure by optical measurement of fluorescently tagged avidin binding to biotinylated-BSA on a glass surface prepared and functionalized identically to our sensor. Data is shown in Figure 6-5. We found that labeled-avidin binding increased slightly with increasing buffer concentration.

For each trial, buffer was injected into the fluid cell several times, and BSA was injected to coat any exposed surfaces, with the intent of minimizing non-specific binding. 950 μL aliquots of .05 mg/mL avidin were injected into the fluid cell, and the sensor response was allowed to stabilize. Subsequent avidin injections did not increase signal, and subsequent buffer injection did not decrease signal. From this, we conclude the avidin binding to be saturated and irreversible under the conditions of the experiment.

Typical binding curves for 10, 30, 60, and 100 mM NaCl concentrations are shown in Figure 6-6A. These experiments were repeated multiple times for each concentration and the total equilibrium surface potential change is shown in Figure 6-6B. Based on the fluorescence measurements indicating a trend of increasing avidin binding with increasing buffer concentration, we conclude that the decreased signal is due to ionic screening which partially shields charge from exerting an electric field on the sensor silicon.

Subsequent measurements were made in which biotinylated-BSA was introduced into the reaction chamber after avidin binding. Avidin and b-BSA were alternately introduced to the sensor in order to build up protein multilayer on the sensor surface. This is possible because avidin is tetrameric and each BSA molecule has several biotin units. The surface potential response to

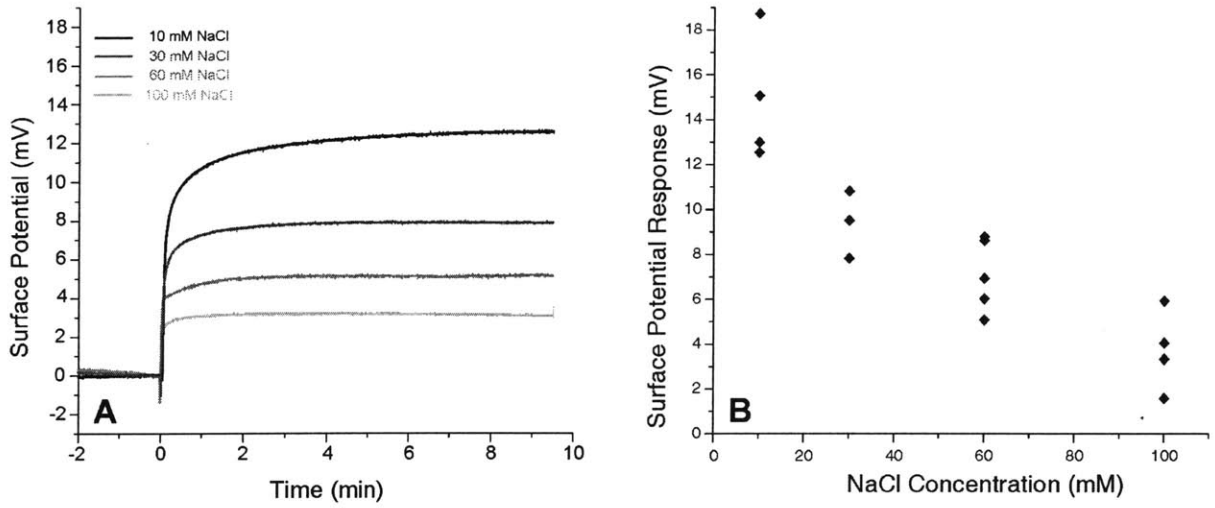

Figure 6-6: Charge screening effect on biotin-avidin binding measurements
A) Surface potential response of biotinylated-BSA-functionalized surface to avidin binding at various salt concentrations. Buffer solutions were 5 mM phosphate buffer with 10, 30, 60, or 100 mM NaCl added. At t=0, 1 mL of 760 nM avidin was injected into the fluid cell. Decreased surface potential response for higher concentrations indicates greater charge screening. B) Summary of multiple trials over the range of salt concentrations. The variation in surface potential response for a given buffer concentration is likely due to variations in the chemical growth of the gate oxide.

subsequent layers diminished rapidly, showing a characteristic quite different from that of the polyelectrolyte multilayers (Chapter 4), which maintained a high surface potential response with the addition of each subsequent layer. This suggests that the b-BSA/avidin complex forms a more porous layer, which can be readily screened by counter-ions. This is perhaps due to the conformational restrictions imposed by specific binding.

For each salt concentration, a spread of several millivolts was seen for the equilibrium avidin binding signal, shown in Figure 6-6B. Such variations are likely due to variations density of probe molecules on the surface, which depend on the functionalization conditions as well as the surface charge state of the sensor after the cleaning procedure. Several devices were used in these trials, and no clear trend was observed linking sensitivity to sensor lifetime.

Data shown in Figure 6-6 refer to the single-ended signal of the b-BSA functionalized sensor. In each experiment, however, high non-specific binding signals were observed from the BSA functionalized sensor. The differential signal (b-BSA minus BSA functionalized), shown in Figure 6-7A also shows a several-millivolt variation among separate trials. However, viewing the differential signal as a percentage of the total signal for each sensor reveals an interesting trend. Plotting the data this way, as in Figure 6-7 can be used to interpret the ratio of specific vs. non-specific binding,

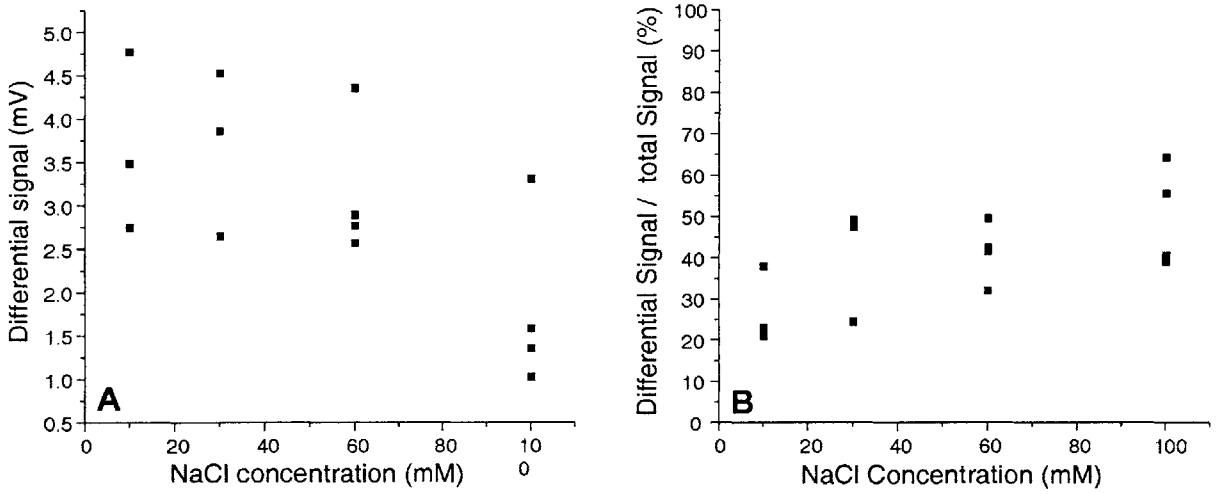

Figure 6-7: Differential surface potential response of biotin-avidin binding
A) Differential surface potential response (sensor1-sensor2) to avidin injection, where sensor 1 was functionalized with biotinylated-BSA, and sensor 2 was passivated with BSA. Shown for multiple independent trials at 10, 30, 60, and 100 mM NaCl concentration in 5 mM phosphate buffer. B) Differential surface potential response divided by single-ended response of sensor 1. The upwards trend with increasing buffer concentration indicates greater specificity of the surface at higher buffer concentrations.

showing a trend of greater specificity at high buffer concentrations. This is expected because higher concentration buffers will contribute greater charge screening, which would minimize non-specific electrostatic interactions.

DNA hybridization and biotin-avidin binding are examples of direct detection of specific molecular recognition events between unlabeled molecules. These demonstrations imply that questions formerly thought to be closed are worth re-examining in the advent of: a) development of robust high-resolution sensor; b) clever surface functionalization techniques currently under development; c) advances in MEMS, especially microfluidics and integration. We anticipate further optimization of measurement systems, fluid delivery, and surface functionalization techniques, to extend the capabilities demonstrated above. Novel surface chemistries possessing both a molecular recognition element and a means of modulating charge near the sensor surface would greatly extend the capabilities of field-effect sensors.

Chapter 7

Length Scaling in Potentiometry

The bulk of the work presented in this thesis has been concerned with the development of potentiometric biosensors producible by batch microfabrication techniques, aimed at integration. This work has sought to lay a foundation for high-resolution measurement of ensembles of molecules on a surface, where performance metrics include resolvable charge per unit area and minimum detectable concentration. Optimally, these types of measurements are performed in a small fluid volume that minimizes analyte consumption. However, some hundreds to thousands of molecules per square micron are measured. This is in contrast to single-molecule measurements or measurements on small numbers of molecules. Ensemble measurements capture average properties of large numbers of molecules; greater insight is enabled by making multiple single-molecule measurements to understand the distribution of properties which are represented in the ensemble average.

Single-molecule methods require feature sizes on the order of the target molecules themselves — typically a few nanometers. This is far below the the processing capability of state-of-the-art integrated circuit fabrication techniques, and indeed below the limits of optical lithography. Single-molecule methods necessitate the fabrication of sensors by serial processing methods, with little automation.

In recent years, novel methods have yielded insight into the biomechanics of single molecules. Optical tweezers, for example, have been used to elucidate function of molecular motor proteins (actin-myosin, kinesin transport along microtubules, rotary motors), DNA transcription, and protein folding.[1] Molecular force microscopy, a scanning probe technique, has been used to investigate

[1] A.D. Mehta, M. Rief, J. A. Spudich, D. A. Smith, and R. M. Simmons. "Single-Molecule Biomechanics with Optical Methods." *Science* **283** 1689 1999.

protein and nucleic acid structure and folding, and inter- and intra-molecular binding.[2]

The development of electronic measurements of single-molecules, however, is still in its infancy. One notable recent demonstration was the electronic measurement of transport of a single DNA molecule through a nanopore.[3] Progress toward nanoscale electrometers is being developed along two primary axes. In the first, the length-scale limited component is fabricated in a batch process, attached to a surface, and the connecting circuit is built around the nanoscale component. In the second approach, nanoscale components are patterned *sur place* with high-resolution methods.

Carbon nanotube and silicon nanowire sensors fall into the first class of nanoscale sensors. Single-walled carbon nanotubes (SWNTs), for example, are typically grown by catalyst-assisted chemical vapor deposition. The resulting SWNTs, which typically have diameters between 1 and 5 nm, have been demonstrated to undergo dramatic changes in electrical properties upon adsorption of certain molecules or polymers, showing the potential for gas-phase and solution phase sensing.[4] In other work, the growth of carbon nanotubes has been directed into circuit configurations.[5,6,7] The sum of these developments lays the groundwork for complete biosensing circuits.

Silicon nanowires have also been demonstrated as nanoscale potentiometric biosensors. A field-effect transistor was constructed by patterning source and drain contacts[8,9] on a 10-20 nm diameter boron-doped silicon nanowire fabricated by laser catalytic growth.[10] Silica surface functionalization techniques were used to modify the nanowires, which were used to detect pH changes, biotin-streptavidin binding, antibody binding, and real-time, enzyme regulation.[11]

The second approach, the direct patterning of nanoscale components, is challenging. One method of building a nanoscale field-effect transistor (FET) is to create silicon nanowires within an

[2]M. Rief, F. Oesterhelt, B. Heymann, and H.E. Gaub. "Single Molecule Force Spectroscopy on Polysaccharides by Atomic Force Microscopy." *Science* **275** 1295 (1997).

[3]A. Meller, and D. Branton. "Single molecule measurements of DNA transport through a nanopore." *Electrophoresis* **23** 2583 (2002).

[4]J. Kong, N.R. Franklin, C. Zhou, M.G. Chapline, S. Peng, K. Cho, and H. Dai. "Nanotube molecular wires as chemical sensors." *Science* **287** 622 (2000).

[5]H.T. Soh, C.F. Quate, A.F. Mrpurgo, C.M. Marcusa, J. Kong, and H. Dai. "Integrated nanotube circuits: Controlled growth and ohmic contacting of single-walled carbon nanotubes." *Applied Physics Letters* **75** 627 (1999).

[6]Y. Zhang, A. Chang, J. Cao, Q. Wang, W. Kim, Y. Li, N. Morris, E. Yenilmez, J. Kong, and H. Dai. "Electric-field-directed growth of aligned single-walled carbon nanotubes." *Applied Physics Letters* **79** 3155 (2001)

[7]C. Zhou, J. Kong, E. Yenilmez, and H. Dai. "Modulated chemical doping of individual carbon naotubes." *Science* **24** 1552 (2000).

[8]Y. Huang, X. Duan, Q. Wei, and C. M. Lieber. "Directed Assembly of One-Dimensional Nanostructures into Functional Networks." *Science* **291** 630 (2001).

[9]Y. Cui, and C. M. Lieber. "Functional Nanoscale Electronic Devices Assembled Using Silicon Nanowire building Blocks." *Science* **291** 851 (2001).

[10]Y. Cui, X. Duan, J. Hu, and C. M. Lieber. "Doping and Electrical Transport in Silicon Nanowires." *Journal of Physical Chemistry B* **104** 5213 (2000).

[11]Y. Cui, Q. Wei, H. Park, and C. M. Lieber. "Nanowire nanosensors for highly sensitive and selective detection of biological and chemical species." *Science* **293** 1289 (2001).

existing circuit. In the work of Fujii et al.,[12,13] an air-bridge nanowire was formed by patterning a thin waist of a bow-tie geometry on a SOI substrate, and then subsequently oxidizing[14,15] the bridge until the remaining silicon was nanometers in diameter, and had electrical connections fabricated at the source and drain. While this method uses batch fabrication methods exclusively, the features sizes are difficult to control.

In the following work, we apply an alternative fabrication method to an experimental electrometer. Rather than developing a nanoscale FET, this work was concerned with the fabrication of a Single-Electron-Transistor (SET). The ability to resolve 10^{-4} to 10^{-5} $e/\sqrt{Hz}$ has been demonstrated with single electron transistors operating at cryogenic temperatures.[16] This extreme resolution could yield unique insight into intermolecular forces and structure-function relationships. There are several developmental challenges faced in bringing this technology to biology, however. The first challenge is the development a sensor with sufficiently high current at room temperature. While SETs have demonstrated extremely high charge resolution at cryogenic temperatures, the development of an SET operation at room temperature — a requirement for biological application — is ongoing.[17,18,19] Subsequent development will be required to establish how such a sensor functions in electrolyte solution, as well as how to functionalize the gate effectively. Encouraging work has been developed in the Feldheim group, where a scanning tunneling microscope (STM) based SET was developed that operates in solution and is gated by pH.[20]

[12]H. Fujii, S. Kanemaru, T. Matsukawa, H. Hiroshima, H. Yokoyama, and J. Itoh. "Fabrication of a Nanometer-Scale Si Wire by Micromachining of Silicon-on-Insulator Substrate." *Japanese Journal of Applied Physics* **37** 7182 (1998).

[13]H. Fujii, S. Kanemaru, T. Matsukawa, and J. Itoh. "Air-bridge-structrued siliocn nanowire and anomalous conductivity." *Applied Physics Letters* **75** 3986 (1999).

[14]H.I. Liu, D.K. Biegeglsen, N.M. Johnson, F.A. Ponce, and R.F.W. Pease. "Self-limiting oxidation of Si nanowires." *Journal of Vaccuum Science and Technology B* **11** 2532 (1993).

[15]H.I. Liu, D.K. Biegelsen, F.A. Ponce, N.M. Johnson, and R.F.W. Pease. "Self-limiting oxidation for fabricating sub-5 nm silicon nanowires." *Applied Physics Letters* **64** 1383 (1994).

[16]K.K. Likharev. "Single Electron Devices and Their Applications." *Proceedings of the IEEE.* **87** 606 (1999).

[17]S.J. Tans, A.R.M. Versheueren, and C. Dekker. "Room-temperature transistor based on a single carbon nanotube." *Nature* **393** 49 (1998).

[18]L. Zhuang, L. Guo, and S.Y. Chou. "Silicon single-electron Quantum-dot transistor switch operating at room temperature" *Applied Physics Letters* **72** 1205 (1998).

[19]L. Guo, E. Leobandung, and S. Y. Chou. "A room-temperature silicon single-electron metal-oxide-semiconductor memory with nanoscale floating-gate and ultranarrow channel." *Applied Physics Letters* **70** 850 (1997).

[20]W.P. McConnell, J. P. Novak, L.C. Brousseau III, R. R. Fuierer, R.C. Tenent, and D. L. Feldheim. "Electronic and Optical Properties of Chemically Modified etal Nanoparticules and Molecularly Bridged Nanoparticle Arrays." *Journal of Physical Chemistry B* **104** 8925 (2000).

7.1 Towards a Room Temperature Single Electron Transistor

The challenge for room-temperature SET operation is to develop of devices with high tunneling current, but small tunneling capacitance. A small tunneling capacitance is preferable because the charging energy, $E = \frac{q^2}{C}$, required to add one extra electron to the island must be greater than the energy of thermal fluctuations, $E >> kT$. This capacitance represents the capacitance between the island and the world. The tunneling current, however, requires narrow tunnel junctions to lower the tunneling barrier. Gotoh and coworkers show, through 3-dimensional modeling, that for nanometer scale feature sizes, the capacitance of the island changes little when the tunnel junction width is decreased.[21] This is because fringing fields in the substrate dominate the parallel plate capacitance of the tunnel junctions between source and island, and island and drain. The implication of this is that making shorter tunnel junctions increases the tunneling current without increasing the tunneling capacitance.

The Matsumoto group at the Electrotechnical Laboratory in Tsukuba, Japan has fabricated a series of SET structures using scanning probe nano-oxidation to pattern oxide features on an atomically flat titanium substrate.[22,23,24] By this method, a scanning probe is brought in close proximity to a thin metal film and a negative bias voltage is applied to the probe tip in the presence of water adsorbed on the surface, creating localized oxidation, as shown in Figure 7-1.

The structure fabricated by the Matsumoto group is shown schematically in Figure 7-2. A single island is sandwiched by two tunnel junctions, which are defined by the SWNT tip nano-oxidation process. In this planar device, current is modulated by charge on the side gate. The source-drain barrier and the gate barriers are at least 1 micron wide to eliminate leakage.

Field-induced oxidation was originally developed on silicon with the STM by Dagata et al.[25,26]

[21] Y. Gotoh, K. Matsumoto, T. Maeda, E.B. Cooper, S.R. Manalis, H. Fang, S.C. Minne, T. Hunt, H. Dai, J. Harris, and C.F. Quate. "Experimental and theoretical results of room-temperature single-electron transistor formed by the atomic force microscope nano-oxidation process" *Journal of Vaccuum Science and Technology A* **18** 1321 (2000).

[22] K. Matsumoto. "STM/AFM nano-oxidation process to room-temperature-operated single-electron transistor and other devices" *Proceedings of the IEEE* **85**612(1997).

[23] K. Matsumoto, M. Ishii, K. Segawa, Y. Oka, B.J. Vartanian, and J.S. Harris. "Room temperature operation of a single electron transistor made by the scannign tunneling microscope nanooxidation process for the TiOx/Ti system." *Applied Physics Letters* **68** 34 (1996).

[24] K. Matsumoto, Y. Gotoh, T. Maeda, J.A. Dagata, and J.S. Harris. "Room temperatre Coulomb oscillation and memory effect for single electron memeory made by pulse-mode AFM nano-oxidation process." *Internantional Electron Devices Meeting 1998 Technical Digest* 449 (1998).

[25] J.A. Dagata, J. Schneir, H.H. Harary, C.J. Evans, M.T. Pstek, and J. Bennett."Modification of Hydrogen-Passivtaed Silicon by a Scanning Tunneling Microscope Operating in Air. *Applied Physics Letters* **56** 2001 (1990).

[26] J. A. Dagata, J. Schneir, H. H. Harary, J. Bennet, and W. Tseng. "Pattern Generation on Semiconductor Surfaces by a Scanning Tunneling Microscope Operating in Air." *Journal of Vaccuum Science and Technology B* **9** 1384 (1991).

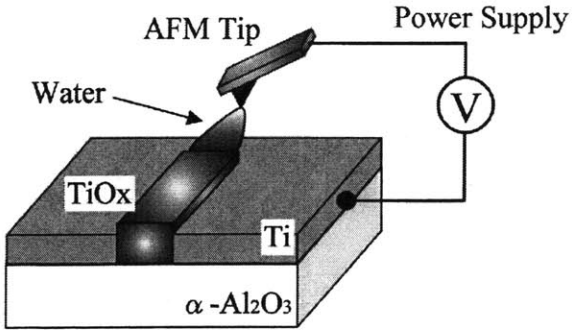

Figure 7-1: Local oxidation lithography schematic

and on titanium with the STM by Sugimura et al.[27] Subsequently, Snow and Campbell developed field-induced oxidation of silicon with the AFM.[28] This local oxidation had since been well characterized in terms of parameters such as tip-diameter, substrate roughness, field strength, scanning rate, tip-sample distance, and environment.[29, 30,31,32] However, the diameter of the proximal probe tip and the surface roughness of the substrate ultimately limit the minimum attainable feature size.

In the following work, the localized oxidation of the critical features — the tunnel barriers — was performed with a single-walled carbon nanotube (SWNT) tip, grafted onto a commercially available AFM cantilever. The diameter of the SWNT is as small as 2-5 nm. This is several times smaller than the apex of conventional silicon AFM tips, whose radius of curvature is as small as 20 nm, or even oxide-sharpened silicon AFM tips, whose radius of curvature is as low as 5 nm.

Prior to this work, multiwalled carbon nanotubes were used to write lines as narrow as 10 nm.[33] Nanotubes have proven to be quite resistant to wear, enabling them to write large areas without tip degradation. Silicon tips, by comparison, wear with use. The smaller diameter nanotube allows sub-10-nm features to be written, while at the same time permitting larger features to be written

[27]H. Sugimura, R. Uchida, N. Kitamura, and H. Mashuhara. "Scanning Tunneling Microscope Tip-Induced Anodization for Nanofabrication of Titanium." *Journal of Physical Chemistry* **98** 4352 (1994).

[28]E. S. Snow and P. M. Campbell. "Fabrication of Si Nanostructures with an Atomic-Force Microscope." *Applied Phsyics Letters* **64** 1932 (1994).

[29]P. Avouris, R. Martel, T. Hertel, and R. Sandstrom. "AFM-tip-induced and current-induced local oxidation of silicon and metals" *Applied Phyics A - Materials Science and Processing.* **66** S659 (1998).

[30]F. Perez-Murano, K. Birkelund, K. Morimoto, and J. A. Dagata. "Voltage modulation scanned probe oxidation." *Applied Physics Letters* **75** 199 (1999).

[31]J.A. Dagata, T. Inoue, J. Itoh, K. Matsumoto, and H Yokoyama. " Role of space charge in scanned probe oxidation" *Journal of Applied Phyiscs* **84** 6891 (1998).

[32]J. A. Dagata, T. Inoue, J. Itoh, and H. Yokoyama. "Understanding scanned probe oxidation." *Applied Physics Letters* **73** 271 (1998).

[33]H. Dai, N. Franklin, and J. Han. "Exploiting the Properties of Carbon Nanotubes for Nanolithogrpahy." *Applied Physics Letters* **73** 1508 (1998).

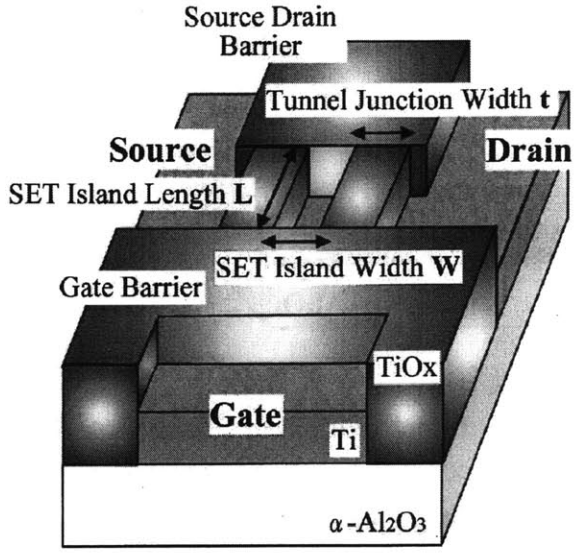

Figure 7-2: Single-electron transistor schematic

more reliably.

The single-walled carbon nanotube tips used here were synthesized by chemical vapor deposition on the tip of a commercial silicon cantilever[34], shown in Figure 7-5. First, a catalyst solution to promote SWNT growth was prepared by hydrolyzing $FeCl_3$ in ethanol to produce iron oxide. A supporting gel matrix was formed of aluminum and silicon oxides. Molybdenum oxide was used as a promoter. The tubes were dipped in the catalyst solution and then exposed to chemical-vapor deposition of CH_4 at 900 ° C Since the catalyst coats the entire surface of the cantilever tip, nanotubes grow at many sites and follow the contour of the surface. The sharp discontinuity at the pyramid tip allows the nanotube to extend beyond the surface, sometimes over a micron in length.

Tips synthesized by this process often have a single nanotube tip extending from the cantilever pyramid, although sometimes multiple nanotubes form small bundles. SWNT tips range in length from a few nanometers to more than a micron. After synthesis, most tips must be trimmed in order to isolate a single nanotube less than 65 nm long that is suitable for reliable imaging and writing. A tip that is too long with either buckle during writing, producing wider features, or traverse the surface with a slip-stick motion, producing intermittent oxidation, shown in Figure 7-3.

Nanotube tips were shortened by applying a series of 500-μs voltage pulses ranging from 20 to 60 V between the nanotube and the titanium surface. During the tip-shortening process, a

[34] 250 μm length. 60-80 kHz resonance. From Digital Instruments, Santa Barbara, CA 93117.

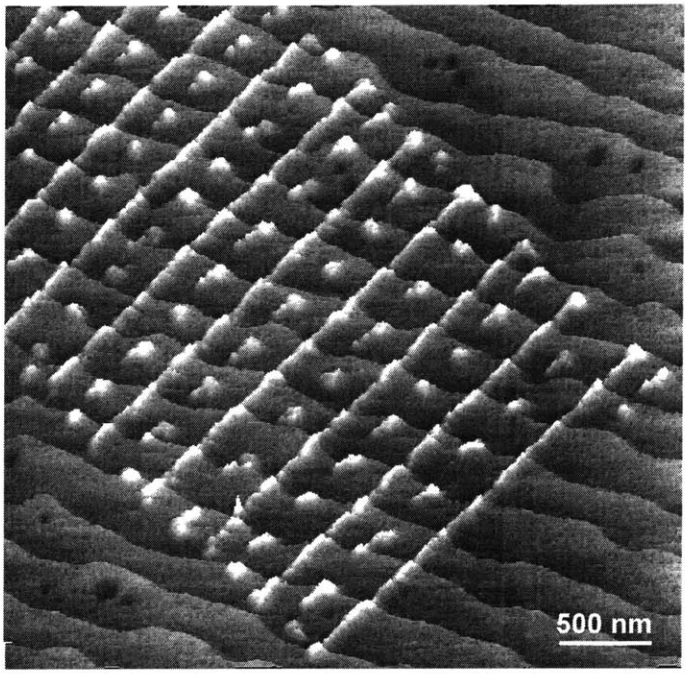

Figure 7-3: Nanolithography produced by slip-stick motion of long nanotube tip. Atomic force micrograph of Al_2O3 surface showing broken oxide lines created by slip-stick motion of nanotube tip traversing crystal planes.

commercial AFM (Digital Instruments, Santa Barbara, CA 93117) is used to measure the (RMS) amplitude and deflection of the cantilever versus tip-sample separation. The cantilever is driven at resonance while a piezotube scans the cantilever over a range of a few hundred nanometers in a direction orthogonal to the substrate. The scan range of the tip-sample separation is adjusted so that the tip only contacts the surface for the last ~10 nm of the scan. A noticeable shift in the amplitude and deflection curves occurs when the tip is successfully shortened. Figure 7-4 shows the response from a nanotube which has been shortened to ~45 nm. An example of a completed SWNT lithography tip is shown in Figure 7-5

7.1.1 Substrate

Our substrate consists of a 2-nm-thick conformal layer of titanium on an atomically flat $\alpha - Al_2O_3(1012)$ surface.[35] Before evaporation, the surface is extremely clean and ideal for titanium adhesion. The surface roughness is approximately 1 Å, which is critical for two reasons. First it allows consistent, repeatable lithography. Extreme discontinuities in the surface cause sticking and

[35]Surface preparation: After organic cleaning, the $\alpha - Al_2O_3$ surface is annealed in air at 1100 C for 30 minutes, and 2 nm titanium is evaporated at a rate of 1 Å per second at $\sim 10^{-8}$ Torr.

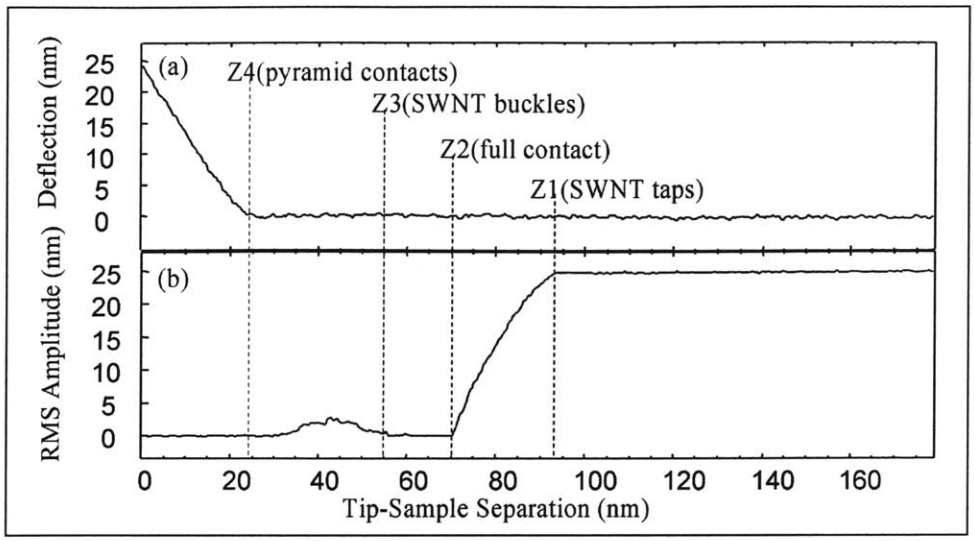

Figure 7-4: Force-Distance characterization of nanotube preparation

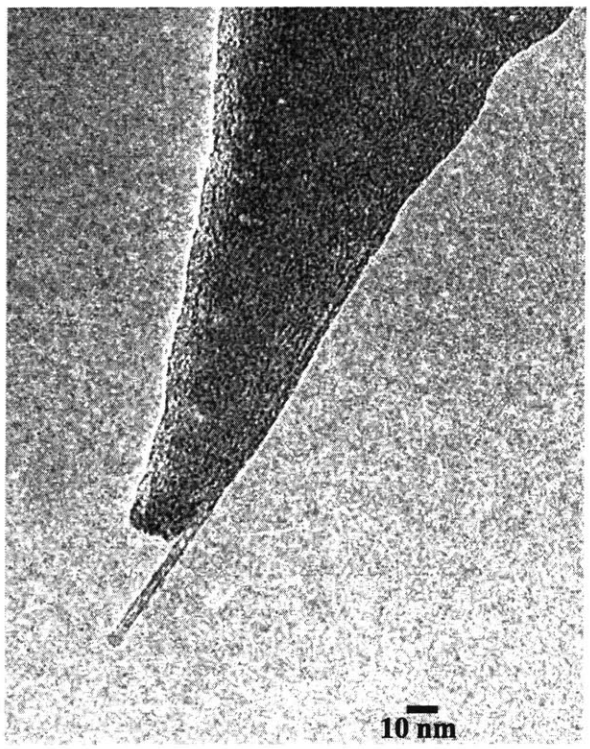

Figure 7-5: Transmission electron micrograph of atomic force microscope tip with carbon nanotube stylus

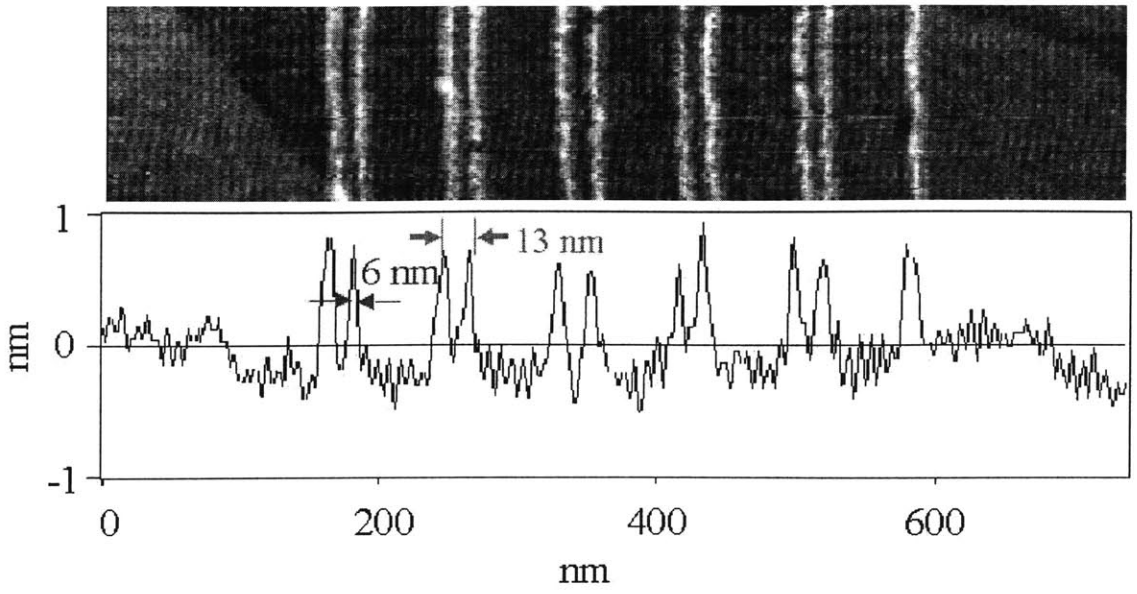

Figure 7-6: 6-nm-wide tunnel barriers for SET

deformation of patterned features. Second, since the average height of the titanium oxide features is approximately 1 nm, high surface roughness can cause ambiguity in reading features.

7.1.2 Patterning

Features were both patterned and imaged in the tapping mode. A 10 Hz square wave of +.5 V and -8.5 V was applied, while scanning the tip 40-100 μm/s. This produced lines as small as 6 nm wide, an 1 nm tall[36], as shown in Figure 7-6. Low voltages will not induce oxidation, and very high voltages will produce excessively large features.[22,29,30]

7.1.3 Results and discussion

A SET was fabricated according to the schematic shown in Figure 7-2, with 8-nm wide tunnel barriers defined by the SWNT nano-oxidation process. Coulomb oscillations measured with this device are shown in Figure 7-7. The drain bias was set at 5 V and the gate bias was swept from 1 to 8 V. The apparent period of Coulomb oscillation are about 1 V, from which it is estimated that the gate capacitance is 1.6×10^{-19} F. The drain current of the SET is on the order of 10^{-13} amperes,

[36]This patterning technique has additionally been applied by the author to ultra-high density data storage,[37] and the interested reader is referred to Appendix B for a description of this work

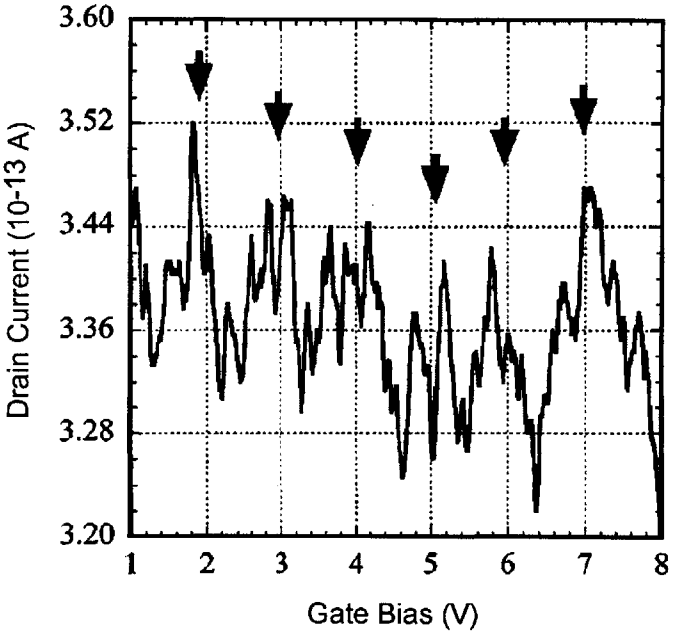

Figure 7-7: Current-voltage characterization of room temperature SET

with a signal to noise ratio of 3 to 4. For SETs with tunnel junctions 20 nm wide, fabricated by with conventional silicon AFM tips was on the order of 10^{-14} to 10^{-15} amperes.

Several gate voltage sweeps were made under various drain bias conditions, and in each case, the current showed oscillation peaks at the same gate voltages, indicating that the data shown in Figure 7-7 are indeed Coulomb oscillations, rather than random noise fluctuations. Nevertheless, the signal-to-noise ratio exhibited by this device leaves much room for improvement.

Although the SWNT nanolithography used in this work produced SETs with higher current at room temperature, the increase was not as great as expected. It is speculated that the quality of the oxide differs due to the difference in scanning rates of the SWNT tip versus the silicon tip.

The nanolithography technique described here is capable of patterning features of the appropriate length scale for single-molecule work. Further development of this sensing technique is necessary if single-molecule-scale potentiometers are to have practical application as sensor systems for single molecule mechanics have.[1,38]

[38]J. Fritz, D. Anselmetti, J. Jarchow, and F. Busquets. "Probing Single Biomolecules iwth Atomic Force Microscopy." *Journal of Structural Biology* **119** 165 (1997).

Chapter 8

Conclusion

Field-effect sensing represents an appealing vision for direct electrical measurement of biomolecular interactions within a compact, highly integrated system. This thesis has explored scaling the gate dielectric towards its limit. Sensors were produced with greatly improved surface potential resolution and real-time readout. Sensor performance was characterized and modeling assumptions were re-evaluated to establish appropriate data interpretation. This work has incorporated recent advances in multiple fields to apply field-effect sensing to specific molecular detection, exploring opportunities and limitations. Doing so has enabled a clearer vision of next steps to be traversed if this sensing system is to have wide applicability.

8.1 Thesis Contributions

Sensors with improved surface potential resolution have been developed by reducing the gate oxide thickness. Through modeling, fabrication parameters have been tailored to produce robust, effective devices. Device performance has been characterized in terms of surface potential resolution, noise, leakage, and drift. Drift was found to be commensurate with that of EIS sensors with much thicker oxide insulators. Leakage was found to be less than for polysilicon-gated MOS devices of equivalent oxide thickness, due to the ionic nature of the electrolyte gate contact. Theoretical analysis has been coupled with empirical evidence to verify data interpretation methods. Detection of biotin-avidin binding has been investigated, and charge screening effects have been investigated over a range of buffer conditions. Combining surface chemistry, differential readout, and improved surface potential resolution, the real-time, label-free detection of DNA has been demonstrated at low nanomolar concentrations. Finally, fabrication techniques for scaling the lateral dimension

of potentiometric devices have been demonstrated, enabling the fabrication of a single-electron transistor demonstrating Coulomb oscillations at room temperatures.

8.2 Outlook, Challenges, and Future Work

Some contributions of the present work are more subtle. Through working on device engineering aspects of an EIS system, it has become clearer which other aspects of the sensor must be improved for future application. Development of appropriate surface functionalization techniques will critically determine the path of field-effect biosensing. Reliability of assays will be enhanced by the development surface preparation procedures resulting in more reproducible oxide surface condition.

This work has focused on sensor development within the context of eventual integration into compact analytical systems. Appropriate materials and techniques were employed with an eye toward further system development. The integration of sensors into systems will be necessary to more clearly understand the both the ultimate capabilities and applications of this technology. Properties of the system, rather than just the sensing element, will determine benchmarks such as concentration and mass sensitivity, and time resolution of measurements.

8.2.1 Assay Development

As we approach the limit of surface potential resolution for microscale field-effect sensors, it becomes clear that the development of surface functionalization techniques is one of the most important aspects for enabling label-free assays. For example, the detection of DNA hybridization demonstrated in this work is facilitated by the electrostatic binding method used; covalent functionalization techniques have been less successful. Yet, electrostatic binding has its own limitations. Typically, hybridization assays undergo various stringency elutions, such as exposure to high salt concentration or high temperature in order to remove non-specifically bound molecules. Rather than improving our system's sensitivity, these methods would likely dissociate the probe DNA layer in our system, effectively de-functionalizing our surface. The challenge, then, is to design covalent functionalization systems that create an appropriate charge micro-environment at the insulator surface, in addition to appropriate covalent attachment sites for probe molecules.

The detection of hybridization of short oligonucleotides that has been demonstrated in this work is an example of a particularly appropriate system for field-effect detection. These molecules are small and highly charged, meaning that a great deal of charge is manipulated very close to the sensor

surface. The mass detection limit of Quartz Crystal Microbalance and Surface Plasmon Resonance make them ill-suited for small-molecule detection, although they are commercially available and find wide applicability for other applications.

As was demonstrated by the biotin-avidin binding experiments, however, field-effect sensing faces serious challenges for general applicability. For these experiments it seems that nonspecific binding of relatively few molecules taking place very close to the sensor surface overwhelmed the electrical signal from many more molecules binding specifically, but farther from the surface. These measurements can be contrasted to the electrostatic adsorption of multilayers, where large signals were seen even for interactions taking place relatively far from the sensor surface. This is likely caused by the dense packing of each of the layers, effectively excluding counter-ions in solution. It would be ideal, then, to develop a surface chemistry that prevented nonspecific binding while forming a dense layer, excluding charge screening, effectively moving the sensor surface closer to binding sites. This is a conceptual proposal drawn at the cartoon level—in reality, the kinds of molecules that form dense layers are highly charged, making them attractive sites for non-specific binding, and recognition elements may require some radius of gyration—some freedom to move about.

Another route is the development of molecular recognition systems where recognition events take place beyond the charge screening length but actuate a charge fluctuation closer to the sensor surface. Aptamer beacons developed in the Ellington lab[1] are a powerful prototype of this sort of interaction. In this work, nucleic acid sequences are created to form hairpin-like loops: the ends are complementary sequences, and the central loop acts as a recognition element. The ends are functionalized with a fluorescence-quencher pair and when a recognition event takes place, the ends are forced apart, increasing the distance between the dye molecule and quencher so that a fluorescence is observed. This concept might be extended to actuate a spatial charge variation. These sequences are developed by in-vitro evolution so that a large number of prospective chemistries can be rapidly evaluated.[2]

[1]N. Hamaguchi, A. Ellington, and M. Stanton. "Aptamer Beacons for the Direct Detection of Proteins." *Analytical Biochemistry* **294** 126 (2001).

[2]S. Jhaveri, M. Rajendran, and A. D. Ellington. "In vitro selection of signaling aptamers." *Nature Biotechnology* **18** 1293 (2000).

8.2.2 Development of Complementary Label-Free Systems

The development of label-free biosensing strategies continues on many fronts: potentiometry, surface-stress mechanical bending, resonant microbalance, surface plasmon resonance, etc. Binary tests—is the target present or not—are developed routinely. However, the real-time quantification of signaling pathways necessary for systems biological understanding requires more subtle measurements within complex backgrounds. It seems likely that the coordinated application of multiple sensing mechanisms within a single analytical system will enable a greater range of detection possibilities with higher specificity.

Studying the response of multiple label-free detection methods to the same assay may yield insight into data interpretation. For example, consider the mechanical deflection sensor developed at IBM,[3] and further pursued by Savran et al.[4] The bending mechanism is not completely understood. The bending response is too great to be caused simply by the additional mass of adsorbed molecules. Proposed mechanisms include steric interactions, charge interactions, and the leading candidate: changes in entropy of the molecular layer. Investigating the response of multiple types of label-free biosensors, may inform signal interpretation and enable measurements of greater quantitative significance.

8.2.3 Microscale Model System for Nanoscale Sensors

Finally, a topic that was only briefly investigated in this work is the scaling down of lateral dimensions of potentiometric sensing. At the microscale, scaling enables high sensor density within a compact area. However, the development of nanoscale potentiometric sensors could enable fundamentally new measurement capabilities. Nanoscale sensing could enable detection with sub-cellular spatial resolution, or even single-molecule measurements.

In the meantime, there may be topics which can be investigated at the microscale to yield insight into nanoscale devices. For example, it has been suggested that nanotube and nanowire sensors, such as those developed in the Lieber group,[5] might offer greatly improved surface potential resolution over tradition ISFETs because of their thin, natively formed gate oxide layers. The

[3] J. Fritz, M.K. Baller, H.P. Lang, H. Rothuizen, P. Vettiger, E. Meyer, H.-J. Güntherodt, C. Gerber, and J.K. Gimzewski. "Translating biomolecular recognition into nanomechanics." *Science* **288** 316 (2000).

[4] C.A. Savran, A.W. Sparks, J. Sihler, J. Li, W. Wu, D.E. Berlin, T.P. Burg, J. Fritz, M.A. Schmidt, and S.R. Manalis. "Fabrication and characterization of a micromechancical sensor for differential detection of nanoscale motions." *Journal of Microelectromechanical Systems* **11** 703 (2002).

[5] Y. Cui, Q. Wei, H. Park, and C. M. Lieber. "Nanowire nanosensors for highly sensitive and selective detection of biological and chemical species." *Science* **293** 1289 (2001).

sensors developed in this thesis offer a microscale field-effect analog, with similar gate insulators. A comparison of the resolution of microscale and nanoscale sensors with similar gate dielectrics could elucidate the effects of the thin gate oxide, the surrounded gate geometry, and quantum effects of the nanowire sensors.

The sensors presented in this thesis can be produced by batch fabrication techniques, while nanowire sensors are fabricated by serial, labor-intensive procedures. Nanoscale sensors offer high spatial resolution, but because of their fabrication procedure, it would be cumbersome to develop functionalization protocols for them, where many trials may be neccessary to optimize surface chemistry. Microscale field-effect sensors, on the other hand, can be batch fabricated, and have been shown to be robust through multiple experiment and cleaning cycles. Microscale field-effect sensors with thin gate oxide may provide a useful model system for developing assay chemistry that may ultimately intended for nanoscale sensors.

8.2.4 Systems Integration

The present work has been concerned with improving the resolution and viability of field-effect biosensing techniques. As such, investigation of prototype assays has been conducted on a small scale, with a few sensors in a differential configuration. As we look toward benchtop research and diagnostic applications, the development of multiplexed arrays of tens or hundreds of sensors will enable rapid, parallel measurements. Simpler readout circuitry with low per-sensor measurement time will be necessary for the development of arrays with multiplexed readout.

Integrating small-volume fluidic handling systems and an on-chip counter-electrode could minimize series resistance contributions which distort CV characteristics.

The noise of the detection system was found to be limited by the readout electronics rather than noise inherent in the sensor. This indicates an opportunity for improving surface potential resolution by by improving the readout electronics.

One of the most promising aspects of potentiometric sensing is its real-time measurements capabilities. The ability to measure time-courses of signaling chemistries, rather than endpoint values will greatly expand biosensing capabilities. At the time of writing, the dynamic measurement capabilities have not been fully exploited for measurement of rate kinetics. This is largely due to the flow profile through the fluidic chamber. The chamber is relatively large ($\sim 500\mu$L) compared to the sensors and injection does not result in complete displacement of the previous contents of the cell. The effects of mixing and diffusion within the fluid chamber contribute to hysteresis in

the measurement since previous analytes cannot be completely eliminated.

Translating the sensor to a planar surface with an integrated microfluidics handling system will provide a more repeatable environment for measurement of reaction kinetics. Scaling down the flow cross section of the fluidic delivery system will enable faster switching times, and complete volumetric displacement of each analyte by the subsequent analyte. Further, molecular handling strategies such as the recent demonstration by Huber et al.,[6] may increase the effective concentration resolution of the system.

[6]D. L. Huber, R. P. Manginell, M. A. Samara, B-I. Kim, and B. C. Bunker. "Programmed Adsorption and Release of Proteins in a Microfluidic Device." *Science* **301** 352 (2003).

Appendix A

Fabrication Process Flow

Starting Material:

n-type Silicon-on-Insulator

3-5 Ωcm device layer, 2 μm thick

1 μm buried oxide layer

500 μm handle

Step	Description	Machine	Lab	Parameters
1	RCA clean	RCA	ICL	
2	Oxidation	Tube 5A GateOx	ICL	Dry O2 ; 950 C ; 37 minutes
	Pattern Implant Mask			
3	HMDS	coater6	ICL	
4	Spin-Coat	coater6	ICL	OGC-825 1 μm
5	Pre-bake	coater6	ICL	
6	Expose	KS2	TRL	30 s
7	Develop	photo-wet-l	TRL	OGC-934 1:1
8	Post-Bake	post-bake	TRL	
9	Implant			Implant Sciences in Wakefield
				Phosphorus 7e15 at 90 keV
10	Etch exposed oxide	pre-metal	ICL	HF to dewet

11	Strip PR	asher	ICL	90 s
	Pattern Device Silicon			
12	HMDS	HMDS	TRL	
13	Spin-Coat Resist	coater	TRL	thick resist:AZ-4620 @ 4 krpm
14	Pre-Bake	pre-bake	TRL	60 min 90 C
15	Align and Expose	KS2	TRL	500 s
16	Develop	photo-wet-l	TRL	AZ-440 until clear
17	Post-Bake	pre-bake	TRL	30 min 90 C
18	Etch Silicon	AME5000	ICL	~4 minutes; HBr-Cl2
19	Strip PR	Pre-Metal	ICL	2 x 10 minutes piranha
20	Etch expose oxide	oxide	ICL	BOE 15-30 s. until dewet
21	RCA clean	RCA	ICL	
22	Field Oxide Diffusion	Tube 5D FieldOx	ICL	Wet O2; 1050 C; 200 min target thickness 1 μm
	Pattern Gate Cuts			
23	HMDS	HMDS	TRL	
24	Spin-Coat Resist	coater	TRL	thick resist:AZ-4620 @ 4 krpm
25	Pre-Bake	pre-bake	TRL	60 min 90 C
26	Align and Expose	KS2	TRL	500 s
27	Develop	photo-wet-l	TRL	AZ-440 until clear
28	Post-Bake	pre-bake	TRL	30 min 90 C
29	Etch oxide in BOE	oxide	BOE	~5 minutes BOE until de-wet
30	Strip PR in piranha	pre-metal	ICL	2 x piranha, 10 minutes each
31	RCA clean	RCA	ICL	
32	Gate Oxidation	Tube 5A GateOx	ICL	950 C; dry oxidation; 90 min target thickness 420 Å
	Pattern Contact Cuts			
33	HMDS	HMDS	TRL	
34	Spin-Coat Resist	coater	TRL	thick resist:AZ-4620 @ 4 krpm
35	Pre-Bake	pre-bake	TRL	60 min 90 C
36	Align and Expose	KS2	TRL	500 s

37	Develop	photo-wet-l	TRL	AZ-440 until clear
38	Post-Bake	pre-bake	TRL	30 min 90 C
39	Etch Contact Cuts	oxide	ICL	5 minutes BOE until de-wet
40	Pre-metal clean	pre-metal	ICL	2x piranha, 30 s HF
41	Aluminum Deposition	e-beam	ICL	5000 Å thickness with planetary
	Pattern Aluminum			
42	HMDS	HMDS	TRL	
43	Spin-Coat Resist	coater	TRL	thick resist:AZ-4620 @ 4 krpm
44	Pre-Bake	pre-bake	TRL	60 min 90 C
45	Align and Expose	KS2	TRL	500 s
46	Develop	photo-wet-l	TRL	AZ-440 until clear
47	Post-Bake	pre-bake	TRL	30 min 90 C
47	Etch Aluminum	acid-hood	TRL	Al wet etchant
48	Strip resist	solvent-noAU	TRL	acetone soak or oxygen plasma ash
49	Forming Gas Anneal	TubeA3	TRL	30 minutes Forming Gas
50	Coat Front Side	coater	TRL	OGC-835
51	Pre-bake	pre-bake	TRL	30 min @ 90 C
	Pattern Back Side			
52	HMDS	HMDS	TRL	
53	Spin-Coat Resist	coater	TRL	thick resist:AZ-4620 @ 1500 krpm
54	Pre-Bake	pre-bake	TRL	60 min 90 C
55	Align and Expose	KS2	TRL	500 s
56	Develop	photo-wet-l	TRL	AZ-440 until clear
57	Post-Bake	pre-bake	TRL	30 min 90 C
57	Mount on Quartz Wafer	coater	TRL	concentric rings of thick resist
58	bake	pre-bake	TRL	10 min.
59	Through-Wafer DRIE Etch	STS1	TRL	MIT_59 $\sim$ 4 hours
60	Dismount in hot microstrip	photo-wet-r	TRL	

Appendix B

Terabit-per-Square-Inch Data Storage with the Atomic Force Microscope

An areal density of 1.6 Terabits per square inch has been achieved by anodically oxidizing titanium with the atomic force microscope (AFM). This density was made possible by (1) single-wall carbon nanotubes (SWNT) selectively grown on an AFM cantilever, (2) atomically flat titanium surfaces on $\alpha - Al_2O_3$ (1012), and (3) atomic scale force and position control with the tapping-mode AFM. By combining these elements, 8 nm bits on a 20 nm pitch were written at a rate of 5 kbit/s at room temperature, in air.

The magnetic hard disk is the dominant method for storing data in the microelectronics industry. Its progress has been fueled by the ever-increasing demand for storage capacity coupled with the continual decrease in price per megabyte. In 1990, state of the art hard disks had an areal density of less than 0.1 Gbit/in^2; in 1999, disks with areal densities of 5 Gbits/in^2 were being sold. In the near future, it is expected that hard disk drive scaling, and the move to giant magnetoresistive heads, will push areal densities into the upper tens of Gbits/in^2. This growth rate can be described by a 60% cumulative annual increase—at this rate, conventional scaling is expected to run out in 2006. This technological limitation will not stop the need for greater storage capacity in less space.

To displace magnetics as the mainstream method for data storage, an emerging technology must offer substantial advantage beyond the incremental advance of an existing technology. Many approaches have been brought forward; the two most prominent are nanoimprint and scanning probe. Chou and co-workers[1,2,3] have pioneered nanoimprintation as a method for fabricating 400 Gbit/in^2 read-only (compact disk) devices

[1] P.R. Krauss, and S.Y. Chou. "Nano-compact disks with 400 Gbit/in^2 storage density fabricated using nanoimprint lithography and read with proximal probe" *Applied Physics Letters* **71** 3174 (1997).

[2] W. Wu, B. Cui, X.-Y. Sun, W. Zhang, L. Zhuang, L. Kong, and S.Y. Chou. "Large area high density quantized magnetic disks fabricated using nanoimprint lithography" *Journal of Vacuum Science and Tehcnology B* **16** 3825 (1998).

[3] B. Cui, W. Wu, L. Kong, X. Sun, and S.Y. Chou. "Perpendicular quantized magnetic disks with 45 Gbits on a 4×4 cm^2 area" *Journal of Applied Physics* **85** 5534 (1999).

and 45 Gbit/in2 read-write devices. Binnig et al.,[4] Mamin and Rugar,[5,6] and Chui[7] through a series of innovations, have pursued a read-write system based on scanning probes that has achieved an areal density of 400 Gbits/in2. Both of these techniques show clear paths to a complete data storage system.

We report here an alternative method for writing bits on a substrate. It is not the goal to show a complete system, but simply to locate what the authors believe to be the uppermost point for areal bit density obtained at room temperature and in air. There is a long history in the literature of surface modification with scanning probe microscopes,[8,9,10] however none of these exceed the threshold of a terabit-per-square-inch. Atomic and molecular scale modifications far surpass this threshold but are generally not suited for data storage because of their low-temperature or vacuum operation. Examples of this include Eigler and Stroscio using the cryogenic scanning tunneling microscope (STM) to move around single atoms,[11] and Gimzewski, Cuberes, and Schlittler using the vacuum STM to align C60 molecules on copper lattices.[12] Albrecht et al. have used the STM in air to ablate graphite to create sub-10-nm holes, however, this technique was often unstable as the ablation and imaging process can obscure adjacent patterns and damages tips.[13]

We have demonstrated that the tapping-mode atomic force microscope (AFM) can oxidize atomically flat titanium with a single-walled carbon nanotube to achieve a bit density of 1.6 Tbits/in2. at a rate of 5 kbits/s. While this data rate is exceedingly slow for storage application, parallelism, as demonstrated by the groups at IBM[14,15] and Stanford[16,17] can serve to overcome this limitation. Tapping mode is used to reduce

---

[4]G. Binnig, M. Despont, U. Drechsler, W. Haeberle, M. Lutwyche, P. Vettiger, H.J. Mamin, B.W. Chui, and T. W. Kenny."Ultrahigh-density atomic force microscopy data storage with erase capability" *Applied Phyics Letters* **74** 1329 (1999).

[5]H.J. Mamin and D. Rugar. "Thermomechanical writing with an atomic force microscope tip." *Applied Physics Letters* **61** 1003 (1992).

[6]H.J. Mamin. "Thermal writing using a heated atomic force microscop tip." *Applied Physics Letters* **69** 433 (1996).

[7]B.W. Chui, T.D. Stowe, T.W. Kenny, H.J. Mamin, B.D. Terris, and D. Rugar. "Low-stiffnes silicon cantilevers for thermal writing and piezoresistive readback with the atomic force microscope." *Applied PHyiscs Letters* **69** 2767 (1996)

[8]E. Betzig, J.K. Tautman, T. D. Harris, J.S. Weiner, and R.L. Kostelak."Breaking the diffraction barrier: optical microscopy on a nanometer scale." *Science* **251** 1486 (1991).

[9]R.C. Barrett and C.F. Quate. "Charge storage in a nitride-oxide-silicon medium by scanning capacitance microscopy." *Journal of Applied Phyiscs* **70** 2725 (1991).

[10]B.D. Terris, H.J. Mamin, and D. Rugar. "Data storage based on proximal probe techniques." *Applied Physics Letters* **68** 141 (1996).

[11]J.A. Stroscio adn D.M. Eigler. "Atomic and molecular manipulation with the scanning tunneling microscope." *Science* **254** 319 (1991).

[12]M.T. Cuberes, R.R. Schlittler, and J.K. Gimzewski. "Manipulation of C/60 molecules on Cu(111) surfaces using a scanning tunneling microscope." *Applied Physics A Materials Science Processing* **66** S669 (1998).

[13]T.R. Albrecht, M.M. Dovek, M.D. Kirk, C.A. Lang, and C.F. Quate. "Nanometer-scale hole formation on graphite using a scanning tunneling microscope." *Applied Physics Letters* **55** 1727 (1989).

[14]M.Lutwyche, C. Andreoli, G. Binnig, J. Brugger, U. Drechsler, W. Haberle, H. Rohrer, H. Rothuizen, P. Vettiger, G. Yaralioglu, and C.F. Quate. "5 × 5 2D AFM cantilever arrays: a first step towards a Terabit storage device." *Sensors and Actuators A* **73** 89 (1999).

[15]IBM, U.S. Patent No. 5,843,477 (November 10, 1998).

[16]S.C. Minne, G. Yaralioglu, S.R. Manlis, J.D. Adams, A. Atalar, J. Zesch, and C.F. Quate. "Automated parallel high-speed atomic force microscopy." *Applied Phyists Letters* **72** 2340 1998.

[17]K. Wilder, H.T. Soh, A Atalar, and C.F. Quate. "Nanometer-scale patterning and individual current-controlled lithography using multiple scanning probes." *Rev Sci Instrum* **70** 2822 (1999).

lateral forces and permit operation with the single-walled nanotube tip. The nanotube tip allows for highly localized surface modification. Additionally, the extreme hardness and cylindrical shape of the nanotube alleviate bit degradation from tip wear during the write process, and minimize tip convolution effects during the read process.

Bits were written in titanium using the electric field from the conductive nanotube to locally oxidize the titanium surface.

Our substrate consists of a 2-nm thick conformal layer of titanium on an atomically flat $\alpha - Al_2O_3$ (1012) surface.[18] The surface roughness is approximately 1 Å, which is critical for two reasons. First, it allows consistent, repeatable lithography. Extreme discontinuities in the surface cause sticking and deformation of patterned features. Second, since the average height of the titanium oxide bits is approximately 1 nm, high surface roughness can cause ambiguity in reading features.

For writing, a 5 kHz square wave of +0.5 and -9.5 V was applied to the tip. An average tip velocity of 100 m/s was used to produce 8 nm bits at a 20 nm pitch, which is equivalent to a bit density of 1.6 Tbits/in2. The images in Figure B were taken from the 16 μm^2 area that had been completely patterned with bits. Several such areas were written with a single nanotube tip, without degradation of resolution or uniformity. Bits as small as 6 nm in diameter were written at 12-15 nm spacing by adjusting the frequency of the control voltage, and the tip velocity. SWNTs allow significantly faster writing rates compared to conventional silicon cantilever tips, which typically write at rates equivalent to 5-30 bits/s when producing oxide of comparable height.[19,20]

We extend improvements to feature sizes achievable with AFM field-induced oxidation by combining single-walled nanotube tips with an atomically flat substrate. This allowed us to demonstrate controllable data storage at densities upwards of 1.6 Tbits/in^2. The success of this lithography is highly dependent on the length, stiffness, and diameter of the SWNT tip. The lithography approach described here is not limited to data storage applications, but can be extended to other sub-10-nm nanofabrication applications.

[18]K. Matsumoto, Y. Gotoh, J.-I. Shirakashi, T. Maeda, and J. Harris. "Fabrication of single electron memory on atomically flat alpha-Al2O3 substrate mdae by AFM nano-oxidation process." *Technical Digest of the International Electron Devices Meeting 1997* 155 (1997).

[19]P. Avouris, R. Martel, T. Hertel, and R. Sandstrom. "AFM-tip-induced and current-induced local oxidation of silicon and metals" *Applied Phyics A - Materials Science and Processing.* **66** S659 (1998).

[20]F. Perez-Murano, K. Birkelund, K. Morimoto, and J.A. Dagata. "Voltage modulation scanned probe oxidation." *Applied Physics Letters* **75** 199 (1999).

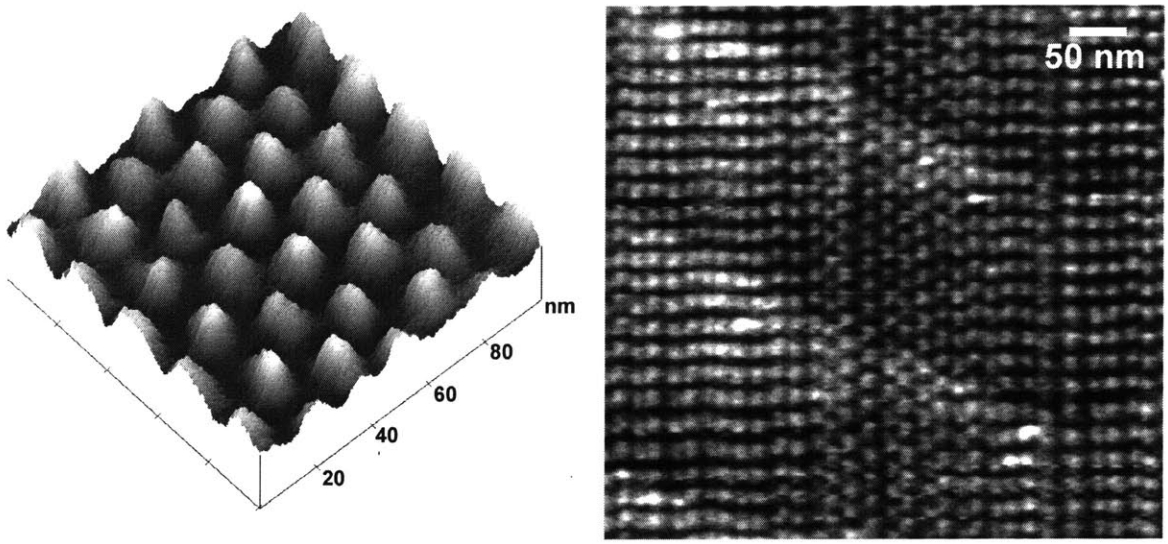

Figure B-1: Atomic force micrographs of anodically oxided titanium oxide bits. Left: 500 nm × 500 nm tapping-mode AFM image of high-density bit array taken from a 16 μm^2 patterned area. The vertical scale is 2 nm. The crystal planes of the substrate can clearly be seen. Right: 100 nm × 100 nm × 2 nm surface plot of 8 nm bits with a 1 nm titatium oxide height.

Appendix C

List of Publications

E.B. Cooper, S.R. Manalis, H. Fang, H. Dai, K. Matsumoto, S.C. Minne, T. Hunt, and C.F. Quate. "Terabit-per-square-inch data storage with the atomic force microscope." *Applied Physics Letters* **75** 3566 (1999).

S.R. Manalis, E.B. Cooper, P.F. Indermuhle, P. Kernen, P. Wagner, D.G. Hafeman, H. Dai, S.C. Minne, and C.F. Quate. "Microvolume field-effect pH sensor for the scanning probe microscope." *Applied Physics Letters* **76** 1072 (2000).

E.B. Cooper, E.R. Post, S. Griffith, J. Levitan, S.R. Manalis, M.A. Schmidt, and C.F. Quate. "A high-resolution micromachined interferometric accelerometer." *Applied Physics Letters* **76** 3316 (2000).

Y. Gotoh, K. Matsumoto, T. Maeda, E.B. Cooper, S.R. Manalis, S.C. Minne, T. Hunt, H. Dai, J. Harris, and C.F. Quate. "Experimental and theoretical results of room-temperature single-electron transistor formed by the atomic force microscope nano-oxidation process." *Journal of Vacuum Science and Technology A* **18** 1321 (2000).

E.B. Cooper, J. Fritz, F. Wiegand, P. Wagner, and S.R. Manalis. "Robust microfabricated field-effect sensor for monitoring molecular adsorption in liquids." *Applied Physics Letters* **79** 3875 (2001).

J. Fritz, E.B. Cooper, S. Gaudet, P.K. Sorger, and S.R. Manalis. "Electronic detection of DNA by its intrinsic molecular charge." *Proceedings of the Nation Academy of Sciences* **99** 14142 (2002).